DEPARTAMENTO DE FÍSICA APLICADA

DOCTORAL THESIS

POROUS SILICON BIOMATERIALS:
PSi/CYCLODEXTRIN DRUG DELIVERY HYBRIDS AND PSi/CALCIUM PHOSPHATE BIOCERAMIC CELL SCAFFOLDS

Thesis submitted by
Jesús Jacobo Hernández Montelongo
to obtain the degree of
Doctor in Physics

Madrid, Spain. November, 2013.

UNIVERSIDAD AUTÓNOMA DE MADRID

DEPARTAMENTO DE FÍSICA APLICADA

DOCTORAL THESIS

POROUS SILICON BIOMATERIALS:
PSi/CYCLODEXTRIN DRUG DELIVERY HYBRIDS AND PSi/CALCIUM PHOSPHATE BIOCERAMIC CELL SCAFFOLDS

Thesis submitted by
Jesús Jacobo Hernández Montelongo
to obtain the degree of
Doctor in Physics

Advisors:
Profr. Dr. Miguel Manso Silván
Profr. Dr. Vicente Torres Costa

Madrid, Spain. November, 2013.

A Luz Alejandra

“Le vrai point d’honneur [d’un scientifique] n’est pas d’être toujours dans le vrai. Il est d'oser, de proposer des idées neuves, et ensuite de les vérifier.”

- Pierre-Gilles de Gennes

“Science, like art, is not a copy of nature but a re-creation of her"

- Jacob Bronowski

Agradecimientos

"*Las fortalezas están en nuestras diferencias, no en nuestras similitudes*" -Stephen Covey

La realización de una tesis es en esencia un trabajo en equipo. Poco más de tres años han pasado desde que comenzó este proyecto, y durante el trayecto he recibido la ayuda y colaboración de muchas personas. Deseo ofrecerle a cada una de ellas mi más efusivo y sincero agradecimiento.

En primer lugar a mis directores de tesis, Miguel y Vicente, por sus conocimientos y amistad compartida. Desde los primeros correos electrónicos intercambiados, Miguel mostró su gran capacidad de liderazgo. Agradezco la confianza y libertad que me otorgó para sacar adelante cada una de las etapas de la tesis. Además de su guía y exigencia para mejorar siempre. Recuerdo cuando parafraseaba al maestro Miyagi de Karate Kid: "Dar cera, pulir cera, dar cera, pulir cera". Sin duda, parte de su tenacidad de deportista. Agradezco la supervisión fina de Vicente. Él, así como un artista que busca la armonía en su obra, evaluó el trabajo no sólo con la rigurosidad científica requerida, sino también con una visión estética.

A todos mis compañeros y amigos doctorantes del grupo de biomateriales. De ellos he aprendido no sólo los secretos artesanales, esos que no se publican, de la fabricación del silicio poroso y otros procesos fisicoquímicos, sino también de su cultura y gastronomía española: Álvaro, Darío, Elena, Esther, Gonzalo, Laura y Sonia. Quiero resaltar la colaboración y ayuda de Álvaro y Darío, con quienes desarrollé proyectos en conjunto. Saludos hasta Chile a mi compadre Nelson, que también hicimos excelente mancuerna científica. A mis otros compañeros doctorantes del departamento: Arancha, Daniel, Eduard, Guille, Luis, Noelia, Sergio, Teresa, Vali… muchas charlas compartimos en el comedor. Y por supuesto a Luis G. Pelayo, que no sólo me apoyó en todo lo técnico del laboratorio, sino también en el uso del sentido común, el menos común de los sentidos, para el entendimiento de conceptos rebuscados de la física.

Agradezco a los profesores Aurelio, Predes y Raúl por la oportunidad de trabajar con ellos, valiosos conocimientos me compartieron: espectroscopia RBS, biología celular y silicio poroso, respectivamente. Resalto también la ayuda de Luna en cuestiones administrativas. Ella es, indudablemente, un pilar del departamento.

La investigación científica en Europa se caracteriza por el trabajo multidisciplinario entre diferentes instituciones de diferentes países. Esta tesis no fue la excepción. Agradezco todo lo aprendido en ciclodextrinas al equipo galo: a Nicolas y Stéphanie por su compañerismo e instrucción científica. A Adeline, Alexandra, Cherry, Jatupol, Lena, Marijo y al resto del equipo Ch'ti. Por supuesto, también a Bernard, excelente profesor y persona. A la squadra azzurra y su ayuda en los estudios de superficie: Andrea, Gerardo, Giacomo, Paola y Valentina. A Germán y Juan por su orientación en las mediciones en SpLine del ESRF. Al equipo SIdI de la UAM: a Luis y Pascual con los análisis IR, a Mario y Noemí con los de XRD, y a Esperanza, Isi y Quique con la microscopía electrónica.

Al equipo administrativo Erasmus Mundus: Emeline, Maritza, Pilar, Sandra y Velia. Sin su orientación en los laberínticos trámites burocráticos, no hubiera logrado mi estancia tanto en Madrid como en Lille. Aprovecho la mención para agradecer al proyecto "Ventana de Cooperación Exterior Erasmus Mundus Lote 20" de la Comisión Europea que financió mi beca de doctorado. Un proyecto de tal envergadura no hubiera sido posible sin las instituciones involucradas: la Universidad de Guadalajara, la Universidad Autónoma de Madrid y la Université Lille 1.

A mis amigos becarios latinoamericanos y europeos: Alberto, Andrea, Belén, Carlos, Daphne, Diana, Gaby, Ivana, Lalo, Lars, Marco, Miriam, Pablo, Rafa, Ricci, Simone, Tania y Victor, por los viajes y cañas compartidas. A mis amigos bohemios en Madrid: Giovanni, María Eugenia, y aquí nuevamente Pablo. A mis amigos bohemios en México: Félix, Mónica, Paco y Paty. Y a mi amigo-colega IQ, que mucho tiene de culpa que ahora yo sea científico: Jorge.

A mi familia que estuvo siempre presente en mi corazón: Jacobo, Pavi, Rosaura, Ale –y Rafa–, y mi adorado sobrino Ramsés. A Mamá Chagua y mis demás raíces, la vena veracruzana y la arteria jalisciense…

Y sobre todo a mi musa luz de luna, Luz Alejandra, por todo su amor y apoyo.

Index

Acronyms List

Atomic Force Microscopy	AFM
β-cyclodextrin-citric acid polymer	polyCD
β-cyclodextrin	βCD
Brushite	BRU
Calcium current density	I_{Ca}
Calcium Phosphate	CaP
Calcium Pyrophosphate	PYR
Calcium reaction time	t_{Ca}
Calcium volume	V_{Ca}
Chemically oxidized macroporous silicon	mPSi-COx
Chemically oxidized nanoporous silicon	nPSi-COx
Ciprofloxacin	CFX
Cyclic Electrochemical Activation	CEA
Cyclic Spin Coating	CSC
Cyclodextrin	CD
Energy Dispersive X-ray Spectroscopy	EDX
Field Emission Scanning Electron Microscopy	FESEM
Fourier Transform Infrared Spectroscopy	FTIR

Fourier Transform Infrared Spectroscopy in Attenuated Total Reflectance mode	ATR-FTIR
Fourier Transform Infrared Spectroscopy in Specular Reflection mode	SR-FTIR
Full-width at half-maximum	FWHM
Glazing angle X-ray Diffraction	GA-XRD
Hydroxyapatite	HAP
Hard X-ray Photoelectron Spectroscopy	HAXPES
Human Embryonic Lung Cell Line	L132
Human Mesenchymal Stem Cells	hMSCs
Inhibition of the growth of 90% of microorganisms	MIC90
Macrostructured Porous silicon	mPSi
Monotite	MON
Nanostructured Porous silicon	nPSi
Phosphate Buffered Saline	PBS
Phosphate current density	I_P
Phosphate reaction time	t_P
Phosphate volume	V_P
Polymerized macroporous silicon	mPSi-CD
Polymerized nanoporous silicon	nPSi-CD
Porous silicon	PSi
Porous silicon/Calcium phosphate composite	PSi/CaP
Postoperative endophthalmitis	POE

Prednisolone	PDN
Root mean square roughness	R_{RMS}
Rutherford Backscattering Spectroscopy	RBS
Scanning Electron Microscopy	SEM
Thermogravimetric Analysis	TGA
Toluidine Blue Ortho	TBO
Transmission Electron Microscopy	TEM
Ultraviolet-visible Spectroscopy	UV-Vis
X-ray Diffraction	XRD
X-ray Photoelectron Spectroscopy	XPS

Chapter 1:

Introduction and Objectives

1.1 Introduction: Biomaterials

According to Williams [1], a biomaterial is “a substance that has been engineered to take a form which, alone or as part of a complex system, is used to direct, by control of interactions with components of living systems, the course of any therapeutic or diagnostic procedure, in human or veterinary medicine”. In that sense, biomaterials as a scientific domain is a recent area of knowledge —it is just over half century old—. It is a multidisciplinary field that encompasses aspects of medicine, biology, chemistry, physics and materials science. Besides, it also sits on a foundation of engineering principles [2].

Although the methodic study and design of biomaterials is recent, its use dates far back into ancient civilizations. Artificial eyes, ears, teeth, and noses have been found on Egyptian mummies [3]. Chinese and Indians used waxes, glues, and tissues in reconstructing missing or defective parts of the body [4]. The Mayan people fashioned nacre teeth from seashells in roughly 600 A.D. Similarly, an iron dental implant in a corpse dated 200 A.D. was found in Europe [2]. The Aztecs commonly used gold and silver plates to replace pieces of the skull following craniotomies [5]. So on, long lists of historic examples are mentioned in bibliographic references. Nevertheless, the modern era of biomaterials started in the late 1800s with two key innovations: the implementation of aseptic techniques reducing the potential of infection-related complications and the radiograph techniques for visualization of skeletal structures [6]. This allowed developing implants design, mainly metallics, more compatible with the human body.

Nowadays, biomaterials are not only used as implants or prostheses, which are typical functions, but they also have a wide range of medical and non-medical applications. Table 1 lists some of the most significant ones. This table illustrates the success reached by biomaterials and its importance to modern medical therapies. In economic terms, biomaterials are a potential market. They have evolved over the last 50

years or so to a US$100 billion endeavor [7]. At this moment, still many applications will require synthetics, so, it is possible to predict that the demand for biomaterials will grow through this century.

Table 1. Some uses for biomaterials (from Ratner and Bryant [7]).

Medical uses	**Non-medical uses**
Artery graft	Arrays for DNA and diagnostics
Artificial heart valve	Bioremediation materials
Implants (breast, cochlear, dental, etc.)	Biosensors
Tubes (feeding, guidance, drainage, etc.)	Bioseparations, chromatography
Drug and gene delivery devices	Biofouling-resistant materials
Hydrocephalous shunt	Biomimetics for new materials
Intraocular lens, keratoprosthesis	Cell culture/cell scaffolds
Joints (hip, knee, shoulder, etc.)	Controlled release for agriculture
Pacemaker	Electrophoresis material
Renal dialyzer	Microelectromechanical systems (MEMS)
Stent	Muscles (artificial) and actuators
Tissue adhesive	Nanofabrication
Urinary catheter	Neural computing/biocomputer

1.2 Porous silicon

Porous silicon (PSi) was discovered in 1956 by Uhlir [8] during some experiments of electropolishing, but was just reported as a technical note. Since then, PSi was ignored by scientific community until 1990 when its visible luminescence was discovered by Canham [9].

PSi is constituted by silicon nanocrystallites immersed in a porous silica skeleton [10]. This complex porous structure may reach a large internal surface area (~500 m^2/cm^3) [11]. In Fig 1, a FESEM image and a scheme of PSi are shown. The silicon nanocrystallite is covered by amorphous, silicon which is oxidized over time [12]. In TEM image of Fig. 2-a, individual silicon nanocrystallites are identified. They are round in the range between 20 Å and 80 Å without a preferential orientation (polycrystalline diffraction pattern) [13].

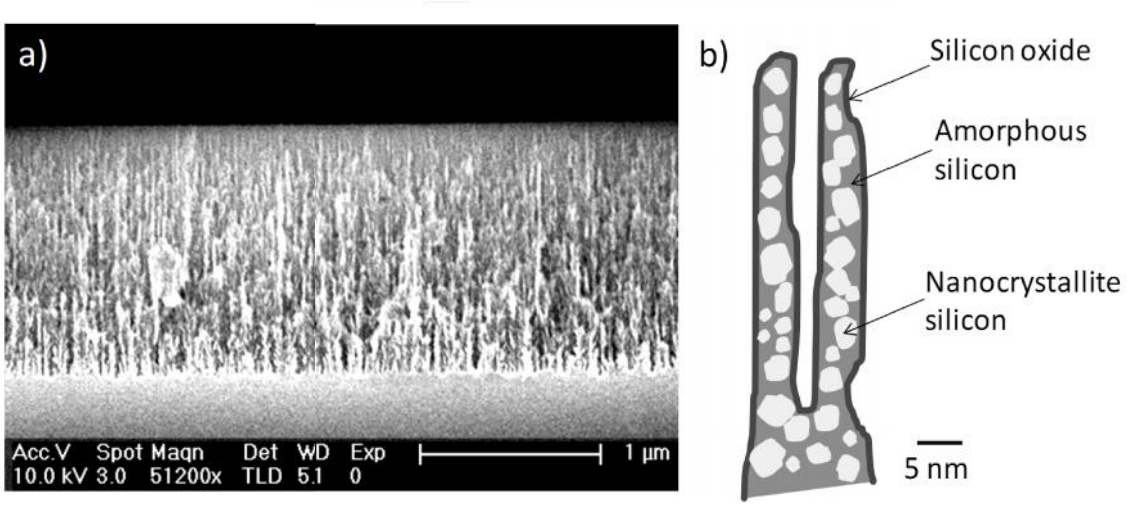

Figure 1. a) FESEM image of PSi layer (by J. Hernandez-Montelongo), and b) scheme in detail of typical PSi components (by J. R. Martín-Palma).

This particular nanostructure of PSi generates efficient photoluminescence and electroluminescence at room temperature in the visible (blue and red) and infrared [9,14]. The most accepted theory indicates that blue band is linked to the presence of surface silicon dioxide; the red band is due to quantum confinement of silicon nanocrystallite possibly supplemented by surface states; and the infrared band is correlated with dangling bonds and bandgap luminescence in large crystallites [10,15]. These properties made PSi a promising material for optoelectronic applications insomuch that publications dedicated to PSi grew exponentially in the 90's [16]. Among the most important PSi applications in optoelectronics are: light emitting devices (LED's) [17], solar cells [18], Bragg reflectors [19], optical waveguides [20] and photodetectors [21].

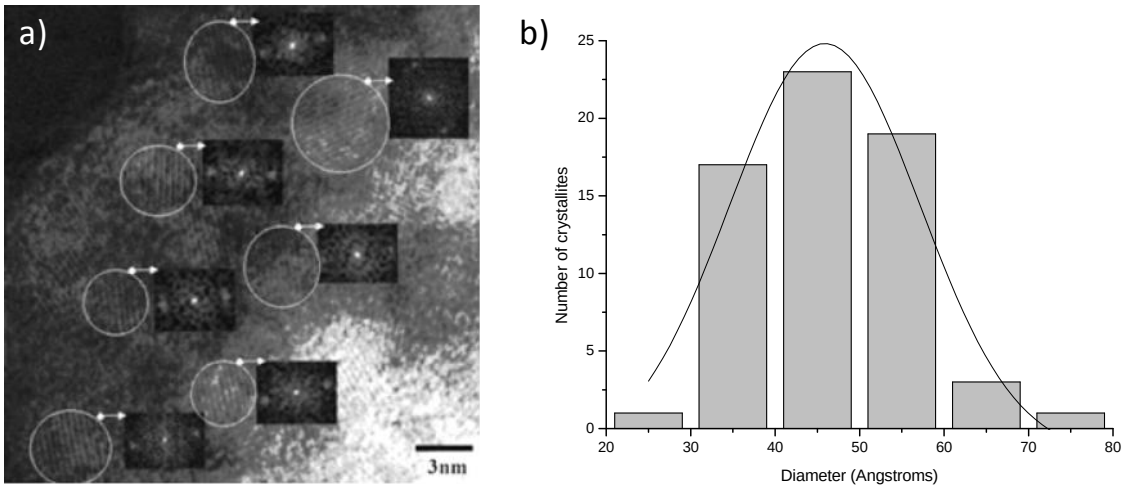

Figure 2. a) TEM image of PSi, and b) nanocrystallite size histogram (from Martín-Palma et al. [13]).

1.3 Porous silicon as a biomaterial

In 1995, Canham [22] demonstrated for first time the bioactivity of PSi by means of the hydroxycarbonate-apatite in-vitro growth on PSi surface over periods of days to weeks. Since then, other PSi bioapplications have been developed: biosensing [23], drug delivery [24], tissue engineering [25], tumor imaging [26], bioreactor platform [27], and others. These PSi scopes have been achieved because PSi is a porous semiconductor and its large surface area and surface chemistry provide a high reactivity. Hence, it is possible to generate a specific chemical composition or molecular adsorption on its surface [27]. Besides, PSi is also an excellent biomaterial given its biocompatibility, biodegradability and bioresorbability [28]. These PSi bioproperties are largely generated due to its particular susceptibility to oxidation. The silicon oxide is readily dissolved by body fluids [24] and later non-toxically eliminated as silicic acid in the urine [29]. Besides, PSi has been also combined with other materials, introduced into its pores or deposited on its surface, in order to obtain composites [30] which can extend or develop its applications and properties, including the bio [24,31].

In that sense, PSi research in medical and non-medical applications is still increasing because it is a suitable biomaterial for commercial industry. Silicon —the substrate to produce it—, is a low cost commodity compatible with high-tech electronic industry. Only in the semiconductor industry, the most relevant market for silicon, it has been predicted an increase from US$125 billion in 1998 to US$ 3.3 trillion in 2020 [32].

Among the most relevant uses of PSi as a biomaterial are drug delivery and cell scaffolds. The development of PSi-based devices oriented to these applications is increasingly relevant [33,34].The state of the art of them is outlined below.

1.3.1 PSi-based drug delivery devices

Drug delivery systems can be defined as materials designed to introduce therapeutic agents into the body with at least one of the following purposes [35]:

a) Sustain drug action at predetermined rates.
b) Localize drug action by placing a rate controlled system near or at the desired tissue or organ.
c) Target drug action by using carriers or chemical derivatization to deliver drug to a particular site.

Within this context, PSi is an attractive biomaterial for drug delivery applications. The size of the pores and the surface chemistry of the pore walls can be easily changed and controlled. Depending on the size and the surface chemistry of PSi pores, increased or sustained release of the loaded drug can be obtained [36]. Nevertheless, surface modified PSi is more frequently utilized than native PSi for drug delivery due to its enhanced stability.

Fig. 3 illustrates schematically the use of PSi as drug delivery device: as a single material and after surface modification; and Table 3 highlights several PSi modification methods that have been investigated for different drug release applications. Furthermore, but to a lesser extent, PSi composites —PSi combined with biopolymers—, have been shown to yield improved control over drug release kinetics and improved stability in aqueous media. Biopolymers that have been incorporated into PSi for drug delivery applications include [24]: polylactide, polydimethylsiloxane, polyethylene, polystyrene, polycaprolactone and poly(N-isopropylacrylamide).

On the other hand, the drug delivery devices based on PSi have been tested in different organs, such as intestinal epithelial cells [37]; adenocarcinoma cancer cells [38]; kidney, liver, and spleen [39]; tissues of the eye [34,40]; and others.

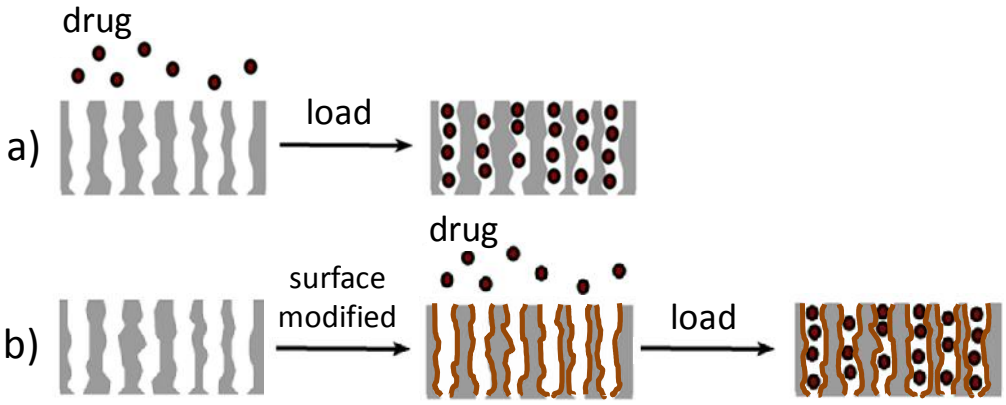

Figure 3. PSi-based drug delivery device: a) as a single material, b) surface modified (from Anglin et al.[24]).

Table 2. Some of the most relevant drug delivery systems using modified PSi (from Jarvis et al. [33]).

PSi surface modification	**Result: Tested with**
Thermal carbonization	Controlled release for highly soluble drugs: ibuprofen Reduced drug crystallinity: ibuprofen, antypirine, anitidine Reduction in pH dependent solubility: furosemide
Thermal hydrocarbonization	Sustained release: melatonan II, ghrelin antagon, peptide YY3-36 Increased dissolution from smaller pores: ibuprofen
Oxidation at 300 ºC	Improved dissolution of poorly soluble drugs: griseofulvin, urosemide, antypirine, ranitidine Increased Caco-2 cell layer permeation: griseofulvin Sustained release: peptide YY3-36
Oxidation at 800 ºC	Controlled release, pH triggered release: vancomycin Improved protein activity: lysozyme
pNIPAM grafting	Temperature controlled release: camptothecin
Electrochemical methylation	Controlled release, pH triggered release: vancomycin

1.3.2 PSi-based cell scaffolds

According to Williams [41], tissue engineering "is the persuasion of the body to heal itself through the delivery to appropriate sites of molecular signals, cells and supporting structures". In that sense, a cell scaffold for a tissue engineering application is a substrate designed to support the appropriate cellular activity, including the facilitation of molecular and mechanical signaling systems, in order to optimize tissue regeneration, without eliciting any undesirable local or systemic responses in the eventual host [42].

Due to its biomedical properties, PSi has been incorporated in tissue engineering as cell scaffold. Its micro/nano-morphology can regulate cell behavior [43]. Its flexible surface chemistry can be tailored to improve the PSi-cell interaction interfacial properties [44]. It is a bioactive material in simulated plasma, whereby corrosion of the film with release of $Si(OH)_4$ stimulates calcification and posterior hydroxyapatite formation [25]. Besides, PSi has an advantage over other biomaterials, its ability to be easily degraded in aqueous solutions into non-toxic silicic acid [45]. An example of the PSi use as cell scaffold is shown in Fig. 4.

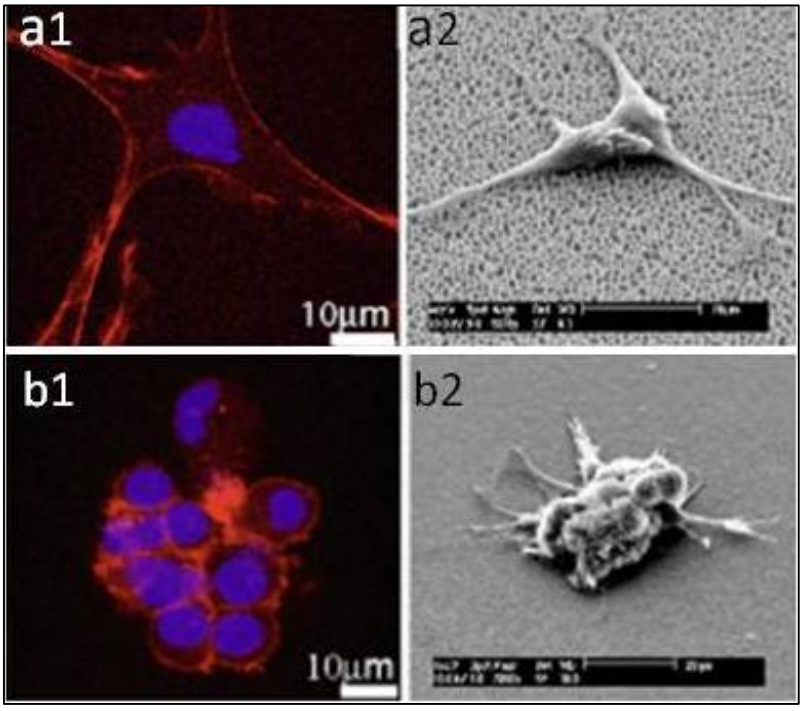

Figure 4. Neurobastoma cells after 24h growth: a1) confocal image of macrostructured PSi, a2) SEM image of macrostructured PSi, b1) confocal image of nanostructured PSi and b2) SEM image of nanostructured PSi (from Khung et al. [46]).

The confocal microscope and SEM images in Fig. 4 are representative of neurobastoma cells cultured on two different PSi surfaces: macrostructured (pores: 1000-3000 nm) and nanostructured (pores: 50-100 nm) [46]. Different growth and cell morphology in function of PSi pore size is perceived. Therefore, specific stimulations in cells can be controlled as needed.

As in other PSi applications, the use of PSi as a cell scaffold can take place in the form of a single material, after appropriate surface modification, or as a composite biomaterial. Table 4 lists the most highlighted cases of cell cultures on PSi-based cell scaffolds.

Table 4. Cell cultures on different kinds of PSi scaffolds.

PSi scaffold	**Cell culture**	**Reference**
Nanostructured	B50 neuron and Chinese hamster ovary	Bayliss et al. [47,48]
Oxidized by ozone	Hepatocyte	Chin et al. [49]
Thermally oxidized, carbon layer coated, methillized.	Human retinal endothelial, mouse aortic endothelial, murine melanomas, neuronal mouse, hamster ovarian	Angelescu et al. [50]
Composited with polycaprolactone and calcificated by SBF	Fibroplast	Coffer et al. [25] Whitehead et al. [51]
Different PSi patterns	Rat hippocampal neuron	Sapelkin et al [52]
Modified by ozone oxidation, silanizated and coated with collagen and serum	Rat pheochromocytoma (PC12) and human lens epithelial	Low et al. [45]
Nano and macrostructured	Osteoblast	Sun et al. [43]
Macrostructured and oxidized by H_2O_2	Osteoblast	Sun et al. [44]
Structured with pore size continuous gradient	Neuroblastoma	Khung et al. [46]
Thermally oxidized and aminosilanized	Human ocular	Low et al. [34]
1D nanostructured PSi micropatterns	Human mesenchymal stem cells	Punzón-Quijorna et al. [53], Muñoz et al. [54]
2D nanostructured PSi micropatterns	Human mesenchymal stem cells	Torres-Costa et al. [55]

1.4 Objectives

As already introduced, the use of PSi as a biomaterial is currently increasing; not only because of its interesting biomedical properties (biocompatibility, biodegradability and bioresorbability [28]), but also because PSi is potentially marketable due to its compatibility with high-tech electronic industry. Nevertheless, it is necessary to adapt its properties depending on the specific envisaged application. In that sense, this thesis aims at exploring new PSi modifications to obtain new advanced PSi-based structures for biomaterials applications. The new PSi-based biomaterials proposed in this thesis were designed to work in the field of drug delivery and cell scaffolds, some of the most important PSi uses as a biomaterial. The motivations and particular objectives of this thesis are:

1) To contribute to the PSi utilization in drug delivery applications. PSi-biopolymer composites are attractive candidates for drug delivery devices because they can display new chemical and physical characteristics, which are not exhibited by the individual constituents. In that sense, a section is dedicated to propose a new composite based on PSi and β-cyclodextrin polymer. The cyclodextrins are cyclic oligosaccharides that are widely used in pharmaceutical applications. Due to their characteristic cavity and their ability to form reversible complexes with drugs they have been used as efficient delivery carriers. Hence, the objective of this section was the development of new PSi/ cyclodextrin composites, their synthesis, characterization and test as potential drug delivery systems. For this reason, the first part of the title of this volume: “PSi/Cyclodextrin Drug Delivery Hybrids”. In order to explore a whole set of experimental conditions, the study involved the use of two kinds of PSi substrates, nanostructured and macrostructured, two drugs, ciprofloxacin (an antibiotic) and prednisolone (an anti-inflammatory), released in two media, pure water and phosphate buffered saline.

2) To provide new formulations of PSi for applications as cell scaffolds. In order to use PSi as cell scaffold in bone tissue engineering, deposition of calcium phosphate ceramics in its hydroxyapatite phase is required. This is because hydroxyapatite is an osteoconductive ceramic and constitutes the main inorganic part of natural bone. Different techniques to produce calcium phosphate coatings on PSi have been used, but not all of them are targeted to hydroxyapatite phase or are compatible to integrate

biological systems. Within this context, this section concerns a new hydroxyapatite deposition technique on PSi. Based on cyclic steps, the technique is developed from a sol-gel method to its optimization by an electrochemical method. Hence, the objective of this section was the development of new PSi-composite cell scaffolds. This contribution is thus outlined in second part of the title of this thesis: "PSi/Calcium Phosphate Bioceramic Cell Scaffolds". The study is based on a cyclic calcium phosphate deposition technique, optimizing the hydroxyapatite phase synthesis from spin coating to electrochemical activation with the purpose of finding an optimized process. The composites were also characterized and biologically tested.

1.5 Thesis organization

This thesis is organized as follows:

In Chapter 2, the fundamentals of the experimental techniques used in this work are explained. It starts with the know how behind the electrochemical etching of PSi, both nanostructured and macrostructured. Afterwards, as the thesis deals with the development of new PSi-based substrates for two different applications, the principles concerning the methods used to modify PSi in each case are discussed. On the other hand, the bases of characterization techniques are briefly explained. Four kinds of microscopy methods and thirteen different physicochemical characterization techniques have been used. It should be noted that not all of them were used in each PSi configuration. Finally, the general concepts of drug release profiles and the *in vitro* biological assays are explained.

Next, two chapters correspond to each application envisaged: Chapter 3 is focused on the functionalization of PSi by β-cyclodextrin-citric acid *in situ* polymerization for drug delivery applications and Chapter 4 deals with the calcium phosphate deposition on PSi for cell scaffold applications. Each one of these chapters is structured as a paper: a brief introduction, method and materials, results and discussions, conclusions and references.

Finally, Chapter 5 summarizes the conclusions and discusses the perspectives for these new PSi-based biomaterials.

References

[1] Williams DF. On the nature of biomaterials. Biomaterials 2009;30(30):5897-5909.

[2] Ratner BD, Hoffman AS, Schoen FJ, Lemons J. Biomaterials science: a multidisciplinary endeavor. In: Ratner BD, Hoffman AS, Schoen FJ, Lemons J, editors. Biomaterials Science: An Introduction to Materials in Medicine: Elsevier; 2004. p. 1-9.

[3] Williams D, Cunningham J. Materials in Clinical Dentistry. Oxford, England: Oxford University Press; 1979.

[4] Ramakrishna S, Mayer J, Wintermantel E, Leong KW. Biomedical applications of polymer-composite materials: a review. Composites Sci Technol 2001;61(9):1189-1224.

[5] Grimm MJ. Orthopedic biomaterials. In: Kutz M, editor. Standard Handbook of Biomedical Engineering and Design: Mc Graw-Hill; 2004. p. 15.1-15.22.

[6] Binyamin G, Shafi BM, Mery CM. Biomaterials: a primer for surgeons. Semin Pediatr Surg 2006;15(4):276-283.

[7] Ratner BD, Bryant SJ. Biomaterials: where we have been and where we are going. Annu Rev Biomed Eng 2004;6:41-75.

[8] Uhlir A. Electrolytic shaping of germanium and silicon. Bell System Tech J 1956;35:333-347.

[9] Canham L. Silicon quantum wire array fabrication by electrochemical and chemical dissolution of wafers. Appl Phys Lett 1990;57(10):1046-1048.

[10] Bisi O, Ossicini S, Pavesi L. Porous silicon: a quantum sponge structure for silicon based optoelectronics. Surf Sci Rep 2000;38(1-3):1-126.

[11] Granitzer P, Rumpf K. Porous silicon—A versatile host material. Materials 2010;3(2):943-998.

[12] Petrova E, Bogoslovskaya K, Balagurov L, Kochoradze G. Room temperature oxidation of porous silicon in air. Mat Sci Eng B 2000;69:152-156.

[13] Martín-Palma R, Pascual L, Herrero P, Martínez-Duart J. Direct determination of grain sizes, lattice parameters, and mismatch of porous silicon. Appl Phys Lett 2002;81(1):25-27.

[14] Halimaoui A, Oules C, Bomchil G, Bsiesy A, Gaspard F, Herino R, et al. Electroluminescence in the visible range during anodic oxidation of porous silicon films. Appl Phys Lett 1991;59(3):304-306.

[15] Fauchet PM. Photoluminescence and electroluminescence from porous silicon. J Lumin 1996;70(1):294-309.

[16] Parkhutik V. Analysis of publications on porous silicon: from photoluminescence to biology. J Porous Mat 2000;7(1):363-366.

[17] Canham L, Cox T, Loni A, Simons A. Progress towards silicon optoelectronics using porous silicon technology. Appl Surf Sci 1996;102:436-441.

[18] Menna P, Di Francia G, La Ferrara V. Porous silicon in solar cells: a review and a description of its application as an AR coating. Solar Energy Mater Solar Cells 1995;37(1):13-24.

[19] Pavesi L, Dubos P. Random porous silicon multilayers: application to distributed Bragg reflectors and interferential Fabry-Perot filters. Semicond Sci Technol 1997;12(5):570-570–575.

[20] Loni A, Canham L, Berger M, Arens-Fischer R, Munder H, Luth H, et al. Porous silicon multilayer optical waveguides. Thin Solid Films 1996;276(1):143-146.

[21] Lee M, Wang Y, Chu C. High-sensitivity porous silicon photodetectors fabricated through rapid thermal oxidation and rapid thermal annealing. IEEE J Quantum Electron 1997;33(12):2199-2202.

[22] Canham LT. Bioactive silicon structure fabrication through nanoetching techniques. Adv Mater 1995;7(12):1033-1037.

[23] Dhanekar S, Jain S. Porous silicon biosensor: Current status. Biosensors and Bioelectronics 2013;41:54-64.

[24] Anglin EJ, Cheng L, Freeman WR, Sailor MJ. Porous silicon in drug delivery devices and materials. Adv Drug Deliv Rev 2008;60(11):1266-1277.

[25] Coffer JL, Whitehead MA, Nagesha DK, Mukherjee P, Akkaraju G, Totolici M, et al. Porous silicon-based scaffolds for tissue engineering and other biomedical applications. Phys Stat Sol (a) 2005;202(8):1451-1455.

[26] Martin-Palma RJ, Manso-Silvan M, Torres-Costa V. Biomedical applications of nanostructured porous silicon: a review. J Nanophotonics 2010;4(042502):1-20.

[27] Stewart MP, Buriak J. Chemical and biological applications of porous silicon technology. Adv Mater 2000;12(12):859-869.

[28] Hernández-Montelongo J, Muñoz-Noval A, Torres-Costa V, Martín-Palma R, Manso-Silvan M. Cyclic Calcium Phosphate Electrodeposition on Porous Silicon. Int J Electrochem Sci 2012;7:1840-1851.

[29] Reffitt DM, Jugdaohsingh R, Thompson RP, Powell JJ. Silicic acid: its gastrointestinal uptake and urinary excretion in man and effects on aluminium excretion. J Inorg Biochem 1999;76(2):141-147.

[30] Hérino R. Nanocomposite materials from porous silicon. Mat Sci Eng B 2000;69:70-76.

[31] Fernandez RE, Stolyarova S, Chadha A, Bhattacharya E, Nemirovsky Y. MEMS composite porous silicon/polysilicon cantilever sensor for enhanced triglycerides biosensing. IEEE Sensors J 2009;9(12):1660-1666.

[32] Williams E. Forecasting material and economic flows in the global production chain for silicon. Technol Forecast Soc 2003;70(4):341-357.

[33] Jarvis KL, Barnes TJ, Prestidge CA. Surface chemistry of porous silicon and implications for drug encapsulation and delivery applications. Adv Colloid Interface Sci 2012;175:25-38.

[34] Low SP, Voelcker NH, Canham LT, Williams KA. The biocompatibility of porous silicon in tissues of the eye. Biomaterials 2009;30(15):2873-2880.

[35] Paolino D, Sinha P, Fresta M, Ferrari M. Drug delivery systems. In: Webster J, editor. Encyclopedia of Medical Devices and Instrumentation: Wiley Online Library; 2006.

[36] Salonen J, Kaukonen AM, Hirvonen J, Lehto V. Mesoporous silicon in drug delivery applications. J Pharm Sci 2008;97(2):632-653.

[37] Foraker AB, Walczak RJ, Cohen MH, Boiarski TA, Grove CF, Swaan PW. Microfabricated porous silicon particles enhance paracellular delivery of insulin across intestinal Caco-2 cell monolayers. Pharm Res 2003;20(1):110-116.

[38] Vaccari L, Canton D, Zaffaroni N, Villa R, Tormen M, di Fabrizio E. Porous silicon as drug carrier for controlled delivery of doxorubicin anticancer agent. Microelectron Eng 2006;83(4):1598-1601.

[39] Park J, Gu L, von Maltzahn G, Ruoslahti E, Bhatia SN, Sailor MJ. Biodegradable luminescent porous silicon nanoparticles for in vivo applications. Nature Mater 2009;8(4):331-336.

[40] Cheng L, Anglin E, Cunin F, Kim D, Sailor MJ, Falkenstein I, et al. Intravitreal properties of porous silicon photonic crystals: a potential self-reporting intraocular drug-delivery vehicle. Br J Ophthalmol 2008;92(5):705-711.

[41] Williams DF. The Williams dictionary of biomaterials. : Liverpool University Press; 1999.

[42] Williams DF. On the mechanisms of biocompatibility. Biomaterials 2008;29(20):2941-2953.

[43] Sun W, Puzas JE, Sheu T, Liu X, Fauchet PM. Nano-to Microscale Porous Silicon as a Cell Interface for Bone-Tissue Engineering. Adv Mater 2007;19(7):921-924.

[44] Sun W, Puzas JE, Sheu T, Fauchet PM. Porous silicon as a cell interface for bone tissue engineering. Phys Stat Sol (a) 2007;204(5):1429-1433.

[45] Low SP, Williams KA, Canham LT, Voelcker NH. Evaluation of mammalian cell adhesion on surface-modified porous silicon. Biomaterials 2006;27(26):4538-4546.

[46] Khung Y, Barritt G, Voelcker N. Using continuous porous silicon gradients to study the influence of surface topography on the behaviour of neuroblastoma cells. Exp Cell Res 2008;314(4):789-800.

[47] Bayliss SC, Heald R, Fletcher DI, Buckberry LD. The culture of mammalian cells on nanostructured silicon. Adv Mater 1999;11(4):318-321.

[48] Bayliss S, Buckberry L, Harris P, Tobin M. Nature of the silicon-animal cell interface. J Porous Mat 2000;7(1):191-195.

[49] Chin V, Collins BE, Sailor MJ, Bhatia SN. Compatibility of primary hepatocytes with oxidized nanoporous silicon. Adv Mater 2001;13(24):1877.

[50] Angelescu A, Kleps I, Mihaela M, Simion M, Neghina T, Petrescu S, et al. Porous silicon matrix for applications in biology. Rev Adv Mater Sci 2003;5:440-449.

[51] Whitehead MA, Fan D, Mukherjee P, Akkaraju GR, Canham LT, Coffer JL. High-porosity poly (ε-caprolactone)/mesoporous silicon scaffolds: calcium phosphate deposition and biological response to bone precursor cells. Tissue Eng Pt A 2008;14(1):195-206.

[52] Sapelkin AV, Bayliss SC, Unal B, Charalambou A. Interaction of B50 rat hippocampal cells with stain-etched porous silicon. Biomaterials 2006;27(6):842-846.

[53] Punzón-Quijorna E, Sánchez-Vaquero V, Muñoz-Noval Á, Pérez-Roldán MJ, Martín-Palma RJ, Rossi F, et al. Nanostructured porous silicon micropatterns as a tool for substrate-conditioned cell research. Nanoscale Res Lett 2012;7(1):1-7.

[54] Muñoz A, Sánchez V, Punzón E, Torres V, Gallach D, González L, et al. Aging of porous silicon in physiological conditions: cell adhesion modes on scaled 1D micropatterns. J Biomed Mater Res A 2012;100(6):1615-1622.

[55] Torres-Costa V, Martínez-Muñoz G, Sánchez-Vaquero V, Muñoz-Noval Á, González-Méndez L, Punzón-Quijorna E, et al. Engineering of silicon surfaces at the micro-and nanoscales for cell adhesion and migration control. Int J Nanomed 2012;7:623-630.

Chapter 2:

Fundamentals of Experimental Techniques

2.1 Introduction

This chapter is divided in two main sections; the first one is related to PSi formation and the fundamentals used to synthesize the composite materials aimed in this study. Besides, the experimental conditions (raw materials, stabilization parameters and protocols) for each synthesis technique are described in detail.

In the second part, the basic principles of the characterization techniques are briefly explained, as well as the details of the parameters used for every analysis. A remarkable aspect of this thesis is the wide fan of characterization protocols and methods used. However, not all of them were used to characterize the two different types of PSi composites considered in this thesis.

2.2 Synthesis techniques

The composite biomaterials were fabricated using porous silicon (PSi) as a support matrix. Two kinds of PSi were used: nanostructured (nPSi) and macrostructured (mPSi). nPSi was used as a substrate in both kind of composites: PSi/cyclodextrin hybrids and PSi/calcium phosphate bioceramics; but mPSi was only used in the PSi hybrids. Besides, the experimental procedure for the processing of each type of PSi is detailed. The basic concepts of the techniques utilized to fabricate the PSi-based composites are also briefly discussed: β-cyclodextrin-citric acid *in situ* polymerization and cyclic calcium phosphate deposition (by means of spin coating and electrochemical activation). The conditions used in each case are also detailed.

2.2.1 Electrochemical etching: Porous silicon formation

PSi is formed by an electrochemical etching of Si in a HF-based electrolyte [1]. In this technique, the Si wafer acts as the anode and Pt electrodes are used as cathode and counter electrodes. The system is connected to a power supply, which regulates the current/voltage on the Si crystal [2]. Due to the fact that HF is extremely corrosive; Teflon beakers are commonly used as reactors. The electrochemical process is mainly controlled by the current/voltage and solution composition. A scheme of the electrochemical cell utilized in this thesis is shown in Fig. 1.

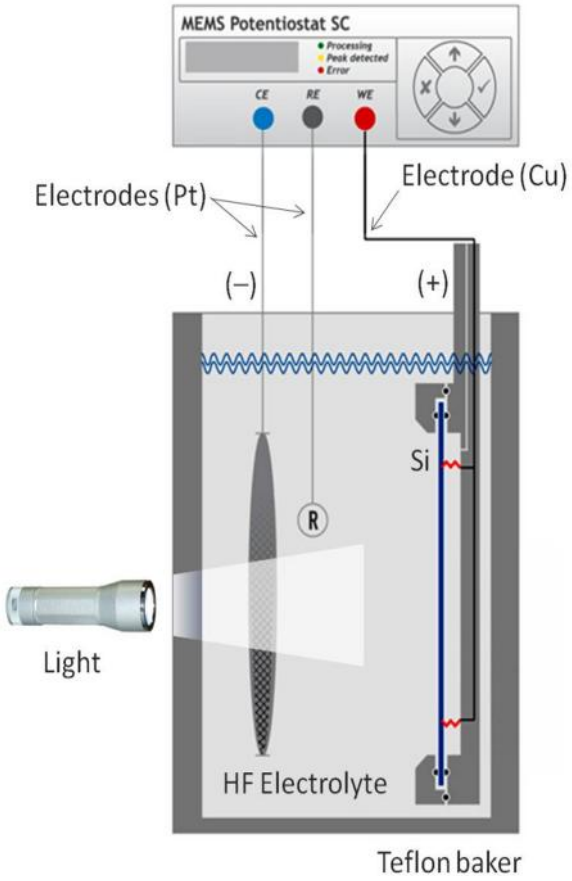

Figure 1. Scheme of the electrochemical cell used for PSi formation (adapted from Advanced Micromachining Tools [3]).

Different models have been proposed to explain pore formation in PSi. However, the most accepted model concerning the Si dissolution/PSi formation is the series of

electrochemical reactions schematized in Fig. 2 [4]. Initially, the Si atoms on the surface are passivated by Si-H bonds (1). Holes are injected from the bulk to the Si surface by the power supply. Thus, a nucleophillic attack on a Si-H bond by F^- anion can occur and a Si-F bond is formed (2). The Si-F bond causes a polarization effect allowing a second F^- anion to attack and replace the remaining hydrogen bonds. Two hydrogen atoms can then combine, injecting an electron into the substrate (3). The polarization induced by the Si-F bonds reduces the electron density of the remaining Si-Si backbonds making them susceptible to further attack by HF in such a manner that the remaining silicon surface atoms are bonded to the hydrogen atoms, which will be nucleophillically attacked again by a F^- anion forming silicon tretrafluoride (SiF_4) (4). The SiF_4 molecule reacts with HF to form the highly stable SiF_6^{2-} fluoroanion. The surface returns to its 'neutral' state until another hole is available (5).

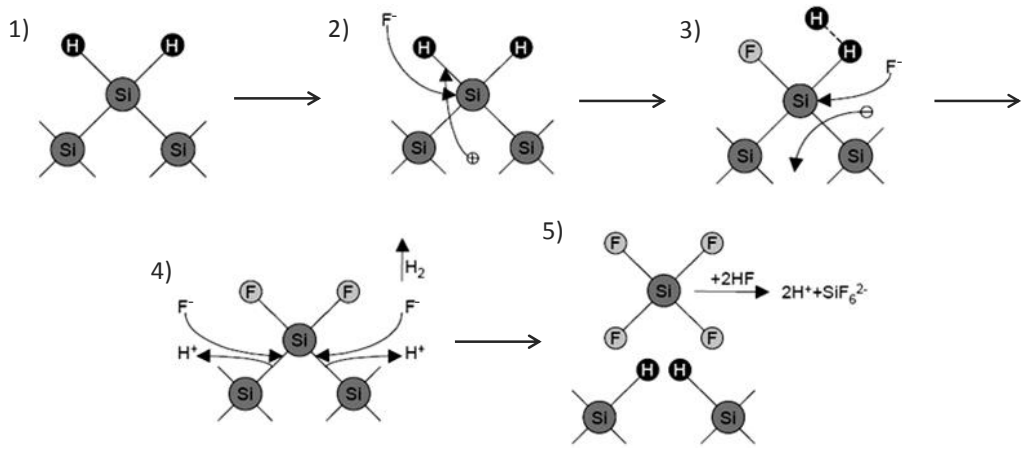

Figure 2. Model of Si dissolution (from Arrand [5]).

The Si dissolution depends on the injected holes (h^+) in the system. When they reach the surface, the previously described reaction mechanism is initiated. As the Si/HF interface shows a Schottky junction behavior (Fig. 3), these holes reach the interface by crossing the space charge region by thermionic effect [6]. After first pores are formed, holes begin to accumulate at the bottom reducing the potential barrier, thus enhancing Si dissolution in that zone. On the other side, the remaining Si structure (PSi formed) is more resistive because of charge carrier depletion; wherewith in depth pore growth is favored [7]. By this effect, PSi homogeneous layer and varying porosity multilayer formation are possible. Nevertheless, if anodic current is high enough, injected charge can

be higher than F^- infiltration into the pore, which produces the dissolution of the PSi columns (Fig. 4). The limit of the anodic current to produce PSi dissolution is known as the electropolishing threshold or critical current [8].

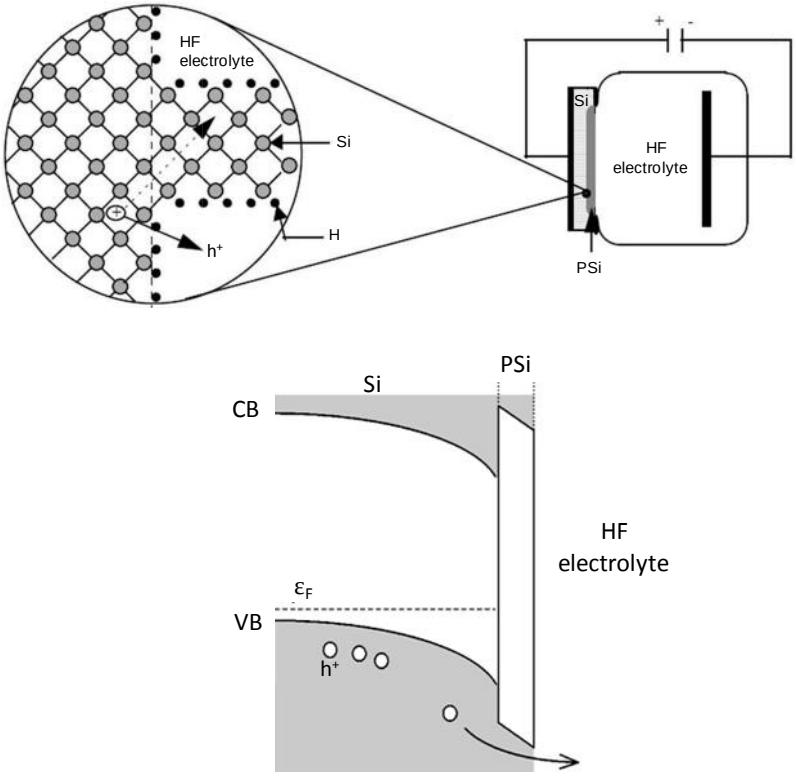

Figure 3. Scheme of Si/PSi/HF interface during electrochemical etching. CB = Conduction band, VB = Valence band, ε_F = Fermi energy (from Arrand [5] and Torres-Costa [9]).

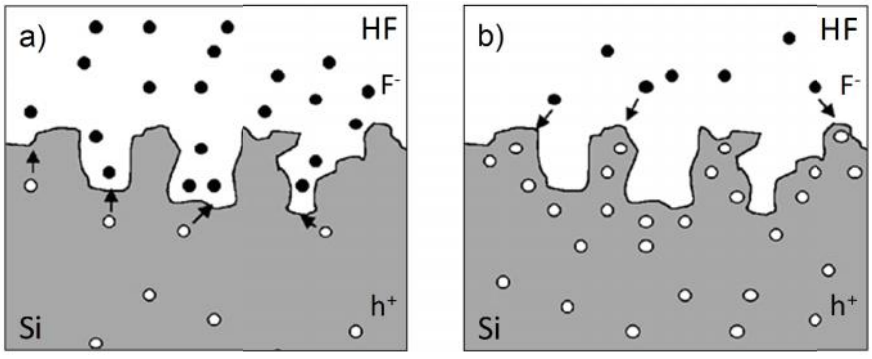

Figure 4. a) Si dissolution at the bottom of pores, where charge carriers preferentially emerge to the electrolyte, and b) Si electropolishing; anodic current is high enough so that holes reach the top of the PSi columns, which induce its dissolution (from Torres-Costa [9]).

All the properties of PSi, such as porosity, thickness, pore diameter and microstructure, depend on Si wafer properties and anodization conditions [1]. These conditions include HF concentration, current density, wafer type and resistivity, anodization duration, illumination (in n-type Si mainly), temperature and drying conditions. In Table 1 the main effects of anodization parameters on PSi formation are summarized.

Table 1. Main effects of anodization parameters on PSi formation (from Bisi et al. [1]).

An increase of … yields a	**Porosity**	**Etching rate**	**Critical current**
HF concentration	Decreasing	Decreasing	Decreasing
Current density	Increasing	Increasing	-
Anodization time	Increasing	Almost constant	-
Temperature	-	-	Increasing
Wafer doping (p-type)	Decreasing	Increasing	Increasing
Wafer doping (n-type)	Increasing	Increasing	-

i) Nanoporous silicon

PSi can be classified as a function of its pore size. According to IUPAC guidelines, the different types of PSi have been categorized as microporous (≤2 nm), mesoporous (2–50 nm) and macroporous (>50 nm) [10]. Two kinds of PSi were fabricated in this thesis: mesoporous and macroporous. However, in order to underline the difference between them, the mesoporous was labeled as nanoporous silicon (nPSi), and the macroporous as macroporous silicon (mPSi).

nPSi is formed from doped silicon substrates, either n-type or p-type [11]. Normally, pore sizes are in the range of 10-50 nm. Its macroscopic surface is slightly darker-looking compared to bulk silicon, and of excellent smoothness. The inner surface area is high and could easily be etched in low-concentration alkaline solutions.

In the case of p-type, lightly doped Si produces a fine network of pores, whereas heavily doped p-type material produces more columnar structures [12]. Different

parameters such as current density, electrolyte composition (mainly HF concentration), crystalline orientation or process temperature also influence the reaction kinetics and hence the morphology of nPSi [13]. As a result, a wide variety of structures, porosity and pore morphology may be achieved depending on the fabrication parameters [14]. Some of the most representative nPSi morphologies and structures are presented in Fig. 5.

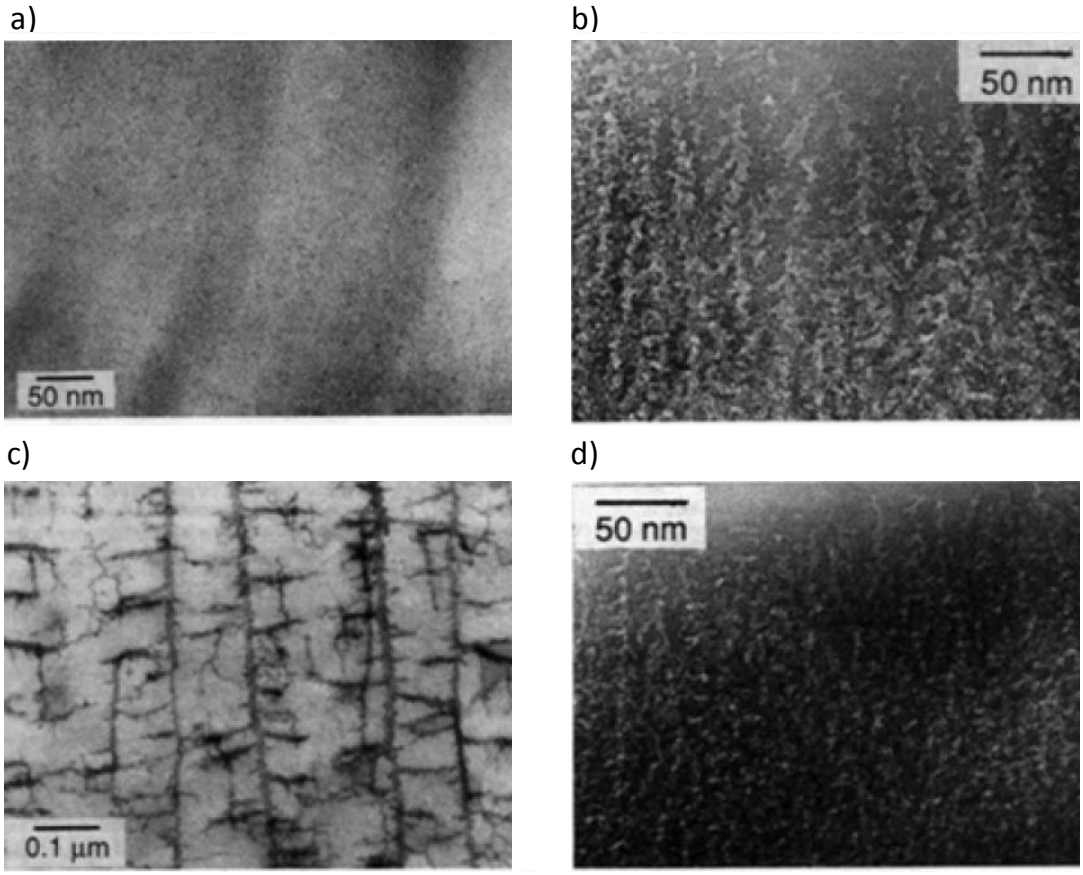

Figure 5. Cross-sectional TEM images showing the basic differences in morphology among different types of nPSi samples from: a) p-type Si, b) p^+-type Si, c) n-type Si, and d) n^+-type Si (from Smith and Collins [14]).

ii) Preparation of nanoporous silicon

The nPSi used in this thesis was fabricated in a homemade Teflon electrochemical cell connected to a potentiostat/galvanostat (HG&G model 263), which is controlled by the computer program Research Electrochmistry 4.3 [9].

nPSi was fabricated by electrochemical etching of 1.5 x 1.5 cm^2 p^+ type Si (boron-doped, orientation <100>, resistivity of 0.01-0.02 Ωcm) in a HF:EtOH solution at 1:2 (*v/v*), HF at 48%. This kind of Si was selected due to its hole availability, which facilitates pore formation [1]. HF was mixed with ethanol in the electrolyte solution in order to improve the infiltration of HF molecules into the PSi pores avoiding the formation of hydrogen bubbles, which may cause an inhomogeneous etching [15]. The HF-ethanol proportion was selected to achieve columnar pores in p^+ type Si, a highly homogenous structure suitable for the formation of PSi-based composites [16].

In order to find a mechanically stable thin nPSi layer to withstand the composites formation steps, a range of current densities and reaction times were tested, from 60 to 120 mA/cm^2 and from 60 to 200 s, respectively. nPSi formation was carried out under illumination with a 150 W halogen lamp; the illumination helped to form more electron-hole pairs in the Si-electrolyte interface, which enhances the Si dissolution resulting in a more homogeneous porosity [9]. Finally, after nPSi synthesis, the samples were rinsed with EtOH and dried with nitrogen.

iii) Macroporous silicon

Usually, mPSi is obtained from low-doped n-type Si [11]. The most critical parameter is the presence of illumination during etching. Regular arrays of pores with pitch ≥2 μm, 1 μm wide and more than 100 μm deep can be obtained. The resistivity of Si should be chosen in agreement with the pitch density, otherwise branching or dying of pores occurs. Also current density should be adjusted according to the desired porosity. In addition, due to the concentration gradients of the electrolyte in the pores, a linearly increasing current density has to be used [1].

Formation of mPSi is more difficult from p-type than n-type Si [11], resulting in relatively short and ‘‘bulgy’’ pores. However, using different kinds of organic electrolytes its synthesis is facilitated and stabilized so that pore depths can be up to 400 μm [17]. Fig. 6 shows examples of different types of p-macropores.

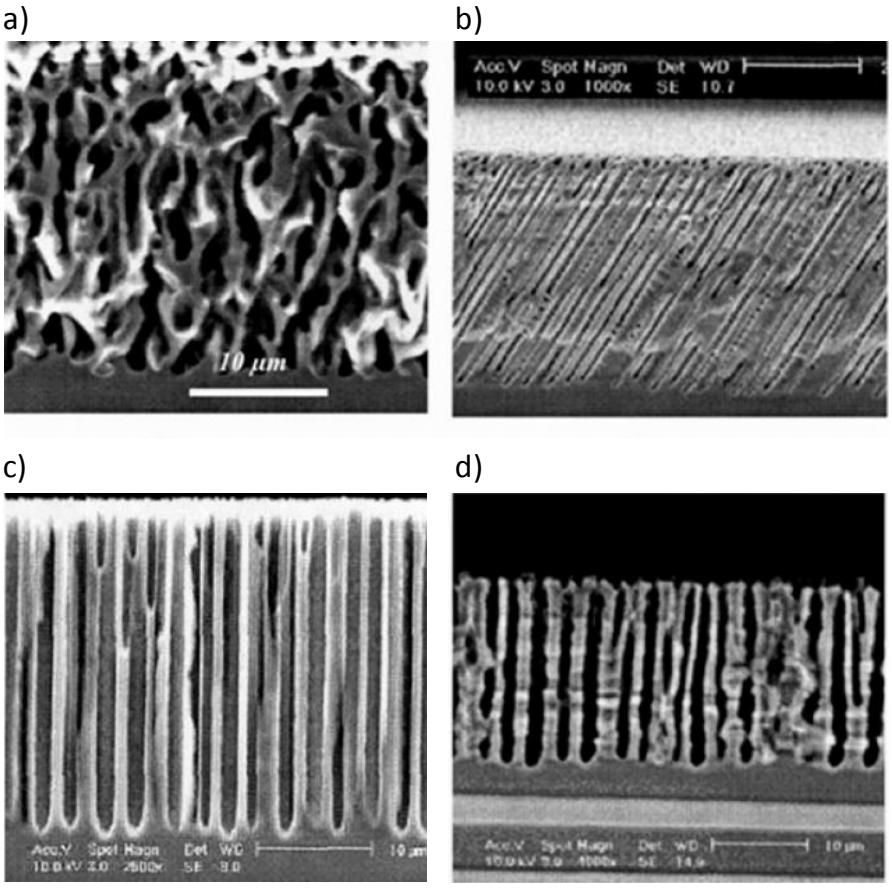

Figure 6. Cross-sectional SEM images of some mPSi samples obtained from p-type Si with 4 wt. % HF in: a) acetonitrile on {1 1 1} Si, b) dimethylformamide on {5 1 1} Si, c) dimethylformamide on {1 0 0} Si (perfect pores) d) acetonitrile + diethyleneglycol (protic additive) on {1 0 0} Si. (from Foll et al. [17])

iv) Preparation of macroporous silicon

As in the case of nPSi, mPSi formation was carried out in a homemade Teflon electrochemical cell.

mPSi was fabricated by electrochemical etching of 1.5 x 1.5 cm^2 p-type Si (boron-doped, orientation <100>, resistivity of 23-31 Ωcm) in a HF:DMF (dimethylformamide, C_2H_6NCOH) solution at 1:6 (*v/v*), HF at 48% [17]. In this case, the macroporuous formation is favored because the higher resistivity of Si wafer produces a lower density of holes at the Si-electrolyte interface, which results in lower surface points of electrochemical etching. The used solvent, DMF, is an organic aprotic solvent (unable to form hydrogen bonds) [18].

Samples were fabricated in ranges of current density and reaction time from 5 to 40 mA/cm^2 and from 300 to 1800 s, respectively. mPSi synthesis was carried out under

illumination with a 150W halogen lamp. After their synthesis, samples were rinsed with EtOH and dried with nitrogen.

v) Porous silicon stabilization: Oxidation

The nanoscale architecture of PSi is inherently fragile [19] and shows a great reactivity due to the chemical instability of the surface just after formation. Rapid modification of the surface occurs if it is not passivated [20]. That is why in some cases PSi is modified to enhance its mechanical and chemical stabilization. Besides, in order to provide PSi surfaces with diverse properties, it is also functionalized using various chemical reactions such as [21]: oxidation, hydrosilylation, cathodization, amino-silation.

One strategy to obtain long-term PSi stability is to oxidize its surface under controlled conditions [22]. Thermal oxidation is the most commonly used technique for the passivation of PSi. It consists on the annealing of porous samples at high temperature in ambient air or under controlled O_2 atmosphere for time intervals ranging from a few tens of minutes to a few hours. In general, temperatures used are within the 300 °C - 1000 °C range. By this process, PSi layers are transformed in SiO_2 [20]:

$$Si + O_2 \rightarrow SiO_2 \qquad \text{(Eq. 1)}$$

Nevertheless, a 300 ºC stabilizing pretreatment prior to higher temperature oxidization is necessary to avoid pore coalescence. The oxygen content at the end of the process varies with substrate, oxidization temperature and duration [1].

Another common stabilization method is chemical oxidation. Depending on the process, the chemical reactions on PSi surface can produce hydroxyl, silyloxy and alkoxy terminated bonds [21]. Different inorganic and organic agents have been used in PSi chemical oxidation, such as hydrogen peroxide, nitric acid or boiling water [1]. In addition to stabilization, oxidation treatments also introduce hydrophilicity to PSi which is an essential requirement in biological applications.

vi) Chemical oxidation: Experimental procedure

This substrate treatment was necessary to enhance the cyclodextrin incorporation into the porous structure. It is well documented that fresh PSi surface is mainly composed of Si-H bonds [23,24]. A simple chemical post-treatment of PSi is using H_2O_2. Its oxidation process involves different reactions: Si-H bonds can be transformed to Si-OH, Si-O-Si or $-O_ySi-H_x$. The oxidation process is represented in the schematic of Eq. 2 [25,26]:

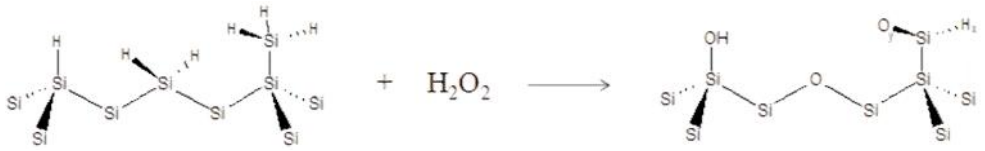

(Eq. 2)

In the case of PSi/cyclodextrin hybrids, both PSi substrates (nPSi and mPSi) were chemically oxidized with H_2O_2 (30% *v/v*) for 2 h [25], rinsed with EtOH and dried with nitrogen. For the synthesis of PSi/calcium phosphate bioceramics, the chemical stabilization was not required.

2.2.2 Preparation of PSi/cyclodextrin hybrids

The processing of PSi/cyclodextrin hybrids was carried out by functionalization of PSi with modified β-cyclodextrin. A brief review of cyclodextrins and the classes of cyclodextrin-based polymers is exposed. Later, the particular *in-situ* procedure of polymerization carried out on PSi samples is detailed.

i) Cyclodextrins

Cyclodextrins (CDs) and their derivatives have been used as building blocks for the development of a wide variety of polymeric networks and assemblies [27]. CD-based polymeric materials, such as hydrogels, nano/microparticles, and micelles, are frequently studied for pharmaceutical and biomedical applications, for example, sustained release [28] and targeted delivery of bioactive substances (low molecular weight drugs, peptides,

proteins, genetic material and others) [29]. Other outstanding but less common applications relate to tissue engineering [30] and medical diagnostics [31].

CDs are non-toxic cyclic polysaccharides with a hydrophilic outer surface (C-OH groups) and a hydrophilic apolar cavity (C-O-C and C-H bonds) [32] (Fig. 7-a). They are built from six to eight (α= 6, β = 7, γ = 8) D-glucose units. The D-glucose units are covalently linked to carbon atoms C_1 and C_4 forming a rigid cavity where guest molecules can be partially or totally enclosed (Fig. 7-b) [33]. Table 2 lists the main characteristics of CDs.

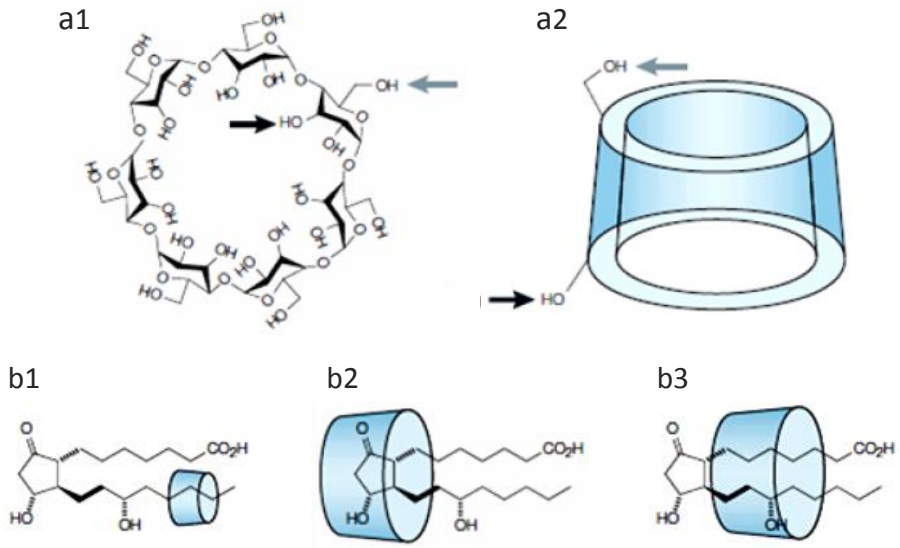

Figure 7. a1) Chemical structure of β-CD, and a2) its toroidal shape. Models of inclusion complexes between prostaglandin E_2 and: a) α-CD, b) β-CD and c) γ-CD (from Davis and Brewster [32]).

Table 2. CD characteristics (from Loftsson and Brewster [34]).

Characteristic	**α-CD**	**β-CD**	**γ-CD**
Number of D-glucose units	6	7	8
Molecular weight (Da)	972	1135	1459
Central cavity diameter (Å)	4.7-5.3	6.0-6.5	7.5-8.3
Water solubility at 25 ºC (g/L)	145	18.5	232

Since each guest molecule is individually surrounded by a CD, this can lead to advantageous changes in its chemical and physical properties [35]:

- Stabilization of light- or oxygen-sensitive substances.
- Modification of the chemical reactivity of guest molecules.
- Fixation of very volatile substances.
- Improvement of solubility of substances.
- Modification of liquid substances to powders by encapsulation.
- Protection against degradation of substances by microorganisms.
- Masking of ill smell and taste.
- Masking pigments or the color of substances.
- Catalytic activity of CDs with guest molecules.

These properties of CDs and their derivatives are also viable to use in applications of other fields such as analytical chemistry, agriculture, food and toilet articles [36].

ii) Classes of cyclodextrin-based polymers and copolymers

It is possible to classify CD-based polymers in four main classes: crosslinked, linear tube, pendent and linear polymer (Fig. 8). CD-crosslinked polymers are three-dimensional crosslinked macromolecular networks formed by polymers and CDs (Fig. 8-a). The crosslinks can be formed by either covalent bonds or physical cohesion forces between the polymer segments such as ionic bonds, hydrogen bonds, van der Waals forces, and hydrophobic interactions [37]. CD-linear tube polymers have a tubular structure (Fig. 8-b). The cylinders can be formed by using molecules that organize the CDs into a tubular configuration, such as cholesterol [38]; then, the polymers are formed from the tubular configurations by crosslinking between the CDs. In the case of CD-pendent polymers and CD-linear polymers, the first ones contain CDs as pendent moieties in a polymer backbone (Fig. 8-c), and the second ones have CDs as part of the polymer backbone (Fig. 8-d) [32].

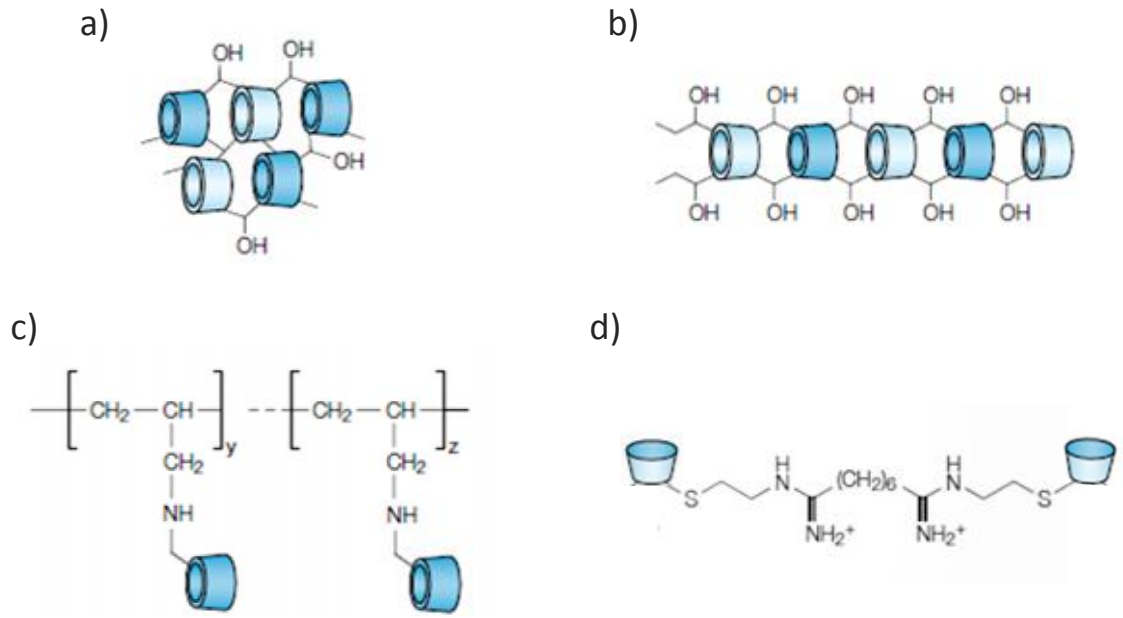

Figure 8. Main classes of CD-based polymers: a) crosslinked, b) linear tube, c**)** pendent, and d) linear polymer (from Davis and Brewster [32]).

iii) PSi functionalization with β-cyclodextrin-citric acid polymer: Experimental procedure

The PSi/CD hybrids were fabricated by means of the protocol developed at Unité Matériaux et Transformations (UMET) of Université Lille 1. Firstly, a monomer solution was prepared with 10 g of β-cyclodextrin (βCD, Roquette, Lestrem France), 3 g of $NaH_2PO_2 \cdot H_2O$ (Aldrich, Saint Quentin Fallavier, France) as catalyst and 10 g of citric acid (Aldrich, Saint Quentin Fallavier, France) in 100 mL of distilled water. Oxidized nano and macroporous silicon samples (nPSi-COx and mPSi-COx, respectively) were immersed in this solution for 15 min with stirring. Afterwards, the excess of monomer solution on the top surfaces was carefully removed by capillarity using a soft cellulosic tissue, leaving a thin film on the top. The samples were dried, first at room temperature, and later at 90 °C for 1 h in each case. The polymerization [39] in PSi samples was carried out at 140 °C for 25 min thereby obtaining the nPSi-CD and mPSi-CD samples. Afterwards they were washed with distilled water for 15 min with stirring, rinsed with EtOH and dried at 90 ºC for 1 h.

The crosslinked polymer obtained (polyCD) by βCD and citric acid is due to a polyesterification mechanism between hydroxyl groups of βCD and carboxylic groups of citric acid, which contains three carboxylic groups as detailed in the following equation (Eq. 3) [39].

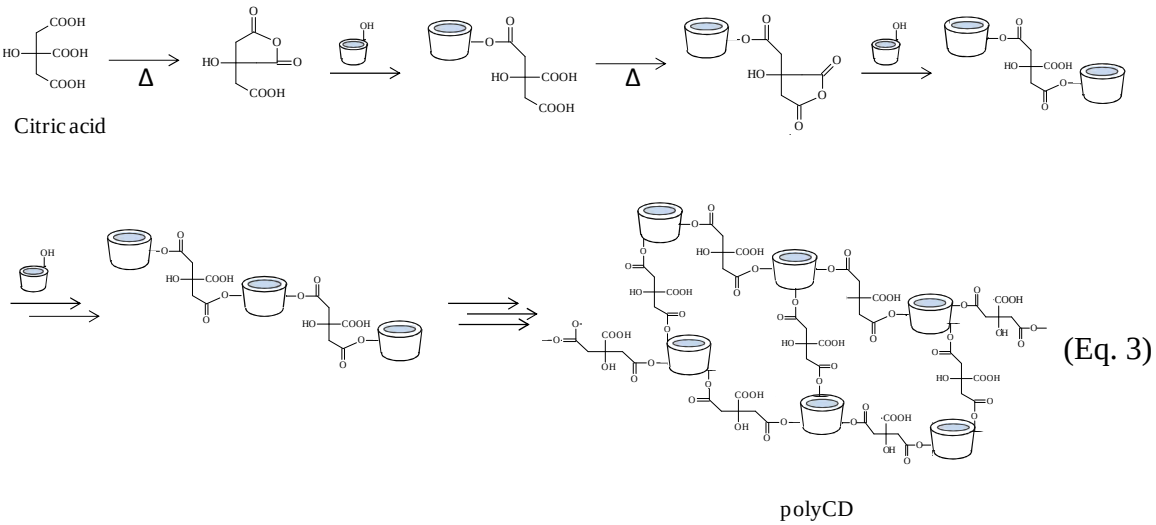

(Eq. 3)

A global scheme of PSi/CD hybrid synthesis is illustrated in Fig. 9.

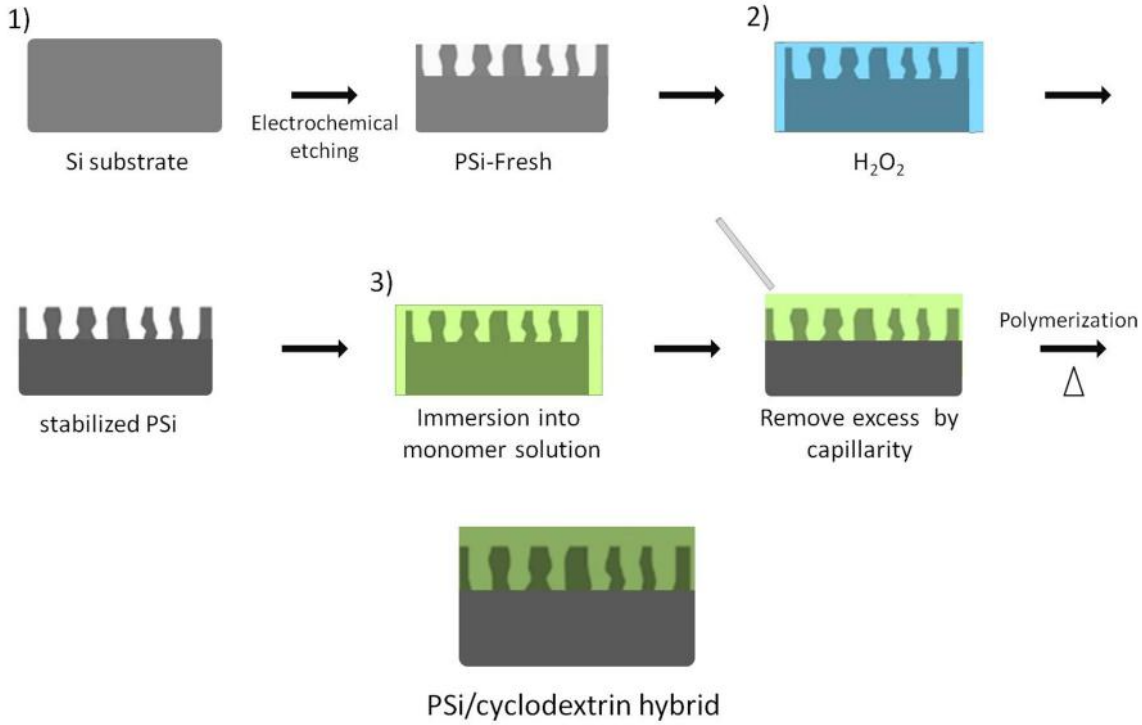

Figure 9. Synthesis scheme of porous silicon-cyclodextrin hybrids: 1) synthesis of nano and micro porous structures, 2) chemical oxidation, 3) cyclodextrin polymerization.

2.2.3 PSi/calcium phosphate bioceramics synthesis

The PSi/calcium phosphate bioceramics were fabricated by calcium phosphate coating on nPSi, at room temperature, from independent solutions of calcium and phosphate by two different deposition methods: cyclic spin coating and cyclic electrochemical activation. Below, a brief fundamental review of calcium phosphates and both deposition techniques used (spin coating and electrochemical deposition) are explained. Besides, the particular experimental procedure of calcium phosphate cyclic deposition on nPSi by each method is detailed.

i) Calcium phosphates

Calcium phosphates (CaPs) are calcium salts of the tribasic phosphoric acid (H_3PO_4), and thus the chemical composition of many CaPs includes $H_2PO_4^-$, HPO_4^{-2}, and/or as incorporated water. Diverse combinations of oxides of calcium and phosphorus (both in the presence and absence of water) provide a variety of CaPs, which are distinguished by the type of the phosphate anion: ortho- (PO_4^{-3}), meta- (PO_4^-), pyro- ($P_2O_7^{-4}$), and poly- ($(PO_3)_n^{-n}$) [40]. Some relevant properties of different CaPs are shown in Table 3.

The importance of CaPs in the field of biomedicine arises from the fact that they constitute the major mineral component of bones and teeth [41]. Due to their compositional similarities to bone mineral and to their excellent biocompatibility, they are the most widely used bone substitutes in bone tissue engineering [42]. Besides, recent studies have shown that some CaPs also exhibit osteoinductive properties, and not only osteoconductive [41]. Thus, these materials can induce osteogenic differentiation *in vitro* or *in vivo* and not only act as substrates for bone deposition.

There are different techniques to produce CaP coatings including biomimmetic growth [43], sol-gel processes [44], plasma spraying [45], sputtering [46], laser ablation [47] or electrodepostion [48]. In this thesis spin coating (a sol-gel derived process) and electrochemical deposition techniques were used so that their characteristics are briefly explained.

Table 3. Properties of different calcium phosphates (from Bose and Tarafder [42]).

Calcium phosphates	**Chemical formula**	**Ca/P molar ratio**	**Solubility**
Monocalcium phosphate monohydrate	$Ca(H_2PO_4)_2 \cdot H_20$	0.5	7.2×10^{-2}
Monocalcium phosphate	$Ca(H_2PO_4)_2$	0.5	7.2×10^{-2}
Dicalcium phosphate dihydrate	$CaHPO_4 \cdot 2H_20$	1.0	2.5×10^{-7}
Dicalcium phosphate	$CaHPO_4$	1.0	1.26×10^{-7}
Calcium pyrophosphate	$Ca_2O_7P_2$	1.0	-
Octacalcium phosphate	$Ca_8H_2(PO_4)_6 \cdot 5H_20$	1.33	2.51×10^{-97}
α-Tricalcalcium phosphate	$\alpha\text{-}Ca_3(PO_4)_2$	1.5	3.16×10^{-26}
β-Tricalcalcium phosphate	$\beta\text{-}Ca_3(PO_4)_2$	1.5	1.25×10^{-29}
Amorphous calcium phosphate	$Ca_3(PO_4)_2 \cdot nH_20$	1.2-2.2	[a]
Calcium-deficient hydroxyapatite	$Ca_{10-x}(HPO_4)_x (PO_4)_{6-x}(OH)_{2-x}$ $(0<x<1)$	1.5-1.67	[b]
Carbonated apatite	$Ca_5(PO_4,CO_3)_3$	1.67	-
Hydroxyapatite	$Ca_{10}(PO_4)_6(OH)_2$	1.67	2.35×10^{-59}
Oxyapatite	$Ca_{10}(PO_4)_6O$	1.67	-
Tetracalcium phosphate	$Ca_4O(PO_4)_2$	2.0	1×10^{-38}- 1×10^{-44}

[a]Solubility varies due to its metastable nature
[b]Solubility varies depending on the stoichiometry

Normally, CaPs can be formed under different pH conditions from slightly acidic to strongly basic [40], depending on the CaP to synthesize and the technique used. It is very important to mention this variable because PSi gets dissolved when submerged into basic solutions [49]. This factor was paramount to consider in PSi/calcium phosphate bioceramics synthesis.

ii) Spin coating deposition

The typical spin coating deposition involves the application of a solution on a substrate followed by acceleration of the substrate at a specific rotational speed (Fig. 10). Alternatively, the solution may be applied while the substrate is spinning. The thickness

and morphology of the film obtained from a particular material in a given solvent at a given concentration is highly reproducible. These three properties depend highly on rotational speed, viscosity, volatility, diffusivity, molecular weight and concentration of the solutes [50]. There is also a shift dependence on the amount of solution deposited, the rate of deposition and the spinning time.

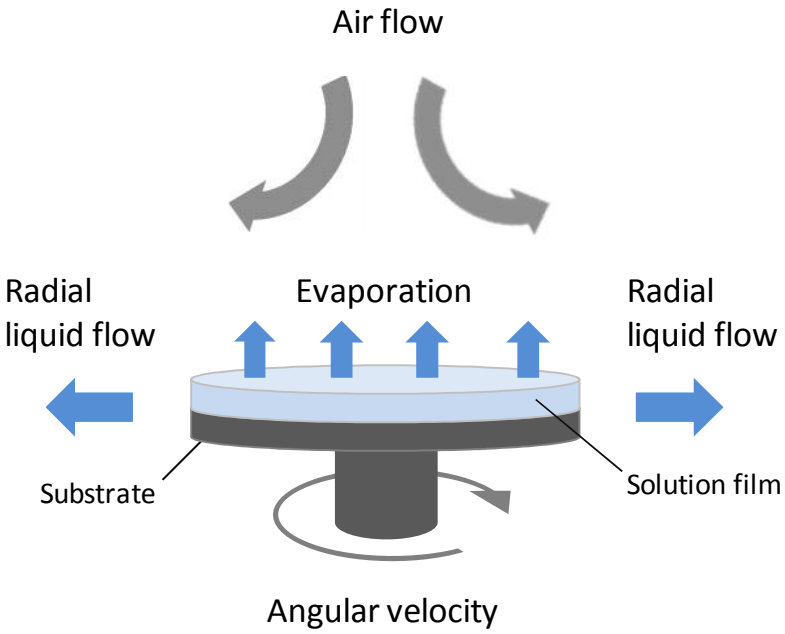

Figure 10. Schematic illustration of the spin coating.

iii) Calcium phosphate deposition by cyclic spin coating: Experimental procedure

CaP deposition by cyclic spin coating (CSC) was carried out using independent calcium (Ca) and phosphate (P) precursor aqueous solutions: 0.1M $CaCl_2$:EtOH at 2:1 (*v/v*) at pH = 5.5 and 0.1M Na_3PO_4:EtOH at 2:1 (*v/v*) adjusted to pH = 7.2 with H_3PO_4, respectively. The standard deposition consisted on alternating 100 µL of Ca and the same quantity of P solution onto a nPSi layer rotated by spin coating at 2500 rpm during 60 s. This process was repeated for ten cycles in a row (Fig. 11). Additionally, CaP was synthesized at different ratios of Ca/P solution volumes (V_{Ca}/V_P = 1, 1.67, 2). Additional experiments were performed under different pH of P solution (pH = 7.2, 9.7, 12.3). All reactions were carried out with fresh Ca and P solutions stirred at room temperature.

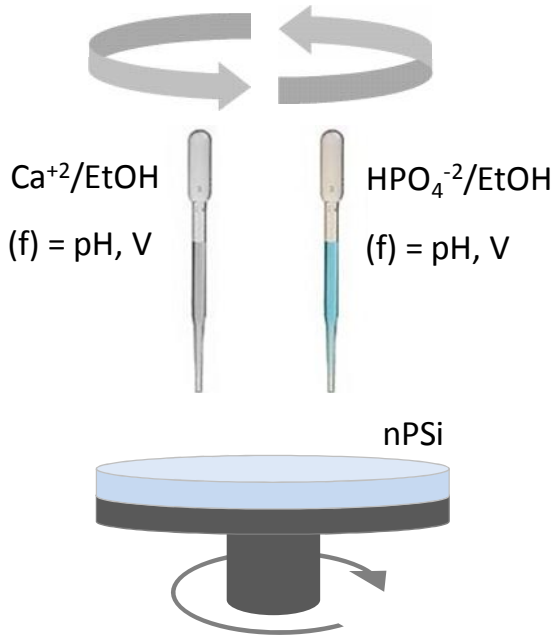

Figure 11. Scheme of CaP deposition on nPSi by CSC.

iv) Electrochemical deposition

The reduction of metal ions M^{+n} in aqueous solution is represented by:

$$M^{+n}_{solution} + ne^- \rightarrow M_{Lattice} \qquad \text{(Eq. 4)}$$

This can be accomplished by means of two different processes: an electrodeposition process in which *z* electrons (e^-) are provided by an external power supply, or an electroless (autocatalytic) deposition process in which a reducing agent in the solution is the electron source (no external power supply is involved). Both processes, electrodeposition and electroless deposition, constitute the electrochemical deposition technique [51]. Fig. 12 shows a cell scheme used for electrochemical deposition and Table 4 compares the nature of reactions occurring in it.

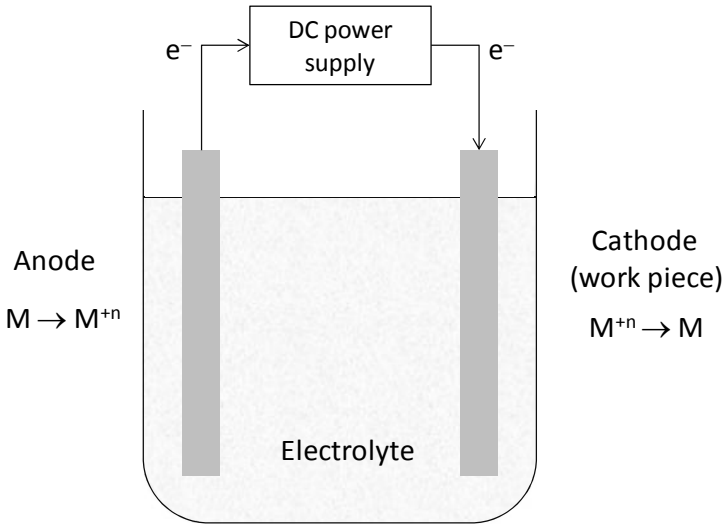

Figure 12. Cell scheme used for electrochemical deposition.

Table 4. Nature of reactions and their sites occurring in electrodeposition (from Rao and Trivedi [52]).

Property	**Electrodeposition**	**Electroless deposition**
Driving force	External power supply	Reducing agent (RA) and autocatalytic property of the deposited metal
Cathode reaction	$M^{n+} + ne^- \rightarrow M$	$M^{n+} + RA \rightarrow M$
Anodic reaction	$M - ne^- \rightarrow M^{n+}$	$RA - ne^- \rightarrow (RA)_{Oxidized\ form}$
Overall reaction	$M_{anode} \rightarrow M_{cathode}$	$M^{n+} + RA \rightarrow M + (RA)_{Oxidized\ form}$
Anodic site	Anode itself	Work piece
Cathodic site	Work piece	Work piece

v) Calcium phosphate deposition by cyclic electrochemical activation: Experimental procedure

The CaP deposition on nPSi by cyclic electrochemical activation (CEA) was performed using the same Ca and P aqueous solutions than in CSC: 0.1M $CaCl_2$:EtOH at 2:1 (*v/v*) at pH 5.5 and 0.1M Na_3PO_4:EtOH at 2:1 (*v/v*) adjusted to pH = 7.2 with H_3PO_4, respectively. The electrodeposition of CaP on nPSi was carried out by applying a cathodic

current to the Ca solution and an anodic current to the P solution under illumination. Every deposition resulted from the application of 20 Ca/P cycles (30 s each) by means of a potentiostat/galvanostat (HG&G model 263) (Fig. 13). Experiments were done at three different Ca/P current density ratios (I_{Ca}/I_P = 1, 1.67, 2, keeping the P current density constant at 1 mA/cm^2) and at three different Ca/P reaction time ratios (t_{Ca}/t_P = 1, 1.67, 2, keeping the P reaction time fixed at 30 s). All reactions were carried out with fresh Ca and P solutions at room temperature.

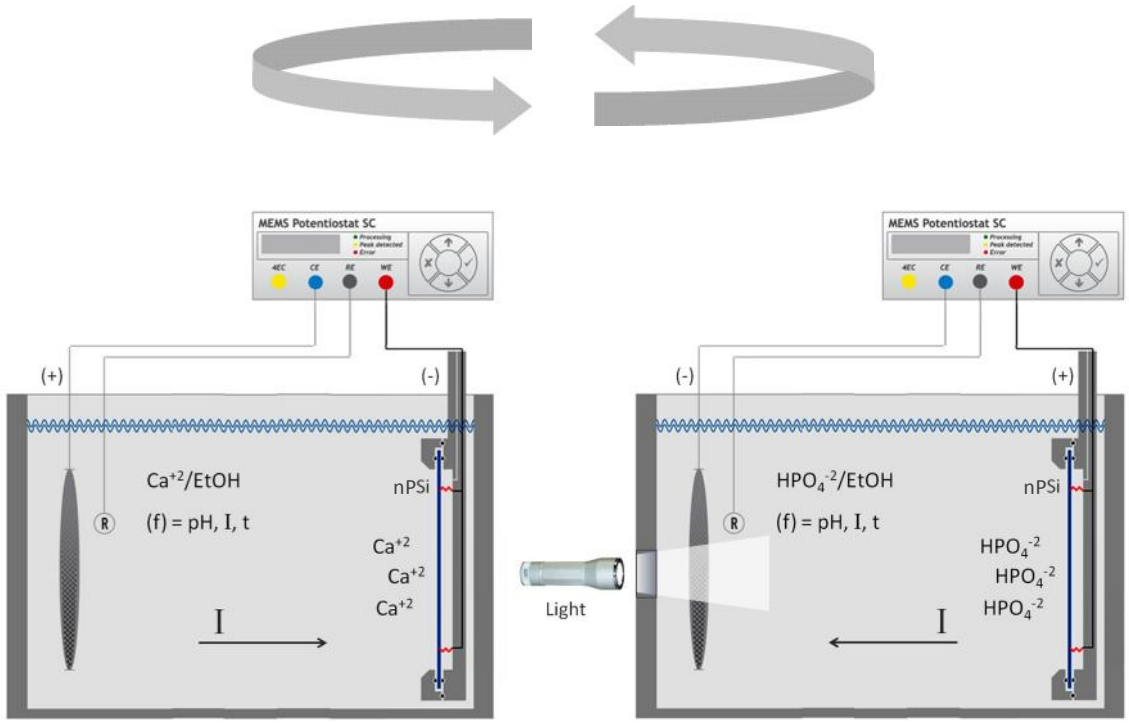

Figure 13. Scheme of CaP deposition on nPSi by CEA.

2.3 Characterization techniques

In this section, the basic principle of each technique used to characterize the biocomposites is briefly explained, as well as their respective utilization parameters. The characterization techniques are organized in four sub-sections: microscopy, physicochemical techniques, *in vitro* cell assays and drug release profiles.

2.3.1 Microscopy

i) Scanning Electron Microscopy (SEM) and Field Emission Electron Microscopy (FESEM)

A scanning electron microscope uses a collimated and focused beam of high-energy electrons to produce images from a sample's surface [9]. The electron beam is generated by a gun usually located at the top of a high vacuum column (Fig. 14). The electron beam is accelerated by a potential up to 50 kV, while is collimated and focused by electromagnetic lenses. When it reaches the sample, the electron beam scans the sample surface by a series of deflection coils. Two independent detectors collect the secondary electrons for images with better resolution, and the backscattered electrons for topographic, compositional or electronic maps.

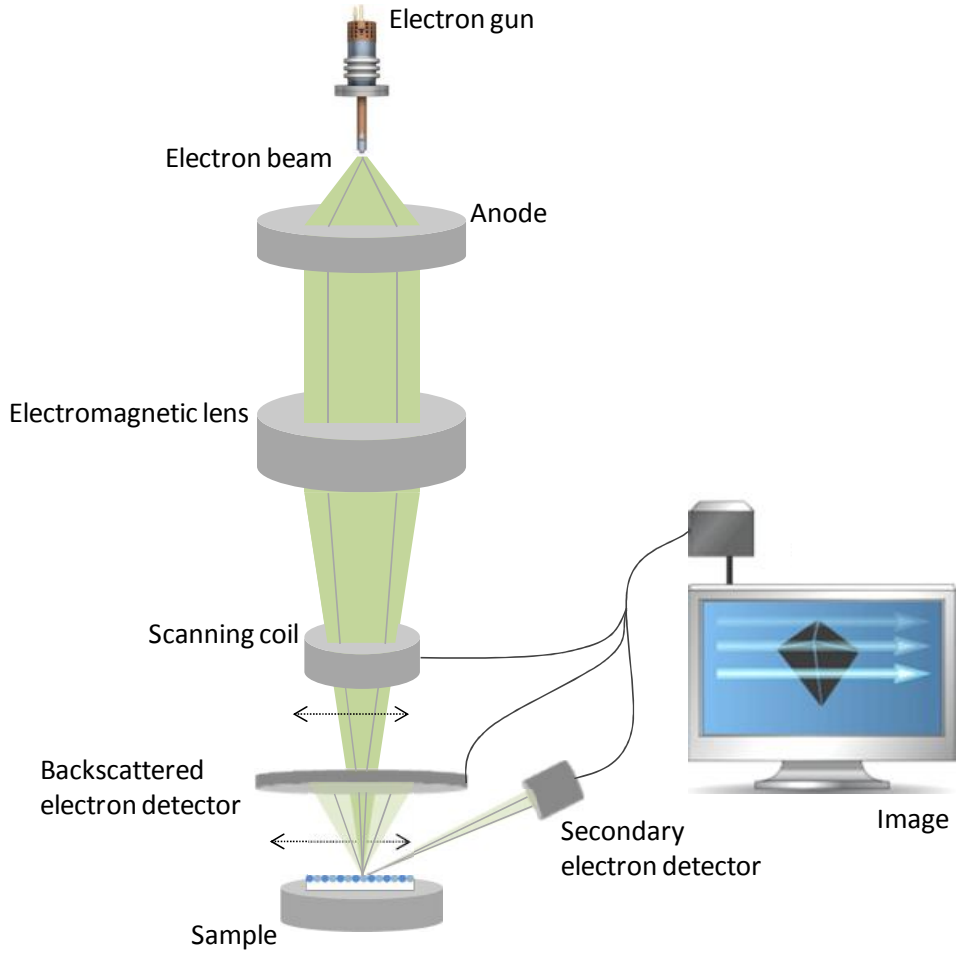

Figure 14. Schematic design of a scanning electron microscope.

The difference between SEM and FESEM is that the FESEM electron gun has a much smaller emission area than the traditional thermionic guns used in SEM, which gives rise to brighter sources and a smaller scanning beam diameter [9]. In turn, as the emission in FESEM is produced by tunnel effect, the energy spread of emitted electrons is significantly reduced, leading to an induction of chromatic aberration. This allows reducing the acceleration voltage of analysis, thereby reducing damage to the samples and charge effects. Thus, images with higher resolution can be obtained.

The microstructure and morphology of PSi and composites were studied by using a conventional SEM (Hitachi S-3000N) detecting secondary electrons and/or a FESEM (Philips XL-40FEG), operated at 20 keV and 10 keV, respectively. Both are facilities at Servicio Interdepartamental de Investigación (SIdI), Universidad Autónoma de Madrid.

ii) Atomic Force Microscopy (AFM)

Images obtained by an atomic force microscope are obtained by detecting the forces between a sample and a probing tip, which is attached to a cantilever [53]. In response to the force between sample and tip, the cantilever is deflected. As the samples are mounted on a piezoelectric base, the images are taken by scanning the sample relative to the probing tip and registering the deflection of the cantilever and/or the z-movement of the piezoelectric as a function of “x” and “y” positions (Fig. 15).

Two main operational modes are distinguished in AFM: contact and non-contact mode. When AFM is operated in non-contact mode, the interaction forces can be resolved up to distances of 10 to 100 nm, such as Van der Waals, electrostatic, magnetic or capillary forces [54]. If the cantilever is vibrated at a constant frequency, the AFM is called tapping mode. In contact mode, the AFM can reach a distance in the order of Å between the probing tip and sample. In this mode, ionic repulsion forces allow the surface topography to be traced with high resolution (it is possible to achieve atomic resolutions). Besides, frictional forces and elastic or plastic deformations can be detected under appropriate conditions.

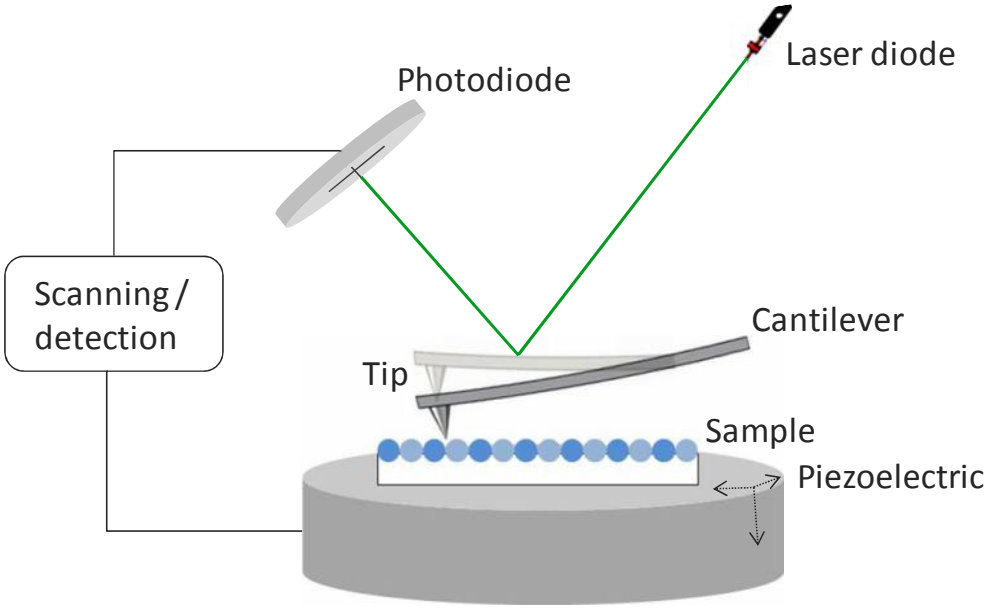

Figure 15. AFM scheme with reflective light detection.

This technique was utilized in tapping mode to study the roughness and topography of PSi substrates, before and after functionalization with polyCD. A NT-MDT Solver equipped with a Smena head and Si cantilevers (force constant 5 N/m, first harmonic frequency of 158 KHz) were used. To generate topographic images and to calculate sample roughness, the NT-MDT SPM Software was used on scanning areas of 4x4 μm^2. The equipment was provided by the Institute for Health and Consumer Protection of the Joint Research Centre in Ispra, Italy.

iii) Immunofluorescence Microscopy

The luminescence principle of fluorophores consists on electronic transitions in a band structure between molecular levels [54]. In Fig. 16 an electronic energy diagram corresponding to a fluorophore is represented. It consists on a singlet ground S_0, a singlet excited state S_1 and an intermediate triplet T_1 of longer lifetime. Light absorption promotes electron excitation and subsequent emission (fluorescence).

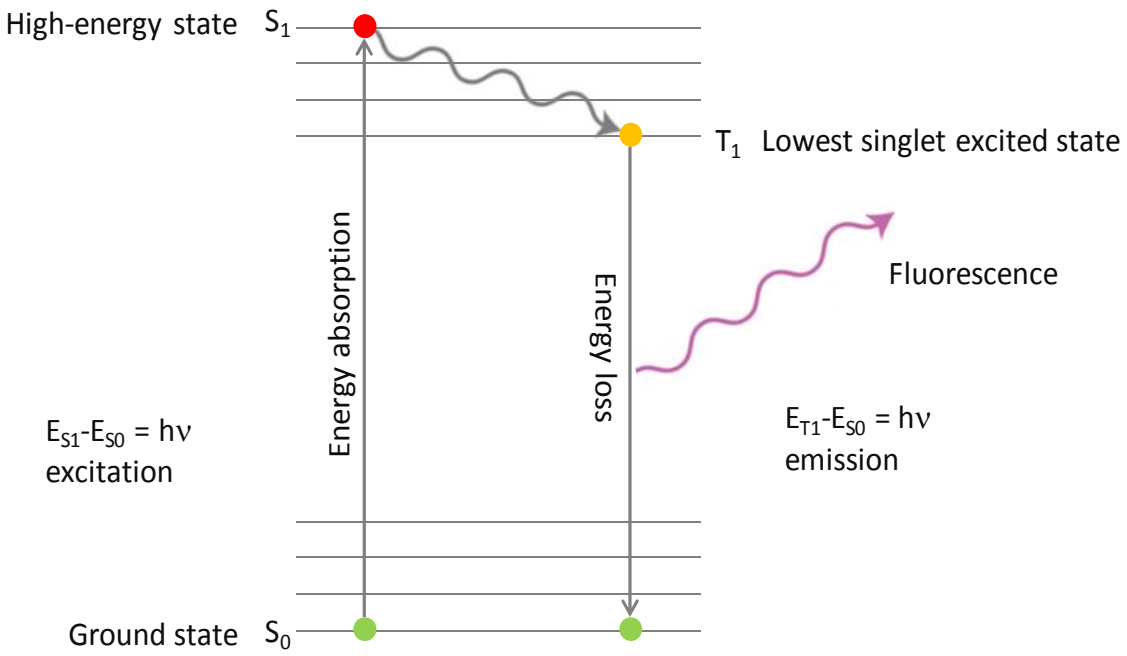

Figure 16. Schematic representation of an energy diagram (Jablonsky diagram) corresponding to a fluorophore: Excitation and emission.

Immunofluorescence microscopy is mainly used to evaluate cells in suspension, cultured cells, tissues, beads and microarrays for the detection of specific proteins [55]. In most cases the sample of interest is labelled with a fluorescent substance known as a fluorophore and then illuminated through the lens with an UV source. The illumination light is absorbed by the fluorophores (now linked to the sample) and causes them to emit a longer wavelength light. This light is separated from the surrounding radiation with filters, which allow seeing only the fluorescent wavelength (Fig. 17).

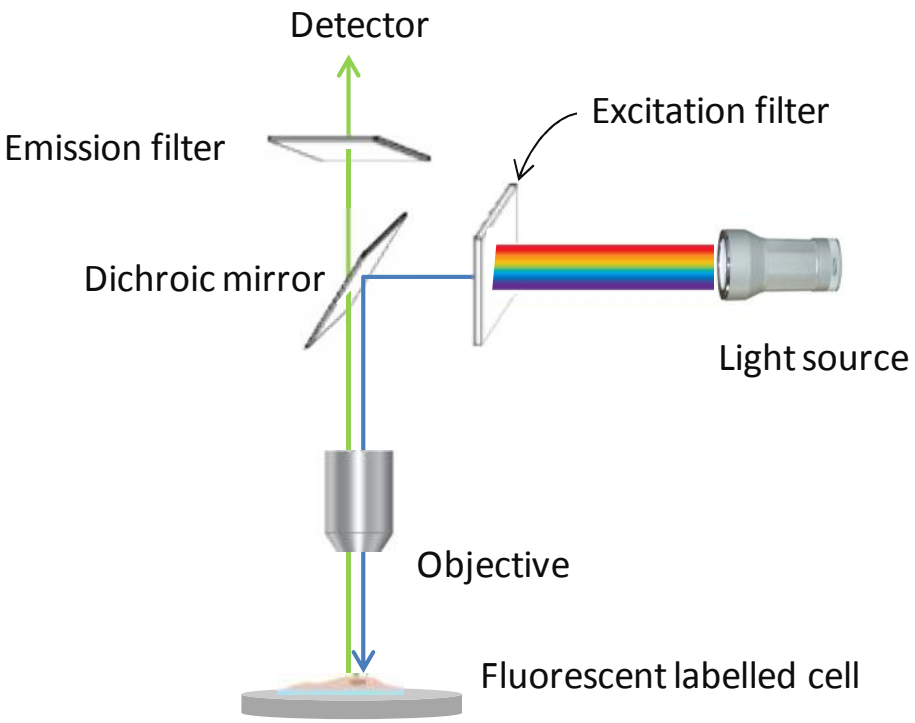

Figure 17. Scheme of a fluorescence microscope.

An inverted fluorescence microscope (Olympus IX81) coupled to a CCD colour camera was used to observe human mesenchymal stem cells (hMSCs) used during the evaluation of the biocompatibility of the PSi/CaP composites. Phalloidin-Alexa 488 and Dapi were used as fluorophores. This microscope is a facility at Departamento de Biología Molecular, Universidad Autónoma de Madrid.

2.3.2 Physicochemical techniques

i) Gravimetric analysis

Gravimetry is a quantitative determination of an analyte based on its mass. The porosity of a solid is defined as the fraction of void within the structure, which can be easily determined by gravimetric measurements. In the case of PSi, the Si wafer is weighted before anodization (m_1), just after anodization (m_2), and after a rapid dissolution of the whole porous layer in a 3% KOH solution (m_3) [1]. Then, porosity is given by the following equation:

$$P(\%) = \frac{(m_1 - m_2)}{(m_1 - m_3)} \qquad \text{(Eq. 5)}$$

This technique was carried out using an automatic standard micro and analytical balance of readability of 0.01 mg (RADWAG AS 60/C/2).

ii) Direct galvanostatic method

The direct galvanostatic method is a typical electrochemical technique used for the study of electrode kinetics in constant current electrodeposition by means of recording the potential-time characteristic (Fig. 18) [56]. The equipment used for these measurements was a potentiostat/galvanostat (HG&G model 263).

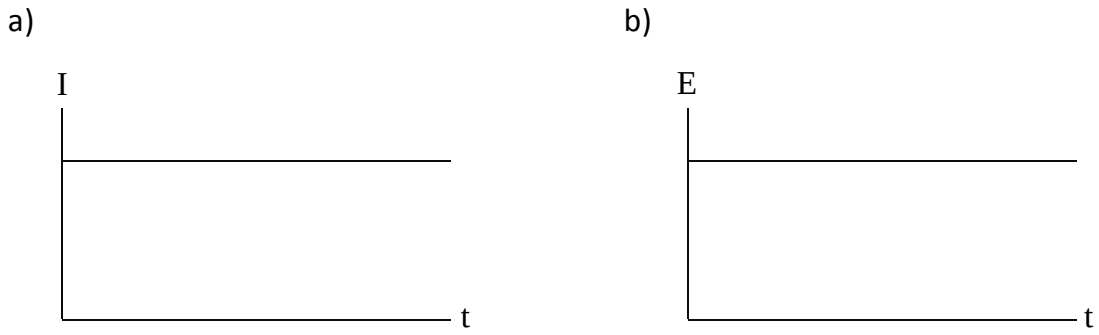

Figure 18. The input (a) and response (b) in a direct galvanostatic measurement.

iii) Water contact angle

The water contact angle is a technique that measures the wettability of solid surfaces [57], that is to say, it allows knowing if a solid surface is hydrophilic or hydrophobic. This is achieved by measuring the intrinsic contact angle (θc) formed by a water drop on a solid surface (rigid, chemically inert and not soluble) (Fig. 19). In general, if a surface has a $\theta c < 90^{o}$ it is considered hydrophilic, but if the $\theta c > 90^{o}$ is considered hydrophobic [58].

The surface wettability of samples was evaluated with a water contact angle goniometer (KSV CAM-101) used on the static sessile drop mode: a 5μL drop of water was applied onto the sample surface and the contact angle formed with the surface was measured. Each measurement was repeated five times. The statistical data obtained were processed by Statgraphics Centurion XV.

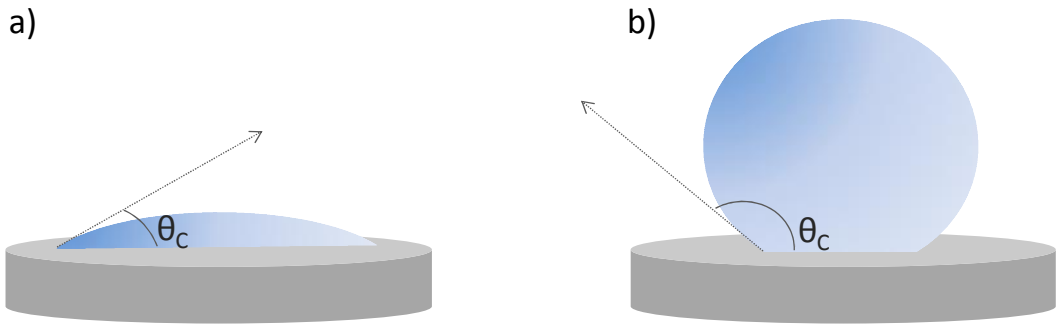

Figure 19. a) Hydrophilic surface, and b) hydrophobic surface.

iv) Toluidine Blue Ortho (TBO) titration

Toluidine blue ortho (TBO) (Fig. 20) is a cationic (basic) dye that interacts electrostatically with negatively charged groups and can be easily detected by light absorption in the blue region. By means of titration, it is currently employed in a variety of applications as a labeling agent, photosensitizer, or mediator for chemical reactions, but is used especially in the medical field to mark or target acidic compounds using high pH solutions [59].

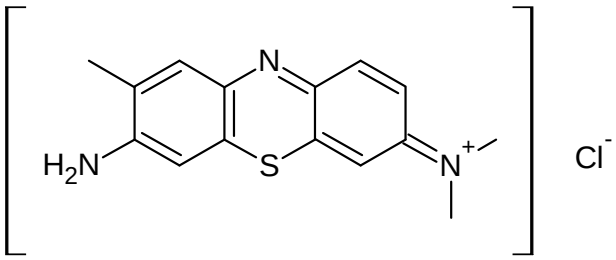

Figure 20. TBO molecule, a cationic dye.

As PSi/CD hybrids presents free carboxylate groups carried by the citrate crosslinks, the carboxylic group density on samples (μmol COOH/cm^2 and μmol COOH/mg) was calculated using TBO titration [60]. Samples were submerged into a 0.5 mM TBO (Aldrich) solution (pH 10, adjusted by NaOH) at 30 ◦C for 4 h. Non-complexed TBO was rinsed with 50 mL of 0.1 M NaOH for 2 min. Complexed TBO was

desorbed from samples with 10 mL of 50% (*v/v*) acetic acid for 30 min. The desorbed TBO in acetic acid was quantified by UVvisible spectrophotometry (UV-1800 spectrometer, Shimadzu) at 634 nm and the density of COOH functions was calculated according to a mole-to-mole complex between TBO and accessible COOH groups [59].

v) Thermogravimetric Analysis (TGA)

According to Brown [61], a thermal analysis "monitors the change in a property of a sample, which is related to an imposed temperature alteration". In the case of thermogravimetric analysis (TGA), changes in weight are measured as a function of increasing temperature [62]. TGA provides information related to the physical and chemical phenomena listed in Table 5.

Table 5. Related information of physical and chemical phenomena provided by TGA [62].

Physical phenomena	**Chemical phenomena**
Fusion	Chemisorption
Vaporization	Desolvation (especially dehydration)
Sublimation	Decomposition
Absorption	Oxidative degradation
Adsorption	Solid-state reactions
Desorption	Solid-gas reactions (i. e. oxidation, reduction)

The TGA technique was used in the characterization of PSi/CD hybrids, which was performed in a TA-Q50 apparatus (TA Instruments) to determine the quantity of organic polyCD fixed onto the PSi samples. Measurements were recorded in the 30-700°C temperature range with a heating rate of 10°C/min in a 90% O_2-10% N_2 atmosphere. The used equipment was installed in UMET, Université Lille 1.

vi) X-ray Diffraction (XRD)

X-ray diffraction (XRD) is a technique primarily used to characterize the crystalline components of a material [63]. XRD is most widely used for identification of crystalline phases, preferred crystal orientation, periodicity and symmetry of a crystal, grain size, strain and crystal defects. In a typical XRD analysis a monochromatic Cu-K_α radiation (λ = 0.154 nm) is incised at a θ angle (0-90º) on a sample and the diffracted intensity is detected at a 2θ angle. The fundamental of XRD is based on the pattern generated by the X-rays diffracted by the atomic planes of the crystal (Fig. 21-b). This phenomenon is described by the Bragg's law.

The Bragg's law relates the incident X-ray angle to a length in real space [64]:

$$d_{hkl} = \frac{n\lambda}{2sin\theta} \qquad \text{(Eq. 6)}$$

where d_{hkl} is the distance between the atomic planes; n is an integer number; λ the X-ray wavelength and θ is the X-ray angle of incidence.

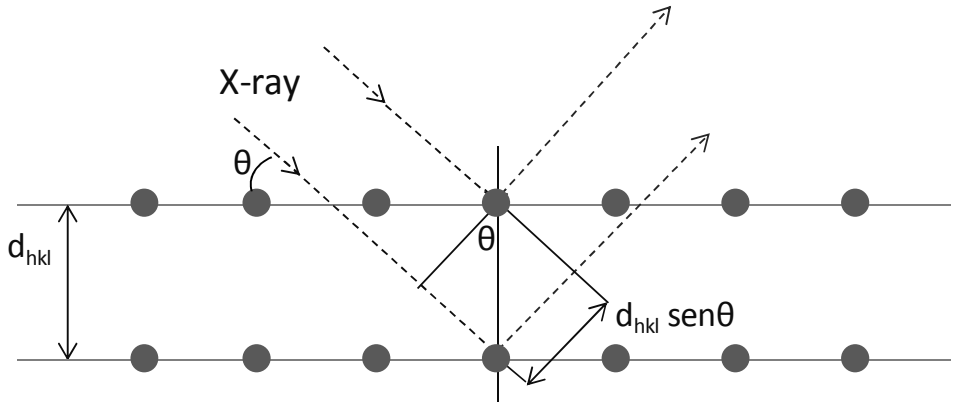

Figure 21. Schemes of the Bragg's law.

The crystalline structure of PSi/CaP bioceramics was determined by glazing angle X-ray diffraction (GA-XRD) with a Siemens D5000 diffractometer using Cu-Kα radiation (λ = 1.54 Å). The analysis was performed at a fixed angle of 0.5º from θ= 10º to θ= 60º with increments of Δθ= 0.04º and accumulation times of 8 s. The glazing angle mode was selected because is more sensitive to particles deposited on a surface. GA-XRD measurements were carried out in SIdI facilities.

vii) Ultraviolet-visible Spectroscopy (UV-Vis)

For liquid systems, ultraviolet-visible spectroscopy refers to the use of light in the ultraviolet/visible range to measure chemical concentrations [65]. When a molecule that contains valence electrons of low excitation energy absorbs UV-Vis radiation, the electron energy is promoted to an excited state. This produces a continuous absorption band, which results in different possible electronic transitions. The electron transitions for *n*, π, and σ bonding orbitals are shown in Fig. 22.

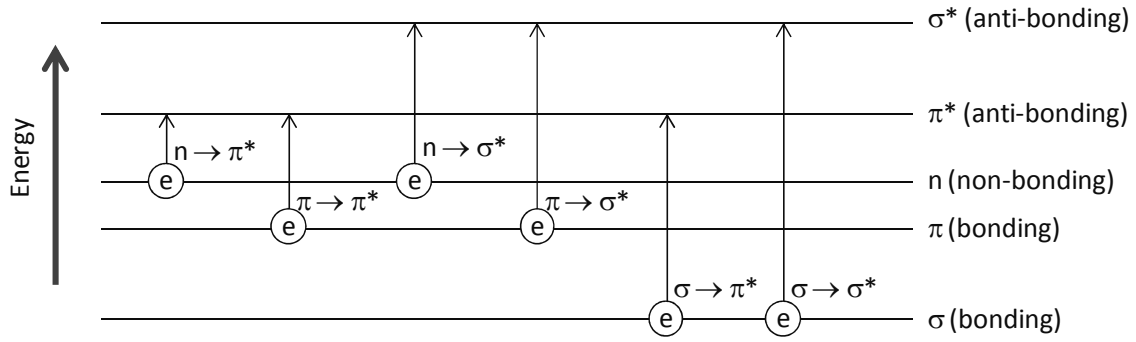

Figure 22. Absorption of light increases the energy of a molecule.

The absorbance (A) is defined as [65]:

$$A = -log_{10}\left(\frac{I}{I_0}\right) \qquad \text{(Eq. 7)}$$

where I_0 is the intensity of the radiation before it passes through the solution (incident radiation); and I is the intensity of the radiation after passing through the solution. In Fig. 23, a scheme of a double beam UV-Vis spectrophotometer is illustrated.

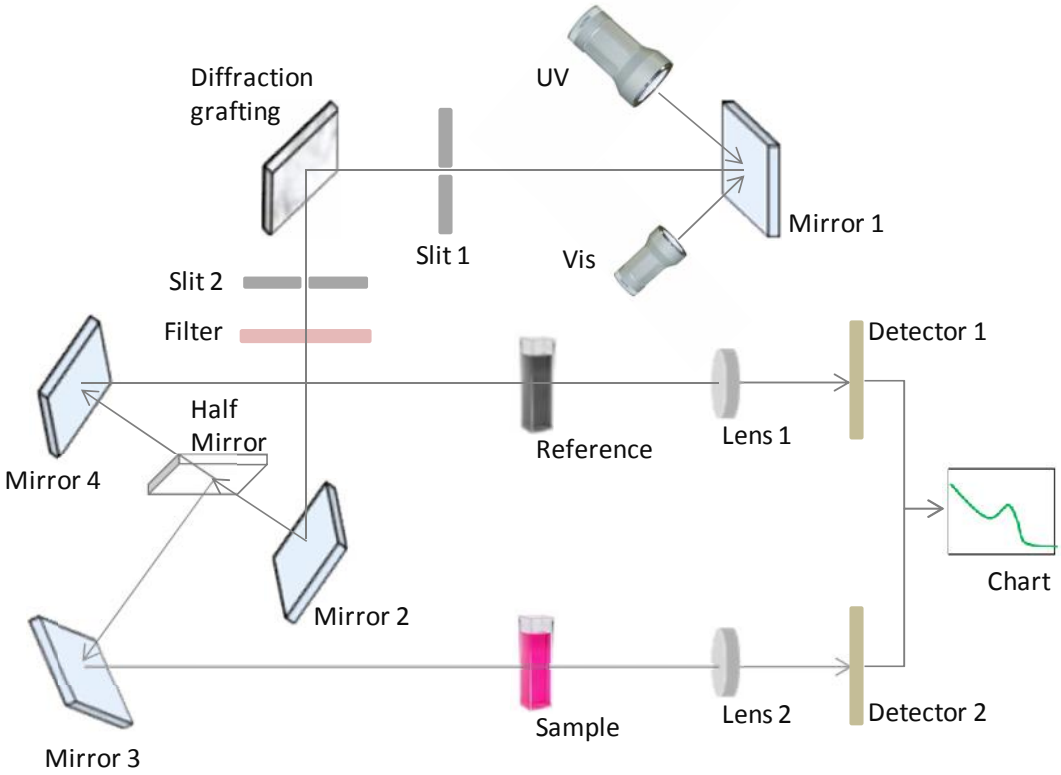

Figure 23. Schematic diagram of a double-beam UV-Vis spectrophotometer.

An UV–visible spectrophotometer (UV-1800 spectrometer, Shimadzu) was used for the elaboration of drug release profiles (Section 2.2.3) according to protocol from UMET of Université Lille 1. The spectrophotometer was used under the absorption mode in the range of wavelength of light from 300 to 200 nm with a resolution of 1 nm.

viii) Energy Dispersive X-ray Spectroscopy (EDX)

Energy Dispersive X-ray Spectroscopy (EDX) is an analytical technique used for the elemental analysis or chemical characterization of a sample. Usually, it is incorporated to a SEM microscope. When an electron beam (at ~10 keV) collides with the sample (Fig. 24), it creates a vacancy in an atomic inner level due to an electron displacement from K-shell. Then, the vacancy is filled by an electron from an upper shell, which induces a dissipation of energy in the form of a characteristic X-ray emission from the element involved in the transition [16].

The EDX equipment used was an INCA X-sight from Oxford Instruments within the SEM of SIdI.

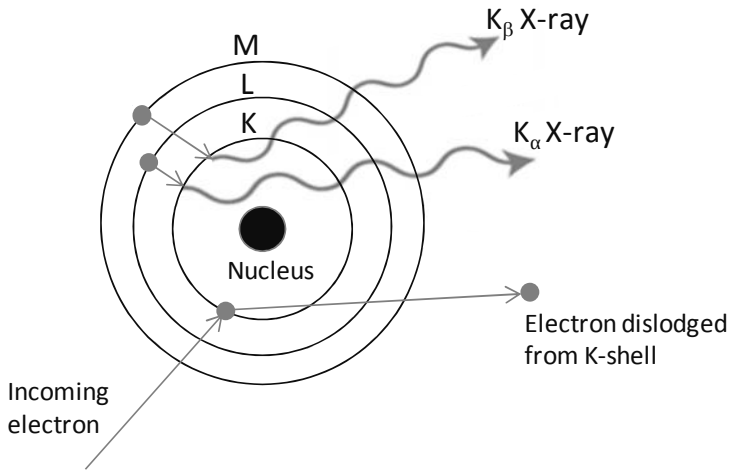

Figure 24. Scheme of the X-ray emission in EDX.

ix) Fourier Transform Infrared Spectroscopy (FTIR)

Fourier Transform Infrared Spectroscopy (FTIR) is a technique mainly used to detect functional groups in a molecule. Although it can be used for both qualitative and quantitative analysis, it is most commonly used as a qualitative technique. FTIR is a technique based on measuring the power density and the optical path, which forms a Fourier pair with the light intensity and the wave number of the electromagnetic radiation [54]. In Fig. 25, a Michelson interferometer system is schematized. The beam from the infrared source is incident on a splitter, where the beam is divided into two parts. The reflected part is directed to a sliding mirror, which allows varying the optical path. The transmitted beam is reflected to a fixed mirror, which carries both beams into a current signal to the detector. Thus, by varying the optical path is possible to obtain the interference pattern.

When the sample is incised by IR, the beam produces on the molecule vibrations and/or rotations causing a net change in the dipolar moment. In turn, the alternating IR interacts with fluctuations in the dipolar moment of the molecule. When the IR frequency matches the molecule vibrational frequency, the radiation is absorbed causing a change in the amplitude of molecular vibration [66]. Typical molecular vibrations are shown in Fig. 26.

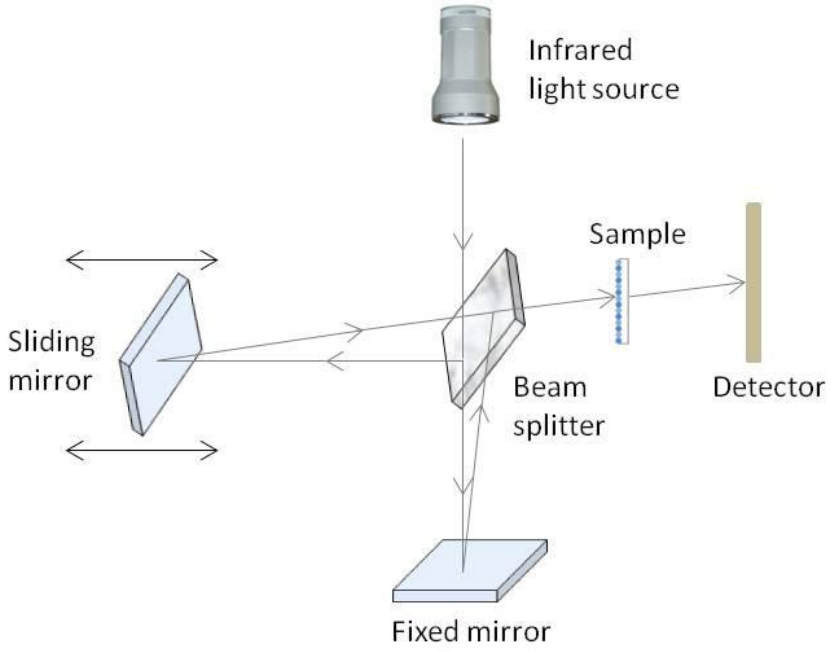

Figure 25. Schematic representation of a Michelson interferometer system.

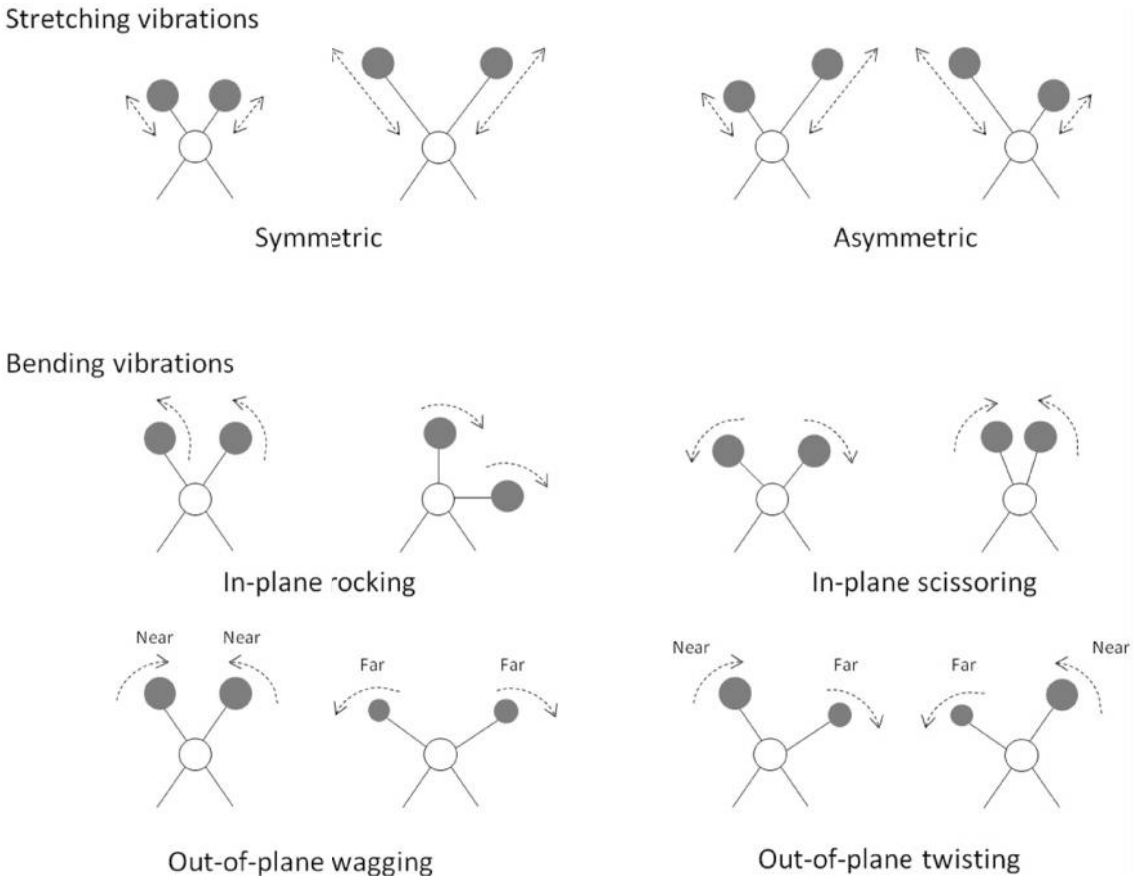

Figure 26. Main molecular vibrations induced by infrared excitation.

Two modes of FTIR were used to characterize the composites: in attenuated total reflectance (ATR-FTIR) for PSi/CD hybrids and in specular reflection (SR-FTIR) for PSi/CaP bioceramics. In the ATR mode the IR beam is passed through a crystal resulting in an evanescent wave which penetrates the sample around 0.5 μm. In the SR mode, the IR incident angle is the same of the IR reflected angle. The ATR-FTIR spectrometer (Spectrum One, Lita detector, MIR source) was facilitated by UMET, which was used in the range between 4000 and 650 cm^{-1} with a resolution of 1 cm^{-1} (NS = 4). The SR-FTIR measurements were carried out in a Brücker spectrometer mod. IFS 60v (4 cm^{-1} resolution, 7000-550 cm^{-1} range) of SIdI facilities.

x) X-ray Photoelectron Spectroscopy (XPS)

X-ray Photoelectron Spectroscopy (XPS) is a surface-sensitive technique probing at an average depth of 2−6 nm, depending on the material [67]. It is used to measure elemental composition, and electronic states of the elements that exist within a material. XPS is based on the photoelectric effect in which the interaction of an X-ray photon of sufficient energy with a solid results in the emission of an electron from its surface [63]. The fundamental energy conservation equation in photoemission is the following [67]:

$$h\nu = E_{bin}^{F} + E_{kin} + \Phi_0 \qquad \text{(Eq. 8)}$$

in which h is Planck's constant; ν is the photon frequency; E_{bin}^{F} is the binding energy relative to the Fermi level or electron potential; E_{kin} is the kinetic energy of the emitted electron; and Φ_0 is the work function of the spectrometer used to measure kinetic energy. If the electron's kinetic energy is measured, and the spectrometer work function is known, it is possible to measure the binding energies of various inner (or core) electrons, as well as those of the outer (or valence) electrons (Fig. 27).

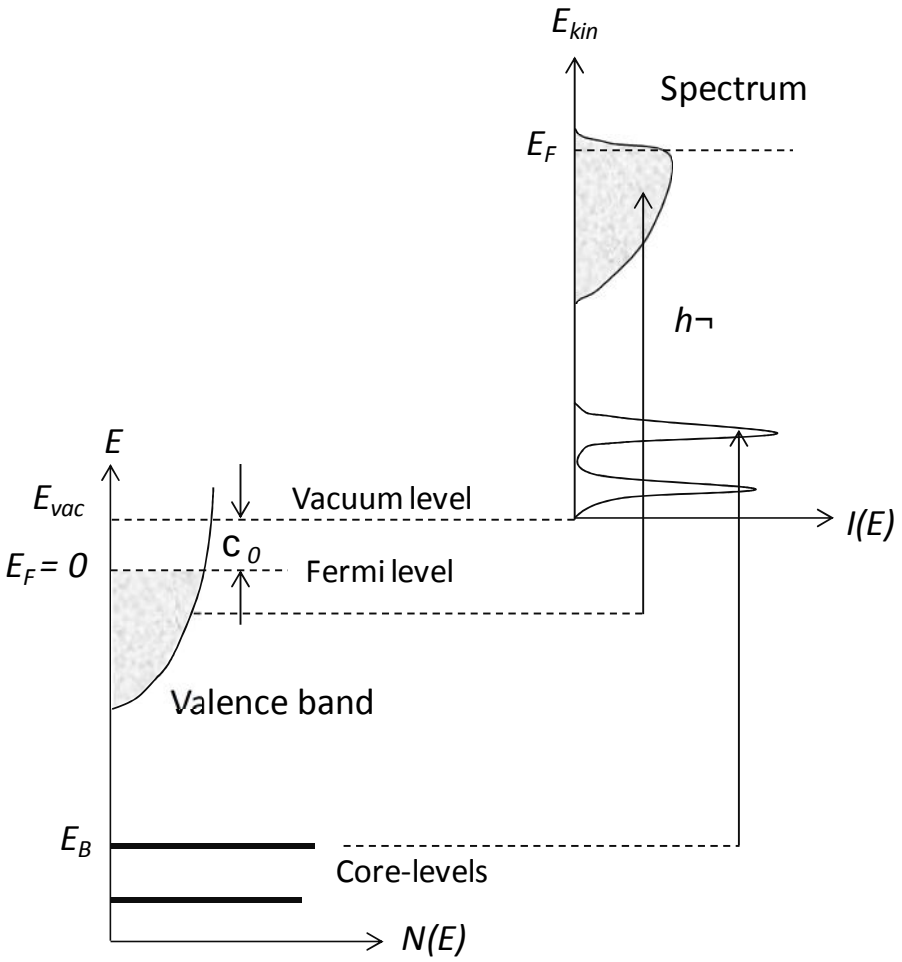

Fig. 27. Schematic view of the photoemission process in the single-particle picture. Electrons with binding energy E_B can be excited into free-electron states above the vacuum level E_{vac} by photons with energy $h\nu > E_B + \Phi_0$. The photoelectron distribution $I(E_{kin})$ can be measured by the analyser and is – in first order – an image of the occupied density of electron states $N(E_B)$ of the sample [68].

The PSi/CD hybrids were characterized in detail by XPS technique at the Institute for Health and Consumer Protection of Joint Research Centre in Ispra, Italy. Measurements have been performed with an AXIS ULTRA Spectrometer (KRATOS Analytical, UK). The samples were irradiated with monochromatic AlKα X-rays (hν=1486.6eV). The area of analysis was 400x700 μm^2 and the take-off angle (TOA) was fixed at 90° with respect to the sample surface. Pass energies of 160 eV and 20 eV were used for the survey and core level spectra, respectively. A filament (I = 1.9 A, V = 3.2 V) inserted in the magnetic lens system acts as neutralizer for surface charge compensation. All core level spectra were shifted to a common binding energy of the hydrocarbon component of the C1s spectrum at 285.0 eV. The data were processed using the Vision2 software (Kratos, UK) and CasaXPS v3.15 (Casa Software, UK).

xi) Hard X-ray Photoelectron Spectroscopy (HAXPES)

Hard X-ray photoelectron spectroscopy (HAXPES) is an emerging non destructive technique to determine the chemical and electronic properties of surfaces, buried interfaces and bulk of solid materials reaching in some cases until 25 nm at 15 keV depending on the material [69]. As typical energies involved in conventional XPS are between 40 and 2 000 eV, its analysis is limited to material surfaces. This is because of the low electron inelastic-mean-free-path (IMFP) and/or the effective attenuation length (EAL) obtained in the solid materials at that energies. However, by means of HAXPES as excitation source, high kinetic energy photoelectrons can be produced and macroscopic penetration depth in the materials can be obtained [70]. Consequently, HAXPES benefits over conventional XPS, due the exceptionally large escape depth of high kinetic energy photoelectrons enabling the study of bulk and buried interfaces up to depths of several tens of nanometres.

In HAXPES, the photoemission intensity for photoelectrons of a q-ionization-sub-shell produced from a constituent element A located between depth Z_A and Z_B of a laterally (x,y) homogeneous sample, within the analyzed area is [70]:

$$I_{Aq}(hv, E_{kin}) = Cf(E_{hv})\sigma_{Aq}(E_{hv})\Gamma(E_{kin})P_{Aq}(E_{kin},\theta)\int_{Z_A}^{Z_B} n_A(z)\,exp\left(-\frac{z}{EAL(E_{kin})cos\theta}\right)dz \qquad \text{(Eq. 9)}$$

where *C* is the ratio between the X-ray irradiated area and the analyzer area; $f(E_{hv})$ is the intensity of the incident X-rays; $\pm_{Aq}(E_{hv})$ is the photoionization cross-section; $\Gamma(E_{kin})$ is the detector transmission function which depends on the kinetic energy of the photoelectrons; *P* is the correction factor for the angular anisotropy of the photoemission process; *EAL* is the effective attenuation length of the photoelectrons; $n_A(z)$ is the density profile with depth and θ denotes the angle between the collection direction and the surface normal. The photoemission process scheme in Fig. 27 is also valid to HAXPES.

PSi/CaP bioceramics made by CEA were characterized by HAXPES. The analyses were performed at the Spanish CRG SpLine beamline (BM25) of the ESRF, Grenoble, France [70], using a sector of a cylindrical mirror analyzer (HV-CSA300) enabling working in a very broad kinetic energy range (from few eV up to 15 KeV). A

two dimensional event counting detector was used in combination with the CSA analyzer to reduce the counting rate. The analyzer was used with a constant energy resolution of 1 eV in order to enhance the analyzer transmission and to measure the photoemission spectra in few minutes. The overall instrumental energy resolution results from the convolution of the analyzer resolution with the x-ray bandwidth. A double crystal monochromator equipped with Si (1 1 1) crystals was used providing an energy resolution of $\Delta E/E = 1.5\times10^{-4}$. Photon energies from 8.5 to 15.5 keV were used to excite Ca 1s, P 1s and Si 1s signals of the samples. The HAXPES measurements were performed in a geometry in which the direction of the x-rays, the photoelectron direction towards the analyzer and the surface normal are in the x-ray polarization plane (azimuth angle set to 0º). The photon incident angle was set to 5º with respect to the sample surface. The electron emission angle was fixed to 15º, on the forward direction, from the normal to the sample surface. Hence the angle formed between the x-rays direction and the analyzer was 100º. The data were processed using the OriginPro 8 and XPS PEAK 4.1 software.

xii) Rutherford Backscattering Spectroscopy (RBS)

Rutherford Backscattering Spectroscopy (RBS) is a technique used to determine the elements present in a given sample, their stoichiometry, and their depth distribution [71]. In a RBS analysis (Fig. 28), the sample under study is bombarded with a monoenergetic beam of ions (i. e. H^+ or $^4He^+$ at ~ MeV) and backscattered particles are analized by a detector system which measures their energy [9].

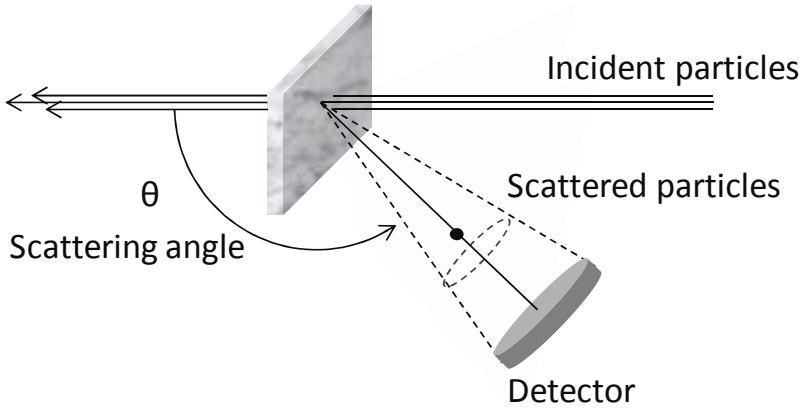

Fig. 28. Schematic representation of the experimental setup for RBS analysis.

When the incident ion collides with an atom at rest from the sample, part of the incident ion energy is transferred to the target atom receding into the material by the impact effect. The collision between particles is elastic, so, the energetic balance after collision depends on the masses of incoming and target atoms. From the equations of classical kinematics it is possible to determine the fraction of energy which retains the ion after collision [9]:

$$E_f = k^2 E_0 \qquad \text{(Eq. 10)}$$

$$k = \left[\frac{\left(m_1 cos\theta + \sqrt{m_2^2 - m_1^2 sin^2\theta} \right)}{m_1 + m_2} \right]^2 \qquad \text{(Eq. 11)}$$

where E_f is the residual energy of the particle scattered (m_1) at angle θ; k is the kinematic scattering factor, which is actually the energy ratio of the particle before and after the collision; and E_0 is the energy of the target atom (m_2).

RBS was used to quantify the Ca/P atomic ratio of PSi/CaP bioceramics made by CEA. The technique was performed using the 5 MeV terminal voltage HVEE tandetron accelerator of Centro de Microanálisis de Materiales (CMAM) [72]. The analysis was performed at oxygen resonant energies (resonant RBS) at an energy of 3.035 MeV by a $^4He^+$ ion beam. The corresponding simulations were carried out using the software SIMNRA 6.05 [73].

2.3.3 *In vitro* biological assays

The *in vitro* biological assays were carried out by means of cell culturing. A cell culture is the removal of cells from an animal or plant and their subsequent growth in an artificial environment [74]. The primary culture is the stage after cells are isolated from the tissue and proliferated under the appropriate conditions until they occupy the entire available substrate. Moreover, the subculture is the cell transferring to a new substrate with fresh growth medium for continued growth.

This technique is one of the major tools used in cellular and molecular biology for the study of:

- physiology and biochemistry of cells;
- the effects of drugs and toxic compounds on the cells;
- mutagenesis and carcinogenesis;
- drug screening and development of biological compounds.

Two kinds of cells were used to test the biocompatibility of PSi-based composites: L132 cells on PSi/CD hybrids and human mesenchymal stem cells (hMSCs) on PSi/CaP bioceramics.

i) L132 Cells

L132 cells are the human embryonic lung cell line [75] successful used to test the biocompatibility of prosthesis [76]. A cell line, or subclone, is derived from the primary culture after the first subculture [74]. As they have a limited life span and are transferred, cells with the highest growth capacity predominate, resulting in a degree of genotypic and phenotypic uniformity in the population, which are used to evaluate the biocompatibility of materials. L132 cells grown on commercial materials are show in Fig. 29.

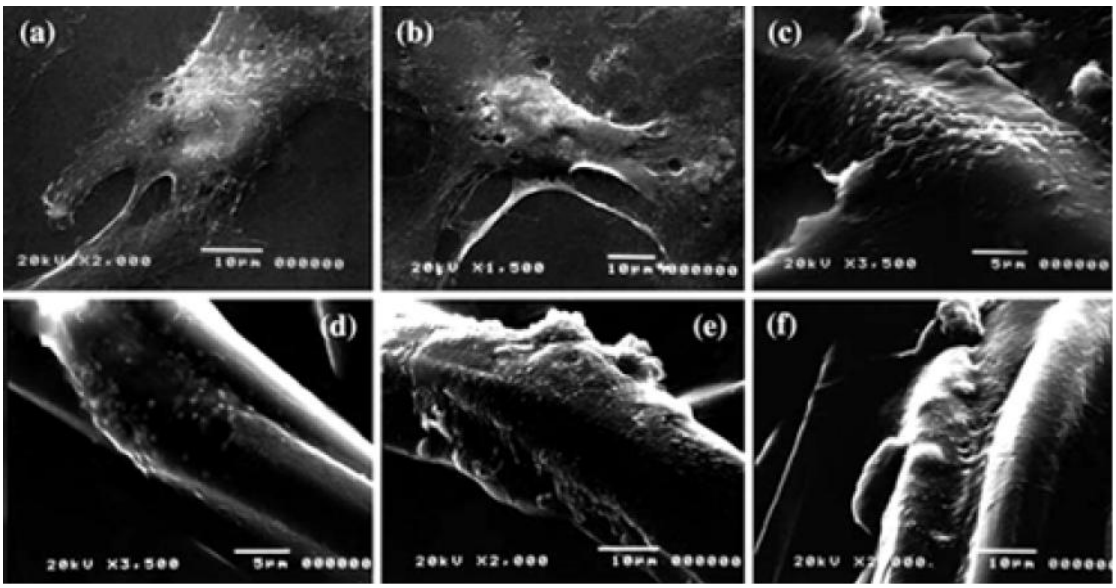

Fig. 29. SEM images of L132 cells grown on: a) control substrate; b) Melinex®; c) Polythese®; d) Polymaille®; e) Polythese® functionalized with a cyclodextrin polymer; and f) Polymaille® functionalized with a cyclodextrin polymer (from Blanchemain et al. [76]).

The cytocompatibility of the PSi/CD hybrids was evaluated by L132 cell culture according to the protocol of Groupe de Recherche sur Biomatériaux in Université Lille 2. First, cells were cultured in Eagle's minimum essential medium (MEM, ATCC®) with glutamax (Gibco BRL) supplemented with 10% fetal calf serum (FCS, Gibco); 50 µg/mL gentamicin (Gibco) and 1 µg/mL amphotericin B (Gibco). Later, cells were incubated at 37°C and 5% CO_2 atmosphere and 100% relative humidity. The cells in the phase of exponential growth were seeded on the samples and cultured for 24 h. For the observation of cell adhesion and cell morphology with SEM, the samples were fixed with 2.5% glutaraldehyde in 0.1 M sodium phosphate buffer (pH 7), then washed twice in 0.1 M sodium phosphate buffer. Thereafter, the samples were post-fixed with 1% osmium tetroxide (OsO_4) in saturated $HgCl_2$ to obtain the best cell morphology. After a graduated dehydration in ethanol, the samples were critical-point dried with CO_2 and examined in a J-SM-5300 SEM (Jeol), operated at 30 keV.

ii) Human Mesenchymal Stem Cells (hMSCs)

Human Mesenchymal Stem Cells (hMSCs) are multipotent cells present in adult marrow [77]. They can replicate as undifferentiated cells, but have the potential to differentiate to lineages of mesenchymal tissues such as bone, cartilage, fat, tendon, muscle, and marrow stroma. In general, mesenchymal stem cells can be used to study the biocompatibility and bioactivity of materials designed to orthopaedic and dental applications [78]. In Fig. 30, a hMSCs image taken by fluorescence microscopy is shown.

The biocompatibility of PSi/CaP bioceramics was tested by hMSCs culture according to Muñoz et. al. [79] in the Departamento de Biología Molecular, Universidad Autónoma de Madrid. Cells were isolated from human bone marrow samples and collected by centrifugation on 70% Percoll gradient and seeded at 200,000 cm^2 in DMEM-LG (Gibco) supplemented with 10% fetal bovine serum (FBS, Sigma). Before conducting any cell culture, phosphate buffered saline (PBS) rinsing and UV exposure were used to sterilize composite materials used in this study. Then, samples were placed on 24-multiwell plates, 15000 cells were seeded in each well and incubated with DMEM-LG supplemented with 10% FBS for 24h at 37°C for conducting hMSCs adhesion studies. For *in situ* immunofluorescence, cells were rinsed twice with PBS and fixed with 3.7%

formaldehyde in PBS during 15 min for further actin and nuclei staining. Cytoskeleton was permeated by incubating in a buffer containing 10^{-2} M Pipes pH 6.8, 3.10^{-3} M $MgCl_2$, 10^{-1} M NaCl, 10^{-3} M EGTA, 0.3 M sucrose and 0.5% triton X- 100 for 30 min at room temperature. Then, samples were washed with PBS. In order to block materials surfaces, 1% bovine serum albumin in PBS for 1 h at room temperature was used. Actin was stained by phalloidin-Alexa 488 at 1:100 *v/v* dilution (Molecular Probes) and nuclei were stained with Dapi diluted 1:5000 *v/v* (Calbiochem) in dark conditions for 45 min. Finally, cells were visualized in an inverted fluorescence microscope (Olympus IX81) coupled to a CCD colour camera.

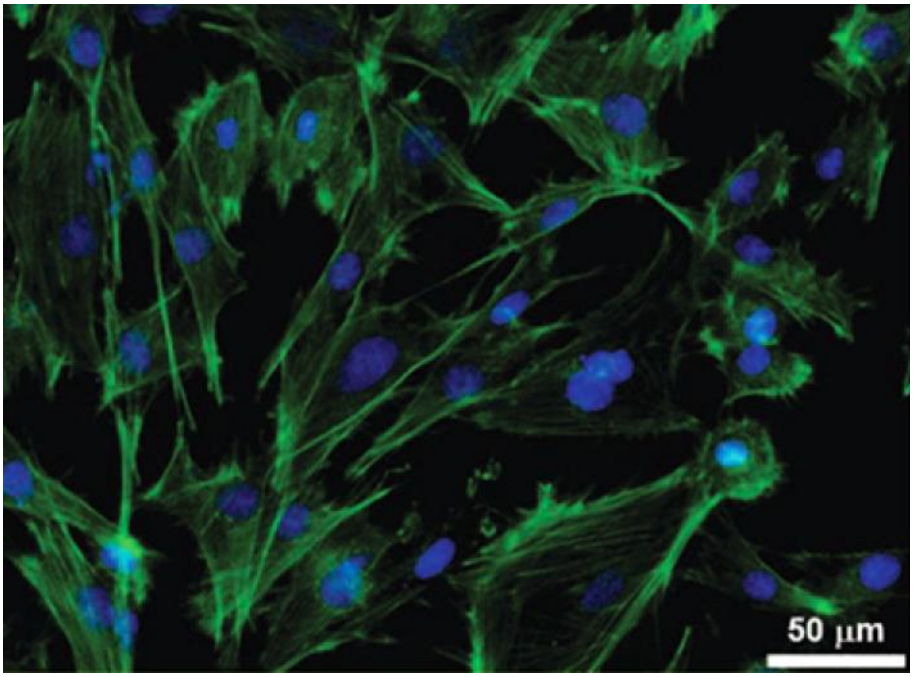

Fig. 30. Fluorphore labeled hMSCs grown on a gelatin-covered glass control (DAPI-stained nuclei, Alexa 488 phalloidin stained actin, from Muñoz et al. [79]).

2.3.4 Drug release profiles

Drug delivery systems release a drug in a controlled manner, at a predetermined rate for a definite time period [80]. A potentially usefull method to monitor the drug release kinetic is by UV-Vis spectroscopy [81] (section 2.2.2-vii), because of the absorbance is directly proportional to the concentration of the light-absorbing species in the sample:

$$A_\lambda = \varepsilon_\lambda bc \qquad \text{(Eq. 12)}$$

where A_λ is the absorbance at a wavelength; ε is the molar absorptivity at a particular wavelength; *b* is the pathlength; and *c* is the concentration of the sample. Then, the release profile can be obtained from calculated concentrations at different times (Fig. 31).

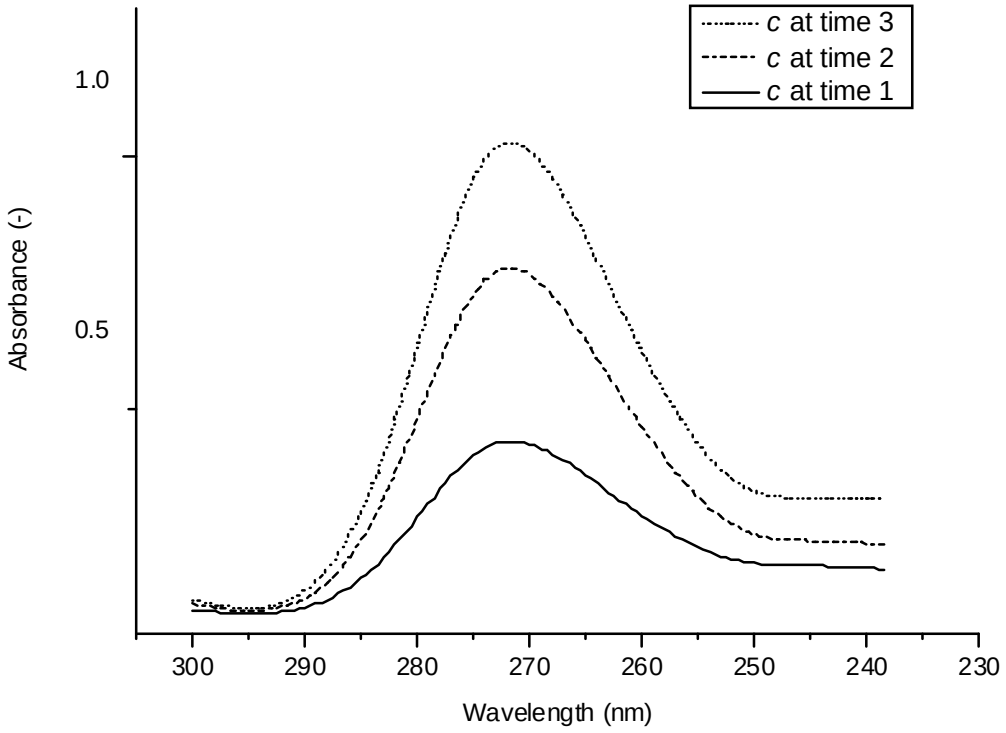

Fig. 31. Examples of absorbance spectra at different time of drug release.

The kinetic studies of PSi/CD hybrids as drug delivery systems were analyzed by drug release profiles done according to UMET protocol. Samples were loaded with ciprofloxacin-base (CFX, an antibiotic) and prednisolone (PDN, an anti-inflammatory) (both in Fig. 32), by means of a saturated aqueous solution of each drug (60 mg/L and 2 g/L, respectively) for 24 h stirring at 100 rpm. In order to check the maximum drug loading, samples were hydrolyzed by stirring for 24 h in 0.1 M NaOH solutions that were analyzed by UV–visible spectrometry [82] (UV-1800 spectrometer, Shimadzu). CFX was

detected at 275 nm and the PDN at 245 nm. Drug release data were collected at different times in two different media: distilled water and PBS, both in agitation at 100 rpm.

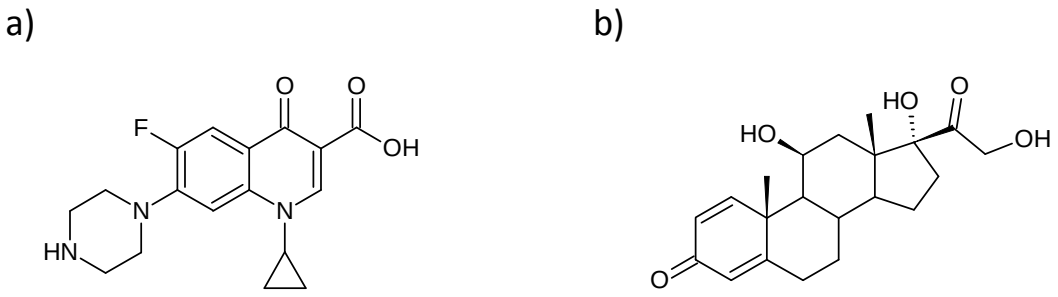

Figure 32. Scheme of: a) CFX, ciprofloxacin; and b) PDN, prednisolone.

References

[1] Bisi O, Ossicini S, Pavesi L. Porous silicon: a quantum sponge structure for silicon based optoelectronics. Surf Sci Rep 2000;38(1-3):1-126.

[2] Kolasinski KW. Silicon nanostructures from electroless electrochemical etching. Curr Opin Solid State Mater Sci 2005;9(1):73-83.

[3] Advanced Micromaching Tools. Electrochemical Etch-Stop. 2013; , 2013.

[4] Lehmann V, Gosele U. Porous silicon formation: A quantum wire effect. Appl Phys Lett 1991;58(8):856-858.

[5] Arrand HF. PhD Thesis: Optical Waveguides and Components Based on Porous Silicon. Nottinhgha, UK.: The University of Nottingham; 1997.

[6] Gerischer H. The impact of semiconductors on the concepts of electrochemistry. Electrochim Acta 1990;35(11):1677-1699.

[7] Beale M, Benjamin J, Uren M, Chew N, Cullis A. An experimental and theoretical study of the formation and microstructure of porous silicon. J Cryst Growth 1985;73(3):622-636.

[8] Uhlir A. Electrolytic shaping of germanium and silicon. Bell System Tech J 1956;35:333-347.

[9] V. Torres-Costa. Tesis doctoral: Dispositivos Interferenciales Basados en Silicio Nanoestructurado para Aplicaciones Optoelectrónicas. Madrid, Spain: Universidad Autónoma de Madrid; 2006.

[10] Gorbanyuk T, Evtukh A, Litovchenko V, Solnsev V, Pakhlov E. Porous silicon microstructure and composition characterization depending on the formation conditions. Thin Solid Films 2006;495(1):134-138.

[11] Steiner P, Lang W. Micromachining applications of porous silicon. Thin Solid Films 1995;255(1):52-58.

[12] Hamilton B. Porous silicon. Semicond Sci Technol 1999;10(9):1187.

[13] Martin-Palma RJ, Manso-Silvan M, Torres-Costa V. Biomedical applications of nanostructured porous silicon: a review. J Nanophotonics 2010;4(042502):1-20.

[14] Smith R, Collins S. Porous silicon formation mechanisms. J Appl Phys 1992;71(8):R1-R22.

[15] Saraf L, Baer DR, Wang Z, Young J, Engelhard MH, Thevuthasan S. Hydrogen bubbles and formation of nanoporous silicon during electrochemical etching. Surf Interface Anal 2005;37(6):555-561.

[16] Álvaro Muñoz-Noval. Tesis doctoral: Estructuras híbridas de silicio poroso y metal/óxido de metal: Síntesis, caracterización y aplicaciones en biomedicina. Madrid, Spain: Universidad Autónoma de Madrid; 2011.

[17] Föll H, Christophersen M, Carstensen J, Hasse G. Formation and application of porous silicon. Mat Sci Eng R 2002;39(4):93-141.

[18] Maria Arroyo-Hernandez. Tesis doctoral: Biofuncionalización de superficies de silicio monocristalino, nanoestructurado y macroporoso. Madrid, Spain: Universidad Autónoma de Madrid; 2006.

[19] Buriak JM, Stewart MP, Geders TW, Allen MJ, Choi HC, Smith J, et al. Lewis acid mediated hydrosilylation on porous silicon surfaces. J Am Chem Soc 1999;121(49):11491-11502.

[20] V. Demontis. PhD thesis: Porous Silicon applications in biotechnology. Cagliari, Italy: Università degli Studi di Cagliari; 2006.

[21] Dhanekar S, Jain S. Porous silicon biosensor: Current status. Biosensors and Bioelectronics 2013;41:54-64.

[22] Petrova-Koch V, Muschik T, Kux A, Meyer B, Koch F, Lehmann V. Rapid-thermal-oxidized porous Si-The superior photoluminescent Si. Appl Phys Lett 1992;61(8):943-945.

[23] Tolstoy VP, Chernyshova I, Skryshevsky VA. Handbook of infrared spectroscopy of ultrathin films. USA: Wiley-VCH; 2003.

[24] Mawhinney DB, Glass Jr JA, Yates Jr JT. FTIR study of the oxidation of porous silicon. J Phys Chem B 1997;101(7):1202-1206.

[25] Naveas N, Costa VT, Gallach D, Hernandez-Montelongo J, Palma RJM, Garcia-Ruiz JP, et al. Chemical stabilization of porous silicon for enhanced biofunctionalization with immunoglobulin. Sci Technol Adv Mater 2012;13(4):045009.

[26] Dhanekar S, Jain S. Porous silicon biosensor: Current status. Biosens Bioelectron 2013;41:54-64.

[27] van de Manakker F, Vermonden T, van Nostrum CF, Hennink WE. Cyclodextrin-based polymeric materials: synthesis, properties, and pharmaceutical/biomedical applications. Biomacromolecules 2009;10(12):3157-3175.

[28] Bibby DC, Davies NM, Tucker IG. Mechanisms by which cyclodextrins modify drug release from polymeric drug delivery systems. Int J Pharm 2000;197(1):1-11.

[29] Moya-Ortega MD, Alvarez-Lorenzo C, Concheiro A, Loftsson T. Cyclodextrin-based nanogels for pharmaceutical and biomedical applications. Int J Pharm 2012;428:152-163.

[30] Zhan J, Singh A, Zhang Z, Huang L, Elisseeff JH. Multifunctional aliphatic polyester nanofibers for tissue engineering. Biomatter 2012;2(4):202-212.

[31] Langer R, Tirrell DA. Designing materials for biology and medicine. Nature 2004;428(6982):487-492.

[32] Davis ME, Brewster ME. Cyclodextrin-based pharmaceutics: past, present and future. Nat Rev Drug Discov 2004;3(12):1023-1035.

[33] Buschmann H, Schollmeyer E. Applications of cyclodextrins in cosmetic products: a review. J Cosmet Sci 2002;53(3):185-192.

[34] Loftsson T, Brewster ME. Pharmaceutical applications of cyclodextrins. 1. Drug solubilization and stabilization. J Pharm Sci 1996;85(10):1017-1025.

[35] Del Valle EM. Cyclodextrins and their uses: a review. Process Biochem 2004;39(9):1033-1046.

[36] Singh M, Sharma R, Banerjee U. Biotechnological applications of cyclodextrins. Biotechnol Adv 2002;20(5):341-359.

[37] Li J. Cyclodextrin inclusion polymers forming hydrogels. Adv Polym Sci 2009;222:79-113.

[38] Asanuma H, Kakazu M, Shibata M, Hishiya T. Molecularly imprinted polymer of β-cyclodextrin for the efficient recognition of cholesterol. Chem Commun 1997(20):1971-1972.

[39] Martel B, Ruffin D, Weltrowski M, Lekchiri Y, Morcellet M. Water-soluble polymers and gels from the polycondensation between cyclodextrins and poly (carboxylic acid) s: A study of the preparation parameters. J Appl Polym Sci 2005;97(2):433-442.

[40] Dorozhkin SV. Calcium orthophosphates. J Mater Sci 2007;42(4):1061-1095.

[41] Syed-Picard FN, Jayaraman T, Lam RS, Beniash E, Sfeir C. Osteoinductivity of calcium phosphate mediated by connexin 43. Biomaterials 2013;34:3763-3774.

[42] Bose S, Tarafder S. Calcium phosphate ceramic systems in growth factor and drug delivery for bone tissue engineering: A review. Acta Biomaterialia 2012;8(4):1401-1421.

[43] Canham LT, Reeves CL, Loni A, Houlton MR, Newey JP, Simons AJ, et al. Calcium phosphate nucleation on porous silicon: factors influencing kinetics in acellular simulated body fluids. Thin Solid Films 1997;297(1-2):304-307.

[44] Shaoqiang C, Ziqiang Z, Jianzhong Z, Jian Z, Yanling S, Ke Y, et al. Hydroxyapatite coating on porous silicon substrate obtained by precipitation process. Appl Surf Sci 2004;230(1-4):418-424.

[45] Heimann RB, Wirth R. Formation and transformation of amorphous calcium phosphates on titanium alloy surfaces during atmospheric plasma spraying and their subsequent in vitro performance. Biomaterials 2006;27(6):823-831.

[46] Yang Y, Kim K, Ong JL. A review on calcium phosphate coatings produced using a sputtering process—an alternative to plasma spraying. Biomaterials 2005;26(3):327-337.

[47] Cleries L, Martınez E, Fernandez-Pradas J, Sardin G, Esteve J, Morenza J. Mechanical properties of calcium phosphate coatings deposited by laser ablation. Biomaterials 2000;21(9):967-971.

[48] Ballesteros P, Yesid D, Estupinan Duran HA, Cordoba Tutta EM. Chitosan/calcium phosphate coating obtained by electrodeposition on titanium alloy. Rev fac ing univ Antioquia 2010(54):15-23.

[49] Anderson SHC, Elliott H, Wallis DJ, Canham LT, Powell JJ. Dissolution of different forms of partially porous silicon wafers under simulated physiological conditions. Phys Stat Sol (a) 2003;197(2):331-335.

[50] Krebs FC. Fabrication and processing of polymer solar cells: a review of printing and coating techniques. Solar Energy Mater Solar Cells 2009;93(4):394-412.

[51] Paunovic M, Schlesinger M. Fundamentals of Electrochemical Deposition. Second edition ed. Hoboken, New Jersey: Jhon Wiley & Sons, Inc.; 2006.

[52] Rao CR, Trivedi D. Chemical and electrochemical depositions of platinum group metals and their applications. Coord Chem Rev 2005;249(5):613-631.

[53] Meyer E. Atomic force microscopy. Prog Surf Sci 1992;41(1):3-49.

[54] Miguel Manso-Silván. PhD thesis: HAP/TiO_2 and HAP/TiN structures; surface modifications for enhanced biocompatibiity. Madrid, Spain: Universidad Autónoma de Madrid; 2001.

[55] Robinson P, Sturgis J, Kumar G. Chapter 10: Immunofluorescence. In: Kumar G, Rudbeck L, editors. Immunohistochemistry Staining Methods. 2009th ed. Carpinteria, California, USA.: Dako North America; 2006. p. 61.

[56] Bockris J, Khan S. Surface Electrochemistry: A molecular level approach. 1993rd ed. Unitaed States of America: Plenum Press, New York; 1993.

[57] Öner D, McCarthy TJ. Ultrahydrophobic surfaces. Effects of topography length scales on wettability. Langmuir 2000;16(20):7777-7782.

[58] Giovambattista N, Debenedetti PG, Rossky PJ. Effect of surface polarity on water contact angle and interfacial hydration structure. J Phys Chem B 2007;111(32):9581-9587.

[59] Tiraferri A, Elimelech M. Direct quantification of negatively charged functional groups on membrane surfaces. J Membr Sci 2012;389:499-508.

[60] Degoutin S, Jimenez M, Casetta M, Bellayer S, Chai F, Blanchemain N, et al. Anticoagulant and antimicrobial finishing of non-woven polypropylene textiles. Biomed Mater 2012;7(3):035001.

[61] Brown ME. Introduction to thermal analysis: techniques and applications. USA: Springer; 2001.

[62] Coats A, Redfern J. Thermogravimetric analysis. A review. Analyst 1963;88(1053):906-924.

[63] Elena Cerro-Prada. PhD thesis: New trends in cement systems: Interface with TiN thin films and modification with titania nanoparticles. Madrid, Spain: Universidad Autónoma de Madrid; 2013.

[64] Fewster PF. X-ray diffraction from low-dimensional structures. Semicond Sci Technol 1993;8(11):1915-1934.

[65] Harris DC. Quantitative Chemical Analysis. Third Edition ed. New York, USA: W. H. Freeman and Company; 1991.

[66] Conley RT. Espectroscopía infrarroja. 1979th ed. Spain: Editorial Alhambra, S. A.; 1972.

[67] Fadley CS. X-ray photoelectron spectroscopy: From origins to future directions. Nucl Instr Meth Phys Res A 2009;601(1):8-31.

[68] Reinert F, Hüfner S. Photoemission Spectroscopy with Very High Energy Resolution: Studying the Influence of Electronic Correlations on the Millielectronvolt Scale. In: Hüfner S, editor. Very High Resolution Photoelectron Spectroscopy. 2007th ed. Heidelberg, Germany: Springer; 2007. p. 13-53.

[69] Rubio-Zuazo J, Castro G. Hard X-ray photoelectron spectroscopy (HAXPES)(15keV) at SpLine, the Spanish CRG beamline at the ESRF. Nucl Instr Meth Phys Res A 2005;547(1):64-72.

[70] Rubio-Zuazo J, Ferrer P, Castro G. Non-destructive compositional depth profile in the tens-of-nanometer scale. J Electron Spectrosc Relat Phenom 2010;180(1):27-33.

[71] Barradas N, Jeynes C, Webb R. Simulated annealing analysis of Rutherford backscattering data. Appl Phys Lett 1997;71(2):291-293.

[72] Climent-Font A, Pászti F, Garcıa G, Fernández-Jiménez M, Agulló F. First measurements with the Madrid 5 MV tandem accelerator. Nucl Instr Meth Phys Res B 2004;219:400-404.

[73] Lao J, Nedelec JM, Moretto P, Jallot E. Micro-PIXE characterization of interactions between a sol-gel derived bioactive glass and biological fluids. Nucl Instrum Meth B 2006;245(2):511-518.

[74] Gibco®, Invitrogen®. Handbook of Cell Culture Basics. USA, Japon & UK: Life Technologies TM; 2013.

[75] Kasper M, Roehlecke C, Witt M, Fehrenbach H, Hofer A, Miyata T, et al. Induction of apoptosis by glyoxal in human embryonic lung epithelial cell line L132. Am J Respir Cell Mol Biol 2000 Oct;23(4):485-491.

[76] Blanchemain N, Chai F, Haulon S, Krump-Konvalinkova V, Traisnel M, Morcellet M, et al. Biological behaviour of an endothelial cell line (HPMEC) on vascular prostheses grafted with hydroxypropylgamma-cyclodextrine (HPγ-CD) and hydroxypropylbeta-cyclodextrine (HPβ-CD). J Mater Sci Mater Med 2008;19(6):2515-2523.

[77] Pittenger MF, Mackay AM, Beck SC, Jaiswal RK, Douglas R, Mosca JD, et al. Multilineage potential of adult human mesenchymal stem cells. Science 1999;284(5411):143-147.

[78] Chen F, Lam W, Lin C, Qiu G, Wu Z, Luk K, et al. Biocompatibility of electrophoretical deposition of nanostructured hydroxyapatite coating on roughen titanium surface: In vitro evaluation using mesenchymal stem cells. J Biomed Mater Res B 2007;82(1):183-191.

[79] Muñoz A, Sánchez V, Punzón E, Torres V, Gallach D, González L, et al. Aging of porous silicon in physiological conditions: cell adhesion modes on scaled 1D micropatterns. J Biomed Mater Res A 2012;100(6):1615-1622.

[80] Langer R. New methods of drug delivery. Science 1990;249(4976):1527-1533.

[81] Washington C. Drug release from microdisperse systems: a critical review. Int J Pharm 1990;58(1):1-12.

[82] Leprêtre S, Chai F, Hornez JC, Vermet G, Neut C, Descamps M, et al. Prolonged local antibiotics delivery from hydroxyapatite functionalised with cyclodextrin polymers. Biomaterials 2009;30(30):6086-6093.

Chapter 3:

PSi/Cyclodextrin Drug Delivery Hybrids

3.1 Introduction

The harmful side effects of pharmaceuticals within the body continuously calls for the development of new carriers and devices for drug delivery ideally allowing a sustained and localized release [1]. In particular, the delivery of drugs to the posterior eye is still a challenge, owing to anatomical and physiological constrains of the eye. Thus, various controlled drug delivery systems, such as biodegradable and non-biodegradable implants, liposomes and nanoparticles, have been developed as new therapeutic techniques for diseases of the posterior segment of the eye [2]. The routes to deliver pharmaceuticals can be topical, systemic, intravitreal and periocular [2].

The cyclodextrins (CDs) have been used as efficient delivery carriers due to their characteristic cavity and their ability to form reversible complexes with drugs [3]. Using citric acid as crosslinking of CDs it is possible to synthesize a three-dimensional polymer network suitable for drug delivery applications, prolonging the residence time in the medium and/or increasing efficiency and specificity towards targeted sites [4]. Besides, in order to improve control over drug release kinetics and stability in aqueous media, CD-based polymers could be combined with PSi as a composite [5]. After a stabilization treatment of the surface by H_2O_2 oxidation, PSi could be suitable biomaterial to use as a substrate for CD-based polymer for drug delivery applications.

In this context, PSi/CD drug delivery hybrids have been developed for the treatment of postoperative endophthalmitis (POE). POE is the severe inflammation involving both the anterior and posterior segments of the eye derived from an infectious agent after an eye surgery [6]. This complication may arise from any surgical procedure that disrupts the integrity of the globe including cataract surgeries, radial keratotomy,

retinal surgeries, and glaucoma filtering surgeries [6]. POE may be originated by the characteristic ocular inflammation after an eye surgery [7] or by a postoperative bacterial infection [8]. POE may cause postoperative pain and photophobia, but its complications may result in increased intraocular pressure, posterior capsular opacification, cystoids macular edema, and decreased visual acuity [7]. The proposed hybrids could be intravitreally injected during any eye surgery in order to reduce POE complications (Fig. 1). Other common intravitreal systems of drug release are vitreous humour and scleral implants, which are also schematized in Fig 1.

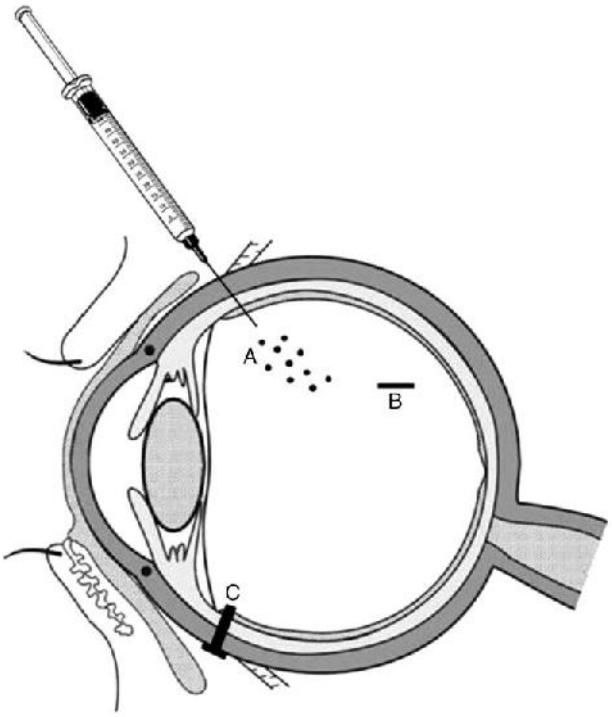

Figure 1. Scheme of the intravitreal route of drug administration to the posterior eye: A) micro- or nanoparticles injected using a needle, B) biodegradable or non-biodegradable implants surgically introduced into the vitreous humour and, C) scleral plugs or implants sutured onto the sclera (from Thrimawithana et. al. [2]).

The hybrids proposed in this chapter consist of the functionalization of nanoporous or macroporous PSi (nPSi or mPSi, respectively) by β-cyclodextrin–citric acid *in-situ* polymerization. Samples are chemically, morphologically and biologically studied by means of different techniques, and their functionalization degree is assessed. Finally, in order to test them as potential intraocular drug delivery systems [9], hybids are

loaded with two drugs used in post-ophthalmic surgery (Fig. 2): ciprofloxacin (CFX, an antibiotic) [10,11] and prednisolone (PDN, an anti-inflammatory) [12,13].

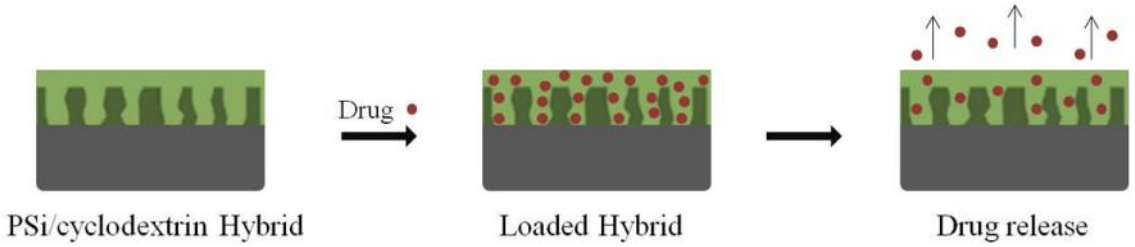

Figure 2. Scheme of PSi/cyclodextrin hybrids as drug delivery systems.

3.2 Materials and Methods

3.2.1 Synthesis of PSi/cyclodextrin hybrids

nPSi or mPSi were used as substrates for the fabrication of the hybrids. nPSi was synthesized using a current density of 60 mA/cm^2 for 90 s (Section 2.2.1 –ii of Chapter 2). A 60% porosity was calculated by gravimetric analysis. mPSi was fabricated with a current density of 20 mA/cm^2 for 600 s (Section 2.2.1 –iv of Chapter 2). The porosity calculated for mPSi was 40%. Both substrates were chemically oxidized with H_2O_2 (nPSi-COx and mPSi-Cox), rinsed with EtOH and dried under a nitrogen stream. nPSi-COx and mPSi-COx were functionalized by β-cyclodextrin–citric acid polymer (polyCD) according to the protocol described in Section 2.2.2 –iii of Chapter 2.

3.2.2 Characterization techniques

Synthesized hybrids were characterized by chemical techniques (ATR-FTIR, XPS and water contact angle) and microscopies (AFM and SEM/FESEM). Their degree of functionalization was tested by TGA and TBO titration (see Sections 2.3.1 and 2.3.2 of Chapter 2). The biocompatibility of the hybrids was tested by *in vitro* culture of the human epithelial cell line (L132). Finally, both systems were tested as drug delivery platforms with the drugs, CFX and PDN, in two media: pure water and phosphate buffer saline (PBS) solution.

3.3 Results and Discussion

3.3.1 Chemical characterization of PSi functionalization by polyCD

In this section we focus on the characterization of the chemical composition of fresh (recently synthesized PSi), oxidized (stabilized PSi), and functionalized samples (PSi hybrids) based on both nPSi and mPSi.

ATR-FTIR spectra are shown in Fig. 3. Spectra plotted in Fig. 3a correspond to nano- series. The spectrum of nPSi shows absorbance peaks at 2141, 2115, and 2090 cm^{-1}, which are attributed to Si-H_x (x=1, 2, 3) stretching modes, respectively [14]. The peak assigned to SiH_2 scissor mode was also detected at 906 cm^{-1} [15]. As it was mentioned in Section 2.1.1–vi of Chapter 2, Si-H bonds are characteristic of fresh PSi. After chemical treatment (nPSi-COx), the peaks corresponding to Si-H bonds transformed to peaks assigned to surface -O_ySi-$H_{x,}$ due to oxidation process at 2250 cm^{-1} for stretching mode and at 880 cm^{-1} for bending mode [14,15]. Besides, a weak band at 835–795 cm^{-1} from the Si–OH bond can be observed [16] as well as the O-H stretching band from SiOH groups at 3350 cm^{-1} [15]. Absorbance peaks related to surface Si-O-Si stretching mode at 1170 and 1060 cm^{-1} are also observed [14,15]. These results are in agreement with the transformations proposed in Eq. 2 of Section 2.1.1-vi in Chapter 2.

Nanoporous samples functionalized with polyCD (nPSi-CD) exhibit the same peaks as pure polyCD. The main absorbance peaks corresponding to bond vibrations from polyCD [17,18] can be observed: O-H stretching from hydroxyl and carboxyl groups (3435 cm^{-1}), CH_2 asymmetric stretching (2933 cm^{-1}), C=O stretching (1736 cm^{-1}), C-O-C stretching (1155 cm^{-1}) and the C-OH stretching (1026 cm^{-1}). This indicates that nPSi presented a properly adhered polymerized film.

Spectra of macroporous samples are plotted in Fig. 3b. In the spectrum corresponding to mPSi a weak band related to Si-H bonds from fresh PSi [19] is appreciable at 2100 cm^{-1}. In this case, the band can be decomposed into three components near 2140, 2110 and 2080 cm^{-1} [19]. Nevertheless, the main absorption peaks correspond to Si-O-Si at 1108 cm^{-1} and 870 cm^{-1} [14,20], confirming that mPSi is more susceptible to oxidation than to hydrogenation during its formation [19,21]. After chemical oxidation, the Si-H signal faded away, but SiOH groups were not detected. As in the case of nPSi-CD, mPSi-CD was also well coated with an organic film since the corresponding spectrum matches the well that of pure polyCD.

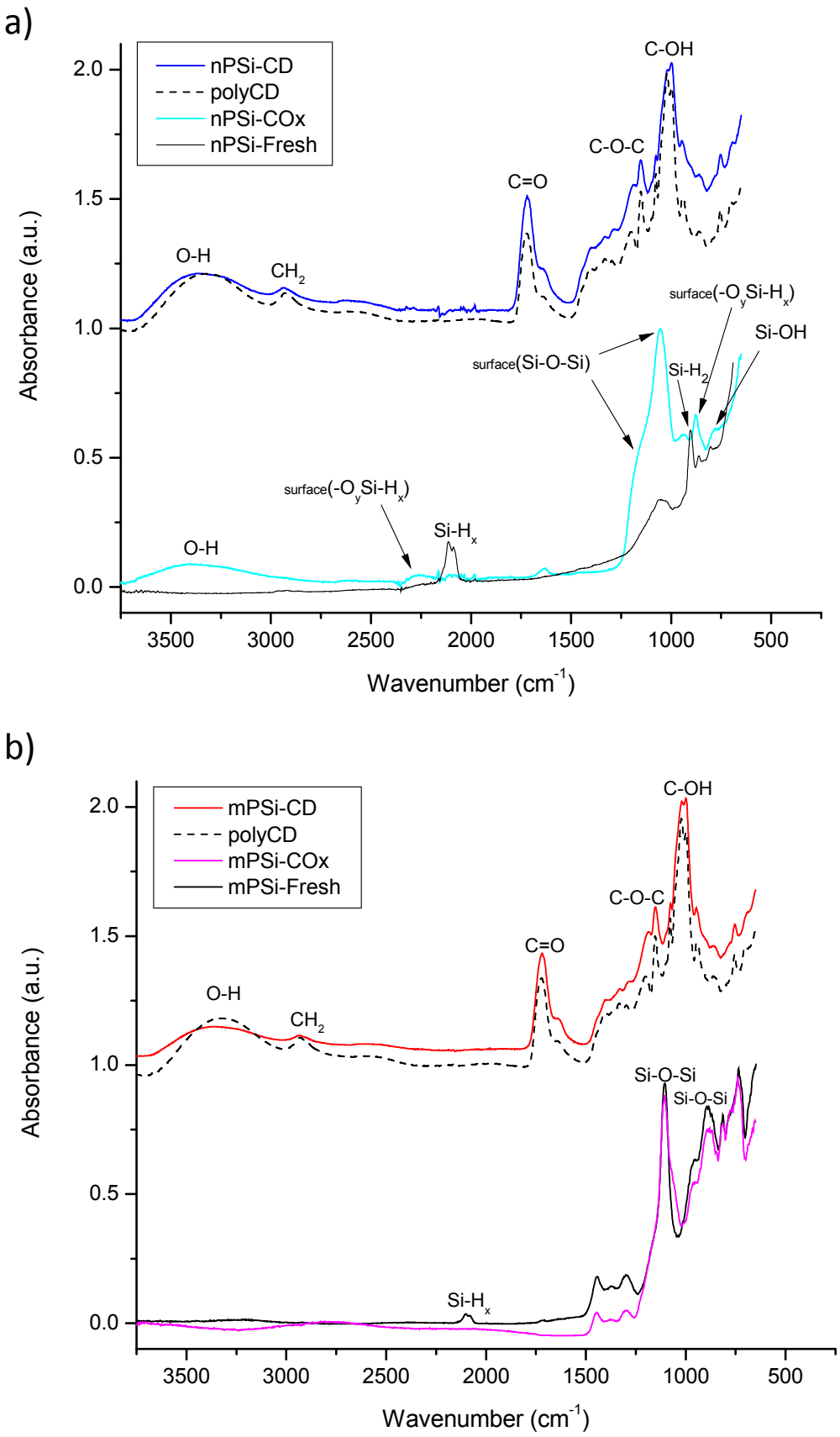

Figure 3. FTIR-ATR spectra of: a) nPSi- series samples: nPSi-Fresh (black line), nPSi-COx (cyan line), polyCD (black dotted line), nPSi-CD (blue line); and b) mPSi- series samples: mPSi-Fresh (black line), mPSi-COx (magneta line), polyCD (black dotted line), mPSi-CD (red line).

Since the XPS probing depth in our experimental conditions is approximately 10-12 nm, the study of the evolution of the surface chemistry was performed on the nPSi series samples (the corresponding surfaces are less rough than the mPSi ones, the root mean square roughness (R_{RMS}) being 1-10 nm, in the order of the scape depth of generated photoelectrons). The elemental surface composition of nPSi, nPSi-COx and nPSi-CD was obtained from the XPS survey spectra and are presented in Table 1.

Table 1. Surface chemical compositions of nPSi, nPSi-COx and nPSi-CD obtained from XPS analysis.

Sample	**C (at%)**	**O (at%)**	**N (at%)**	**Si (at%)**	**F (at%)**
nPSi	22.5 (±0.2)	31.6 (±0.03)	--	44.9 (±0.41)	1.0 (±0.2)
nPSi-COx.	2.5 (±0.4)	66.2 (±0.24)	--	30.7 (±0.5)	0.6 (±0.1)
nPSi-CD	56.9 (±0.5)	43.0 (±0.24)	--	--	--

It can be seen that the starting nPSi substrate shows C contamination, apart from the expected Si and O signals. Moreover, a light presence of other surface synthesis residues, such as F, is also detected. After oxidation, carbon is drastically reduced, whilst O content increased by a factor of 2.1**.** This indicates the successful oxidation of the PSi surface. This result is also confirmed by the analysis of the Si 2p core level spectra (Fig. 4a), where it can be noticed that the doublet at about 99.6 eV ($Si2p_{3/2}$), corresponding to the Si^0 oxidation state, strongly decreases. In parallel, the other components at higher binding energies, corresponding to different oxidation states, increase. In particular, for bare nPSi, three components related to SiO (100.7 eV), SiO_X (x<2, 102 eV) and SiO_2 (103.6 eV) are identified after deconvolution [22]. After oxidation, the major component of nPSi-COx is related to the SiO_2 groups, which accounts for about 40% of the Si signal (Fig. 4b). Moreover, the position of the SiO_2 peak shifts towards higher binding energies (0.6 eV with respect to the bare nPSi), indicating the growth of a dense oxide layer [23]. However, it should be also noticed that the intensities of the components corresponding to lower Si oxidation states and to sub-stoichiometric SiO_x bonds also increase after the oxidation process.

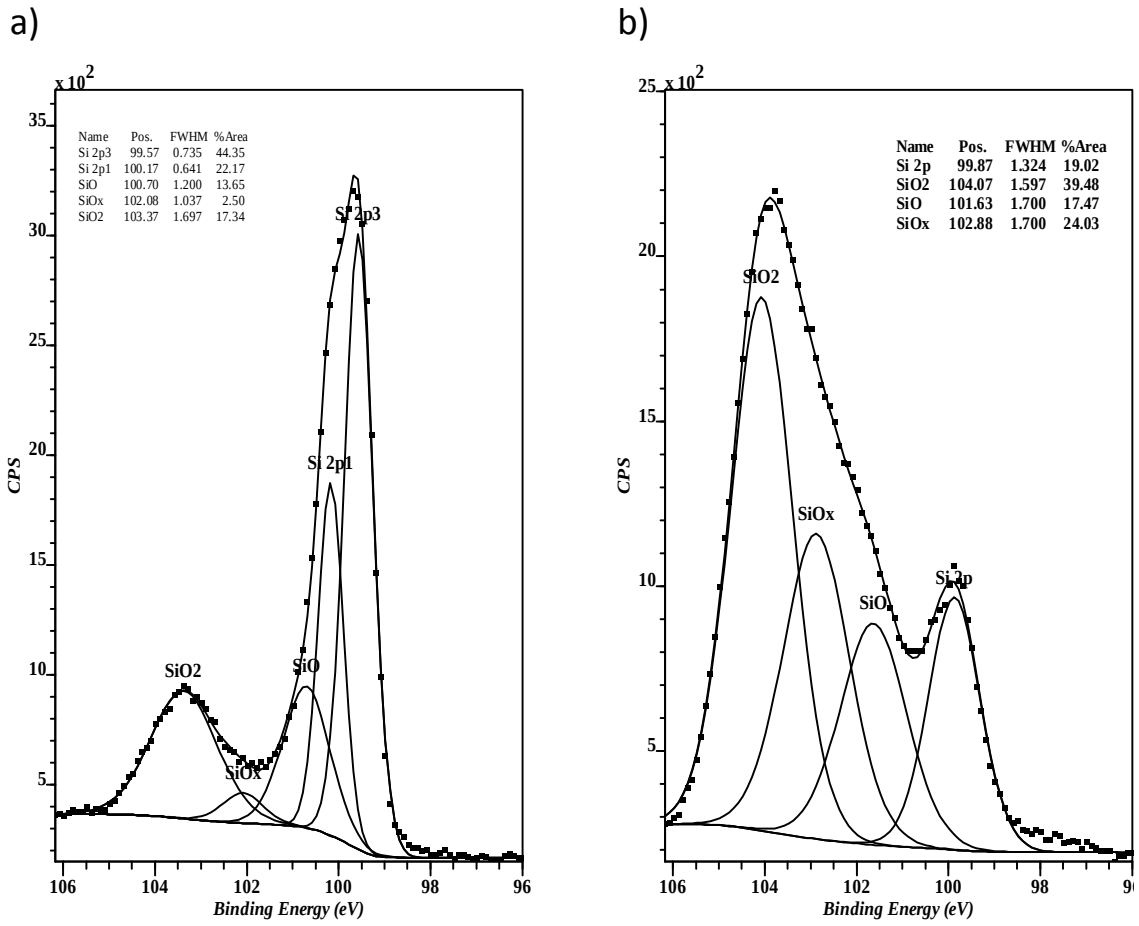

Figure 4. Si 2p core level XPS spectra of: a) nPSi and b) nPSi-COx.

The *in situ* polymerization of βCD and citric acid further changes the surface composition (Table 1). In fact the Si signal disappears, the O decreases and the carbon content increases up to 63 at%. This indicates the successful growth of a uniform and continuous polymer layer. This result is also corroborated by the C 1s core level spectrum presented in Fig. 5. The C1s envelope can be fitted with four components corresponding to C-C/CH (285.00 eV), C-O (286.5eV), C=O/O-C-O (287.5eV) and COOH/R (289.2eV) [23,24]. The success of this polymerization was supported by the previous oxidation process, which stabilizes the PSi and makes compatible the interaction with the polymerized CD`s.

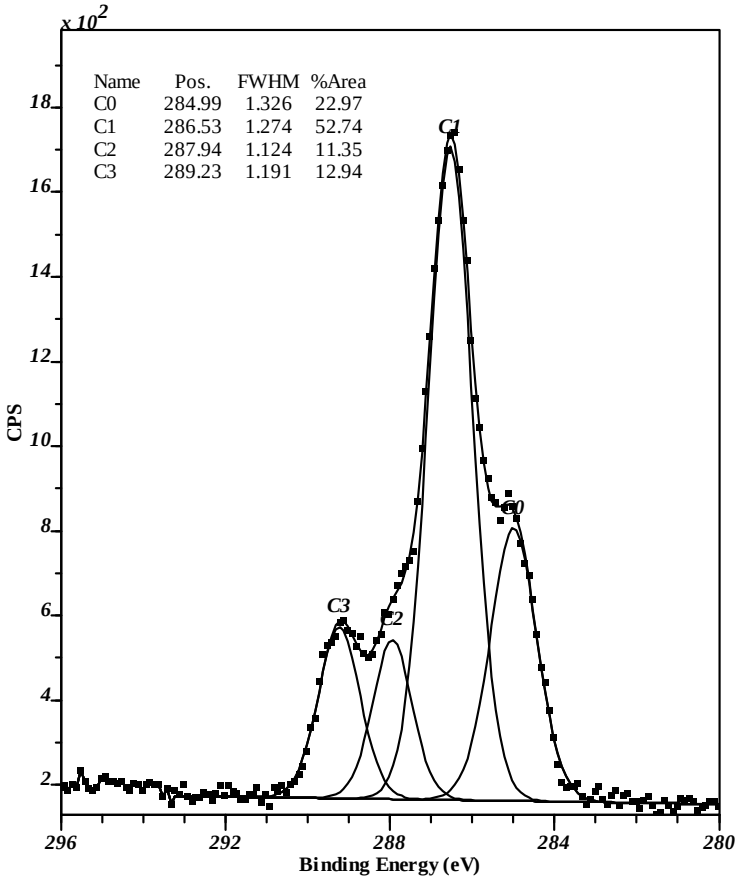

Figure 5. C1s core level spectra of nPSi-CD.

The samples surface wettability was assessed by the water contact angle technique (Fig. 6). nPSi showed a hydrophobic behavior and mPSi presented a tendency to hydrophobic behavior (water contact angle of 126° and 84º, respectively) due to Si-H surface groups [25]. After chemical oxidation, fresh samples change their wettability into a strong hydrophilic behavior, 7.7° for nPSi-COx and 14.7° for mPSi-COx, due to Si-O, H-Si-O [25] and Si-OH bonds [26]. In the case of functionalized samples, the wettability was practically the same on both (nPSi-CD and mPSi-CD) since the polymer layer has the same surface composition (Fig. 3). Their contact angles are similar: 31° for nPSi-CD and 33° for mPSi-CD. This tendency of modification is illustrated with images and data in Fig. 6-a and Fig. 6-b, respectively.

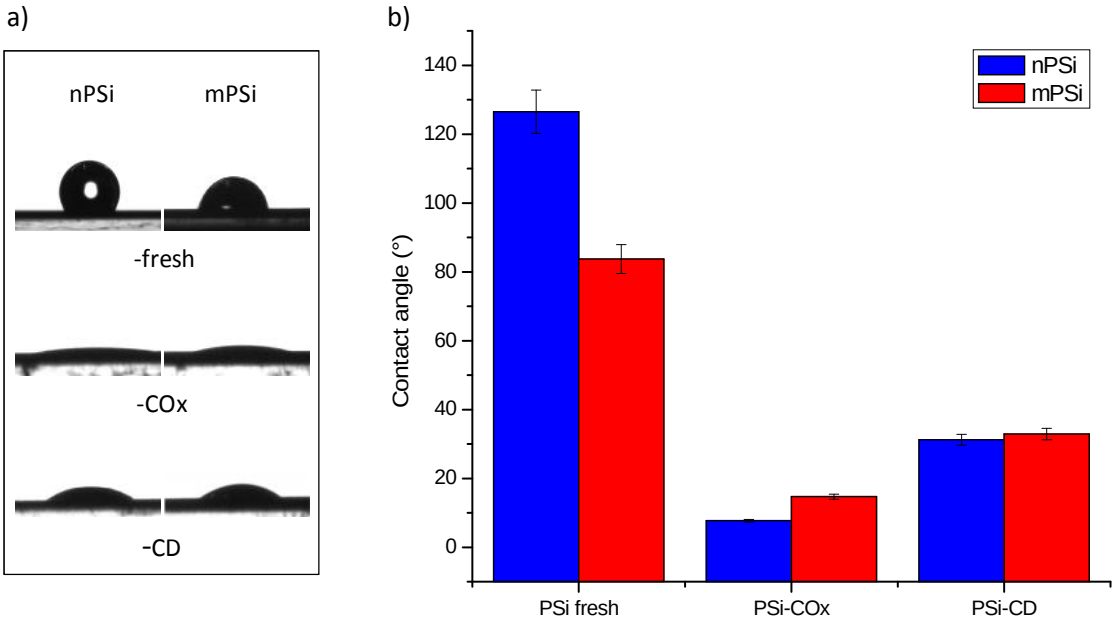

Figure 6. Contact angle technique: a) photographic sequence and b) plotted data.

3.3.2 Microscopic characterization of PSi functionalization by polyCD

In order to study the roughness and topography of the sample surface, AFM analyses were carried out, while the samples morphology was observed by SEM/FESEM.

AFM images provide relevant information regarding sample surface (Fig. 7). The analyzed area in all cases was 4 μm^2. nPSi and nPSi-COx samples (Fig. 7-a1 and 7-a2) showed a different R_{RMS}: 0.584 nm and 1.050 nm, respectively. This is reflected in the textured morphology of nPSi-COx surface that is rounder than in nPSi, which may be attributed to the oxidation post-treatment. In the case of mPSi and mPSi-COx (Fig. 7-b1 and 7-b2) both showed similar values of R_{RMS}: 0.218 μm and 0.251 μm, respectively. Therefore, they did not show a drastic morphologic change after chemical oxidation.

AFM images of functionalized samples with the polyCD are shown in Fig. 7-a3 (nPSi-CD) and Fig. 7-b3 (mPSi-CD). One can appreciate that the surface of both types of samples were completely covered by the polymer providing a different topography. They have similar values of R_{RMS}: 1.89 nm for nPSi-CD and 3.27 nm for mPSi-CD.

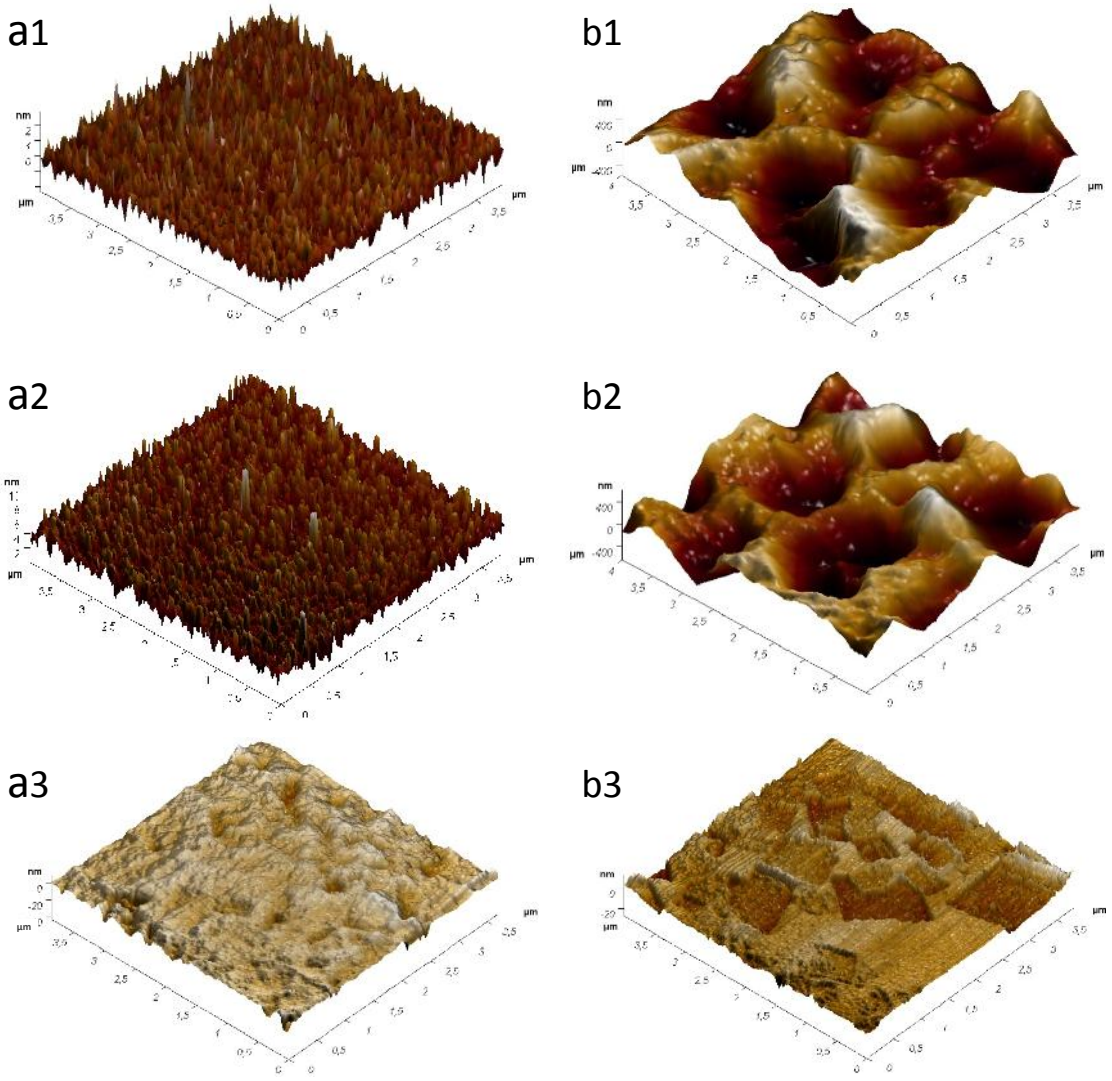

Figure 7. 3D AFM images of a1) nPSi, b1) mPSi, a2) nPSi-COx, b2) mPSi-COx, a3) nPSi-CD and b3) mPSi-CD.

The Z-profile of samples has been plotted as a complementary visualization of topographic differences among them (Fig 8). The increase in roughness of nanostructured fresh samples (nPSi) after the oxidization treatment (nPSi-COx) is clearly and better observed in Fig. 8-a than their respective 3D AFM images (Fig. 7-a1 and 7-a2, respectively): nPSi-COx show deeper valleys than nPSi. On the other hand, the close values of surface roughness of macroporous samples (mPSi and mPSi-COx) and functionalized samples (nPSi-CD and mPSi-CD) are also proved with their respective Z-profiles, because they have a similar valley depth (Fig. 8-c).

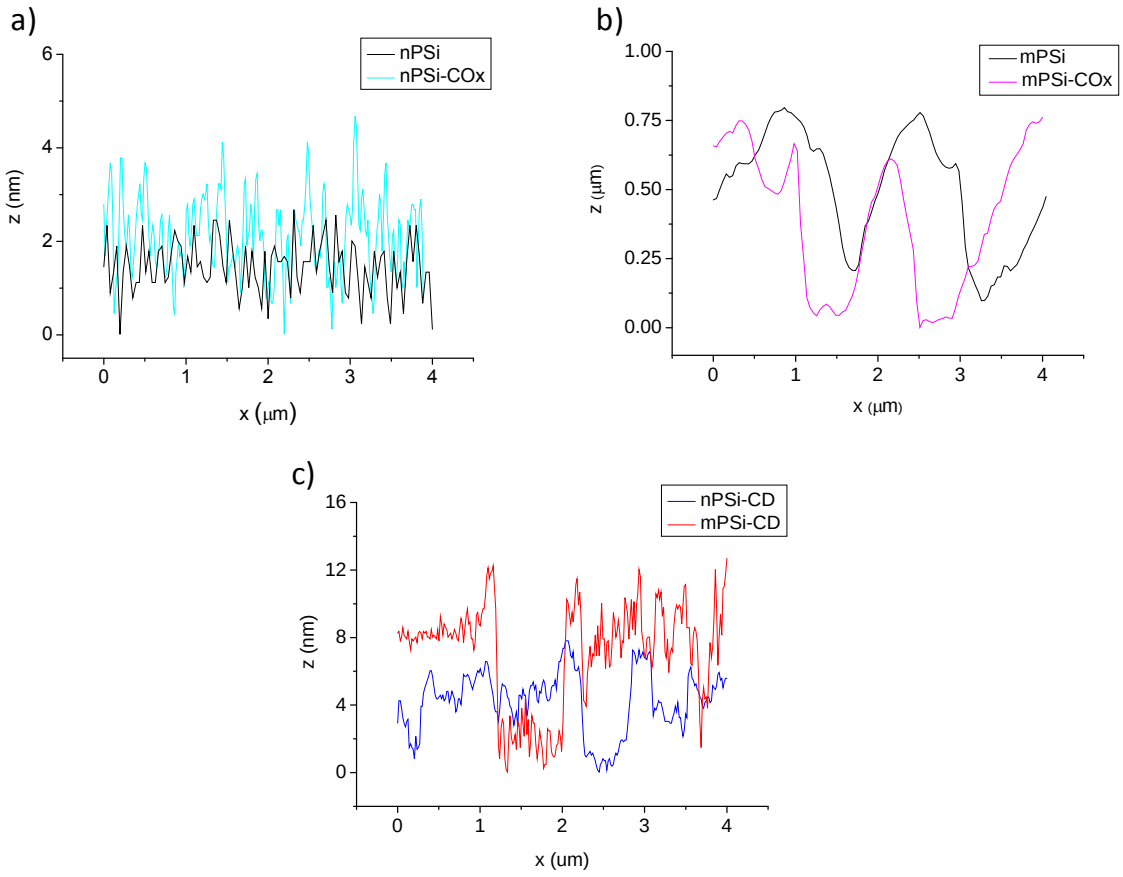

Figure 8. Comparative Z-profile of samples: a) nPSi vs nPSi-COx, b) mPSi vs-mPSi-COX, and c) nPSi-CD vs mPSi-CD.

In order to complement the study on the morphology of synthesized samples, SEM/FESEM analyses were carried out. No significant morphological differences between non-oxidized samples and oxidized samples were detected. The FESEM images of oxidized samples, nPSi-COx and mPSi-COx, are shown in Fig. 9. One can observe that nPSi-COx layer has a thickness of 3.4 μm and an average pore diameter of 30 nm (Fig. 9-a1 and Fig. 9-a2, respectively). In the case of mPSi-COx, the thickness is 7.1 μm and the pore diameter around 1 μm (Fig. 9-b1 and Fig. 9-b2, respectively).

SEM images of functionalized samples are shown in Fig 10. The synthesized polymer layer on the top surface of both samples has the same thickness (approximately 2.5 μm) and it also infiltrates into the porous matrix of samples (Fig. 10-a1 for nPSi-CD and Fig. 10-b1 for mPSi-CD). The top view of nPSi-CD and mPSi-CD (Fig. 10-a2 and Fig 10-b2, respectively) illustrate that the polymer coating is homogeneous and very similar in both cases, showing some cracks on their surface. On the other hand, cross-sectional SEM images (Fig. 11) show that both polymerizations are homogeneously well formed over the substrates.

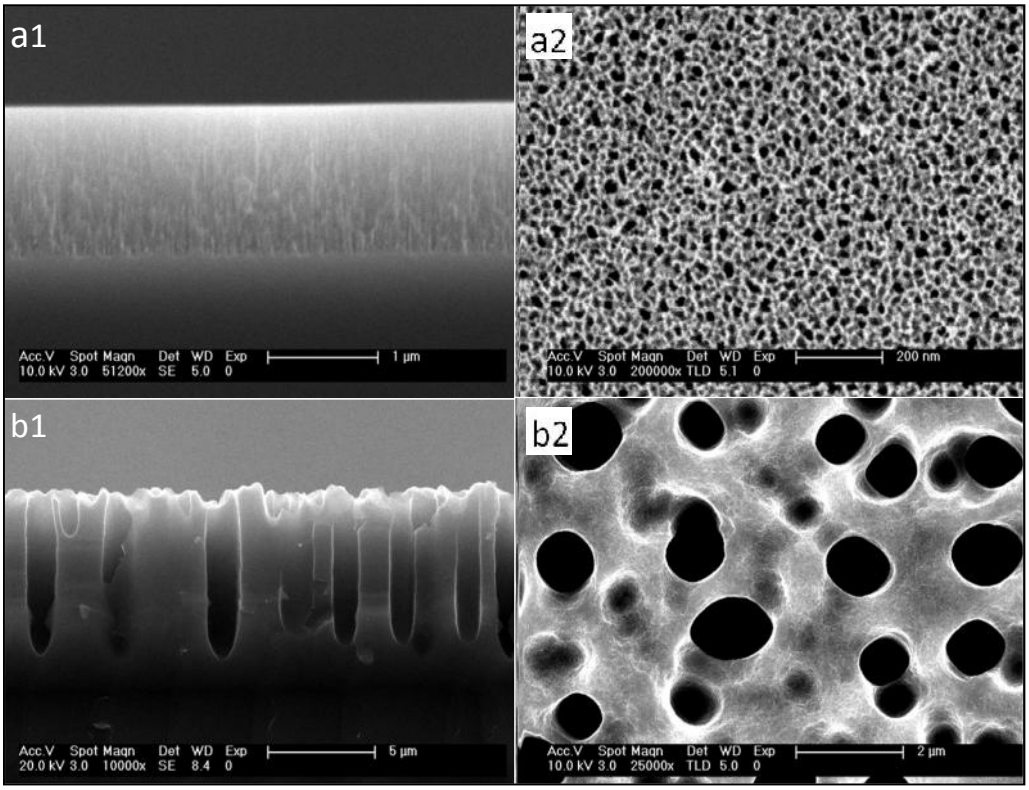

Figure 9. FESEM images of nPSi-COx, cross-section (a1) and top view (a2); and mPSi-COx, cross-section (b1) and top view (b2).

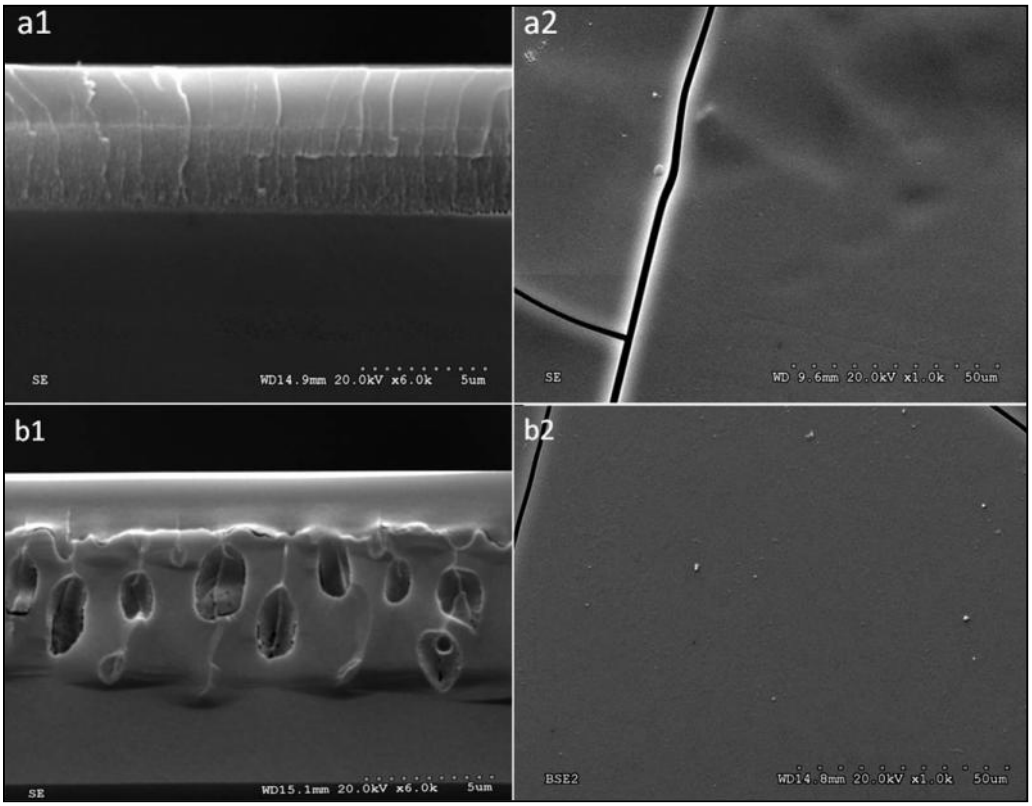

Figure 10. SEM images of nPSi-CD, cross-section (a1) and top view (a2); and mPSi-CD, cross-section (b1) and top view (b2).

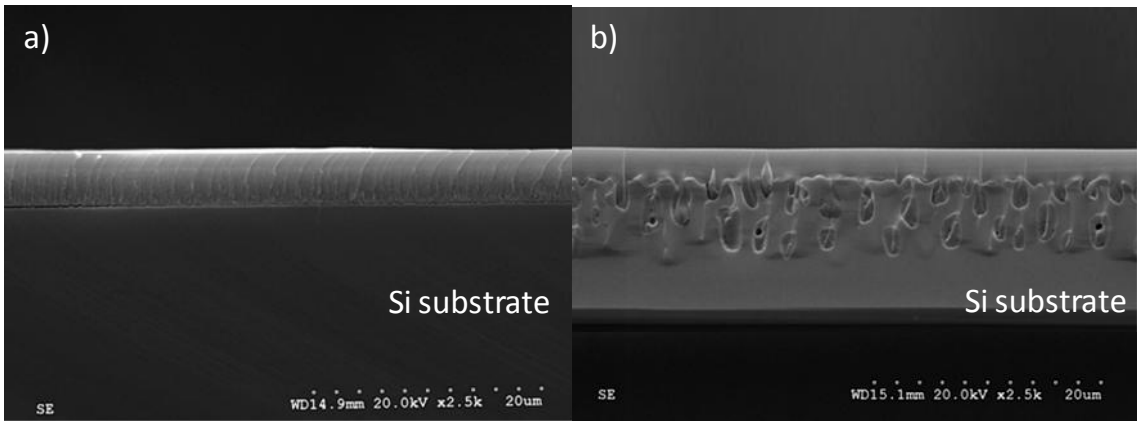

Figure 11. Zoom out SEM images in cross-section of: a) nPSi-CD and b) mPSi-CD.

From the previous chemical and microscopic characterization results, it is possible to explain the binding between the PSi structures (nano- and macro-) and the polyCD. Two phenomena are mainly involved; one chemical, the hydrophilic compatibility of oxidized PSi samples with the external wall of CD's that is full of OH bonds [27], and other physical, the porosity of samples works as an anchor holding the polymer film (Fig. 7 and Fig. 10).

3.3.3 Degree of PSi functionalization by polyCD

In order to evaluate the functionalization degree in PSi/CD hybrids, TGA and gravimetric measurements were performed. Firstly, the thermogravimetric analysis of the polyCD was monitored as reference (Fig. 12). The polymer decomposition is clearly appreciable. The first stage starts at around 200°C reaching the maximum peak around 300 °C where a dominant part of the glucose units are melted, decomposed and turned into char [28]. The last narrow peak is identified at around 475 ºC and is associated to the degradation of this char residue [28].

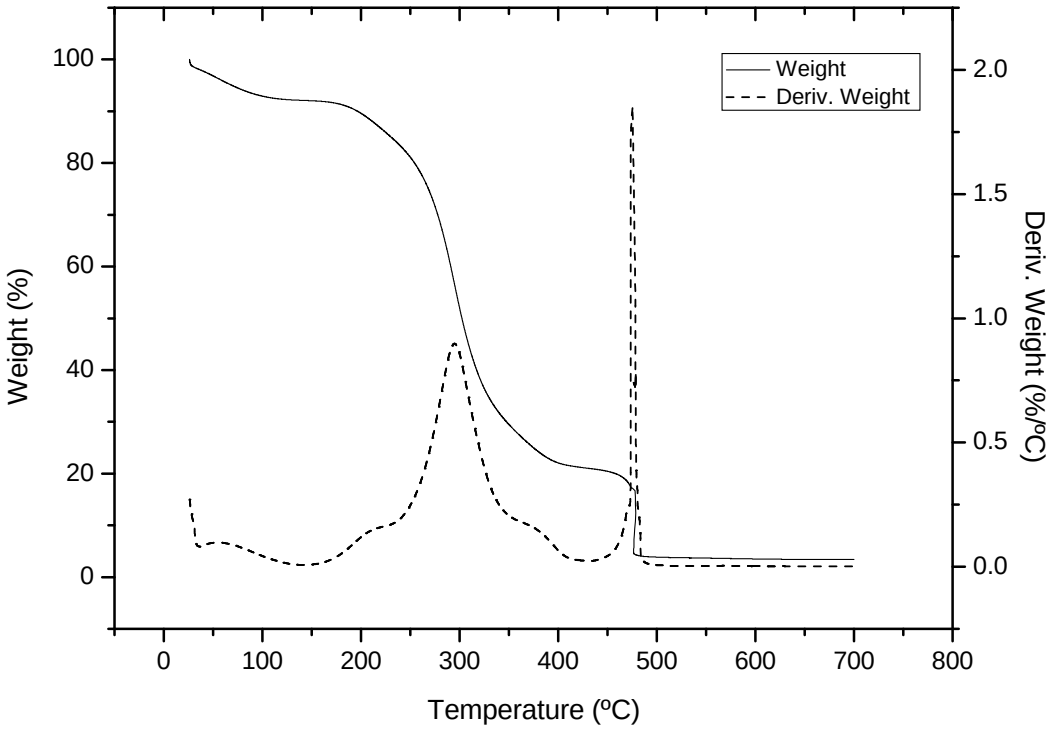

Figure 12. Thermogravimetric analysis of a polyCD control.

The results of thermogravimetric analysis of hybrids are shown in Fig. 13. The plot in Fig. 13-a corresponds to the nano- sample series. The solid lines indicate the weight (left axis) as a function of temperature and the dotted lines its derivative (right axis). In the case of nPSi-COx, one can observe that mass increases with temperature. This is because of oxygen incorporation to the sample by thermal oxidation induced during TGA. This confirms that nPSi chemical oxidation by H_2O_2 is a partial surface oxidation [16]. Nevertheless, the phenomenon is gradual with the derivative curve monotonically growing at decreasing rate. On the other hand, the polymer decomposition in nPSi-CD is noticeable. As in the case of the reference, the phenomenon starts at 200 °C, reaching the maximum peak around 300 °C where glucose is decomposed into char. Nevertheless, the last stage associated to char degradation is produced at a lower temperature (435 ºC). TGA results from macro- sample series are plotted in Fig. 13-b. One can observe that mPSi-COx acquired less mass than nPSi-COx, this is due to a lower oxidation in this sample associated to the lower surface density. The mPSi-CD sample shows a similar behavior than nPSi-CD with the two important stages: one starting at around 200 °C, which reached the maximum at 300 ºC, and other at 450 ºC, which is also observed at lower temperature than for the reference sample. Although TGA analyses of functionalized samples revealed differences with respect to the reference, they denote the

presence of β-cyclodextrin and citric acid in both hybrids. The shift to lower temperatures of the char degradation in both hybrids could be due to the increasing of surface area in PSi substrates. A larger surface area facilitates heat transfer and thus nPSi-CD exhibits a lower char degradation temperature than mPSi-CD.

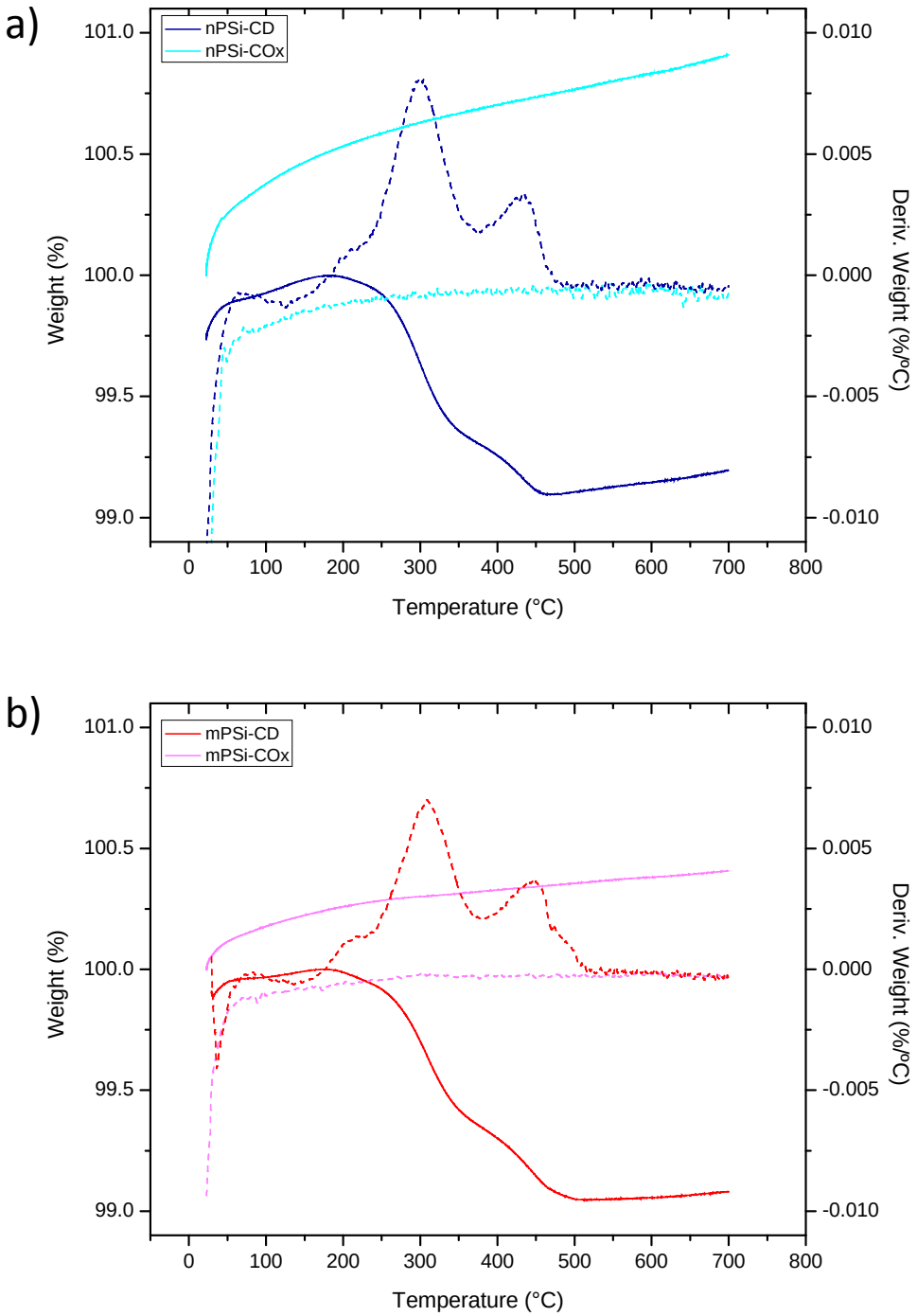

Figure 13. Thermogravimetric analysis of: a) nPSi- samples and b) mPSi- samples before and after CD modification. The solid lines indicate the weight (left axis) and the dotted lines its derivative (right axis).

In order to measure the functionalization degree of polyCD onto the oxidized samples (nPSi-COx and mPSi-COx), it was necessary to remove the contribution of the silicon substrate to total weight (see Fig. 11). This was achieved by gravimetric measurements and TGA. The surface densities and calculated fixed polymer amounts are shown in Table 2. Results indicate a surfacic weight increase from oxidized samples to the functionalized ones from 0.49 to 1.16 mg/cm² (+136.74%) and from 1.79 to 2.64 mg/cm² (+47.79%) for nPSi and mPSi samples respectively. The estimated differences of polyCD were 0.67 and 0.85 mg/cm², respectively. So the polymer composition per surface area of PSi (mg/cm^2) was 1.27 times higher in mPSi-CD compared to nPSi-CD. A reverse proportion was observed if the weight of polyCD is considered per unit of weight of nPSi and mPSi. The values were 1.37 and 0.47 mg/mg, respectively (rightmost column of Table 2). Thus, the ponderated composition of nPSi-CD in polyCD was 2.91 times that of mPSi-CD. This result can be attributed to the large difference of surfacic mass between both support materials (leftmost column of Table 2).

Table 2. Surfacic mass and polymer amounts calculated from TGA.

Sample	**mg PSi /cm^2**	**mg polyCD-PSi /cm^2**	**mg polyCD /cm^2 PSi**	**mg polyCD /mg PSi**
nPSi-	0.49 (±0.03)	1.16 (±0.08)	0.67 (±0.04)	1.37 (±0.09)
mPSi-	1.79 (±0.14)	2.64 (±0.21)	0.85 (±0.07)	0.47 (±0.04)

The amount of immobilized polymer on PSi surfaces was also indirectly measured by detecting –COOH groups by TBO titration (Fig. 14). Data were reported as a function of area and mass of the composite, that is to say, the polymer and PSi considered as a whole (for nPSi-CD and mPSi-CD). The TBO loaded normalized to PSi surface area in mPSi-CD (0.975 μmol/cm^2) more than doubled that in nPSi-CD (0.463 μmol/cm^2) but the load normalized to PSi mass was almost the same in both cases; just 8% more in nPSi-CD (0.40 μmol/mg) with respect to mPSi-CD (0.37 μmol/mg).

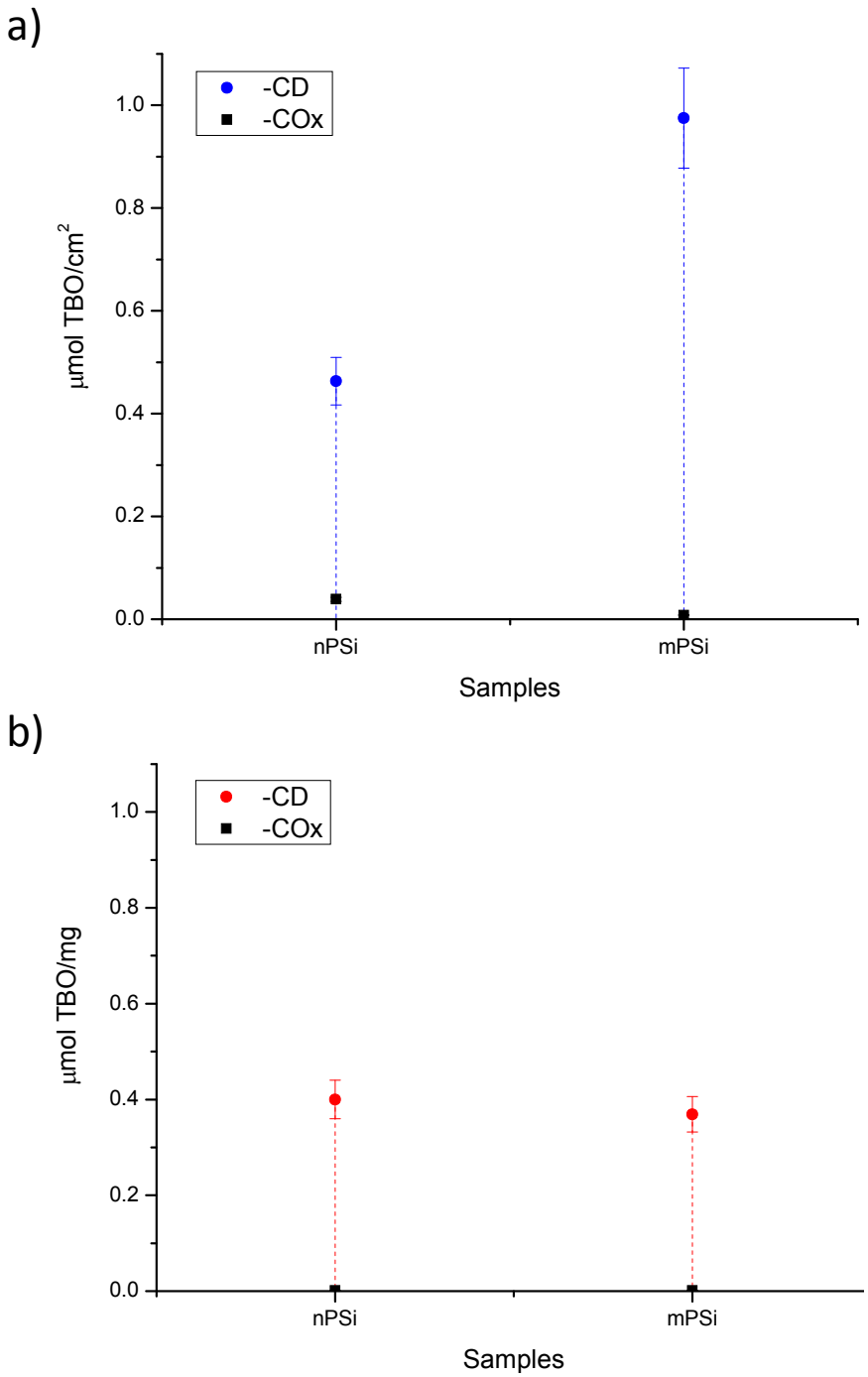

Figure 14. The TBO loaded into different PSi supports according to: a) PSi surface area normalization (µmol/cm^2) and b) PSi mass normalization (µmol/mg).

3.3.4 Biological evaluation

The cytocompatibility of the PSi-CD samples was tested *in-vitro* by studying the adhesion of L132 cells after 24 h of culture (Fig. 15). The cells adhered to the surfaces of all samples, giving a first positive estimation of biocompatibility [29]. However, the

adherent cells on the samples also presented strong differences in morphology, indicating that the evolution of cells in terms of cell growth in longer culture experiments might be considerably different [30]. On nPSi, SEM images show that cells were isolated and presented a contracted semispherical form (Fig 15-a1). Besides, few and short filopodia were observed (white arrows in Fig. 15-a2). These two characteristics denote that the cells did not fully-adhere on the substrate [31]. In the case of cells on nPSi-CD, cell bodies were oval with extended lamellipodia (Fig. 15-b1). Around their body, numerous filopodia were extended anchoring the cell to the surface (white arrows in Fig. 15-b2). Those signs imply a better adhesion to the surface and their elongated cytoskeleton can be interpreted in terms of a migratory state [31]. Cells on mPSi were spread and closely contacted to the surface (Fig. 15-c1). Moreover, some filopodia are observed in the higher-magnification image in Fig. 15-c2 (white arrows), which confirms that mPSi is better suited to support cells than nPSi [32]. Finally, it was found, in the case of mPSi-CD, that the polymer coating layer on the top surface was not strong enough to resist the cell culture or process of SEM sample preparation. The top polymer layer peeled off from the substrate (inset SEM image of Fig. 15-d1) and probably carried away the adherent cells. Consequently, the cells were observed only in restricted areas of the sample. Relevantly, in spite of the absence of the top polyCD layer, there were pores refilled with polymer remnants. The cells were drastically elongated under this materials configuration and slightly repelled substratum in their central area, minimizing the contact with the surface (Fig. 15-d1). Although there were no observable filopodia (Fig. 15-d2), their long stretched shape suggest again a migratory state [25].

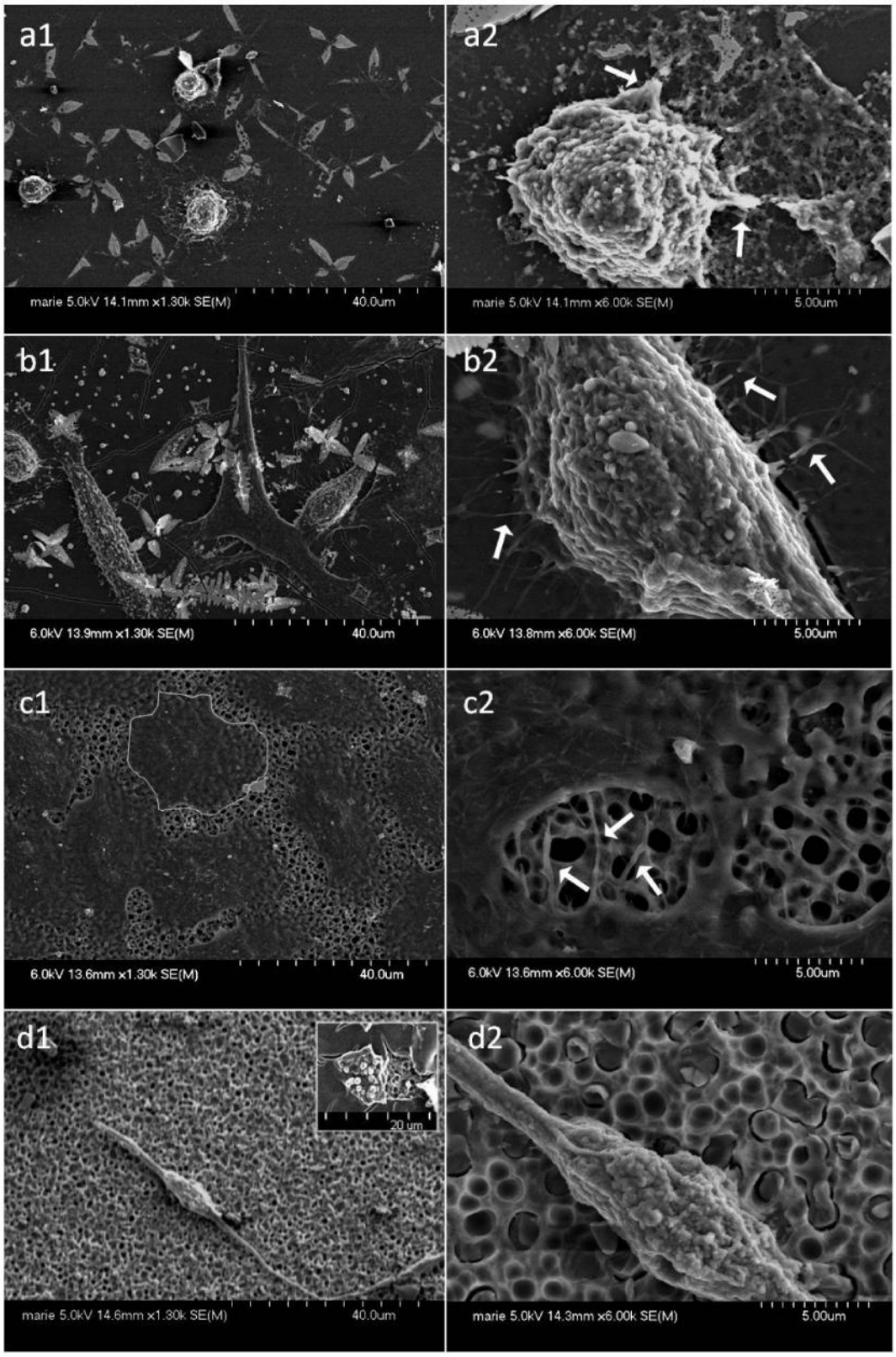

Figure 15. SEM images of L132 cells after 24 h culture on: nPSi (a1 and a2), mPSi (b1 and b2), nPSi-CD (c1 and c2) and mPSi-CD (d1 and d2).

3.3.5 Study of drug delivery

In order to test the layered hybrids as potential intraocular drug delivery system, the samples were loaded with the ophthalmic drugs CFX and PDN (see Fig. 30 of Section 2.2.3 in Chapter 2).

The elemental surface compositions of the nPSi-CD before and after drug loadings was obtained from the XPS survey spectra and are presented in Table 3.

Table 3. Surface chemical compositions of nPSi-CD obtained before and after drug loadings from XPS analysis.

Sample	**C (at%)**	**O (at%)**	**N (at%)**	**Si (at%)**	**F (at%)**
nPSi-CD	56.9 (±0.5)	43.0 (±0.24)	--	--	--
nPSi-CD-CFX	61.5 (±0.3)	31.6 (±0.2)	4.5 (±0.24)	0.4 (±0.2)	1.4 (±0.2)
nPSi-CD-PDN	58.2 (±0.6)	40.4 (±0.53)	1.1 (±0.01)	0.1 (±0.02)	--

The loading of CFX is demonstrated by the appearance of N and the emerging of F signals (three and one atoms per CFX molecule, respectively) not detected in the unloaded samples (Table 3). The analyses show also a slight surface contamination by silicon and, in the case of nPSi-CD-PDN, also nitrogen. The analysis of the C1s core level spectrum (Fig. 16-b) further supports this conclusion. In fact, after CFX loading, the intensity of the hydrocarbon component at 285eV increases slightly. Moreover, the FWHM of the C1 and C2 components increases indicating the presence of C-N and CN(O) bonds and also of C-F (expected at about 289.0 eV). In addition, the C3 component shifts toward lower binding energy (about 0.22eV) also supporting the formation of COO type bonds. On the other hand, in the case of PDN loading, the XPS analysis is not so indicative of its presence on the surface since there are no additional elements in PDN to those present on the nPSi-CD surface. However, the increase of the C3 (C=O) and C0 (C-C) components in the C1s core level spectra (Figure 16-c) are compatible with an enrichment on PDN in view of the presence of two C=O carbons and 13 C-C carbons in the PDN molecule.

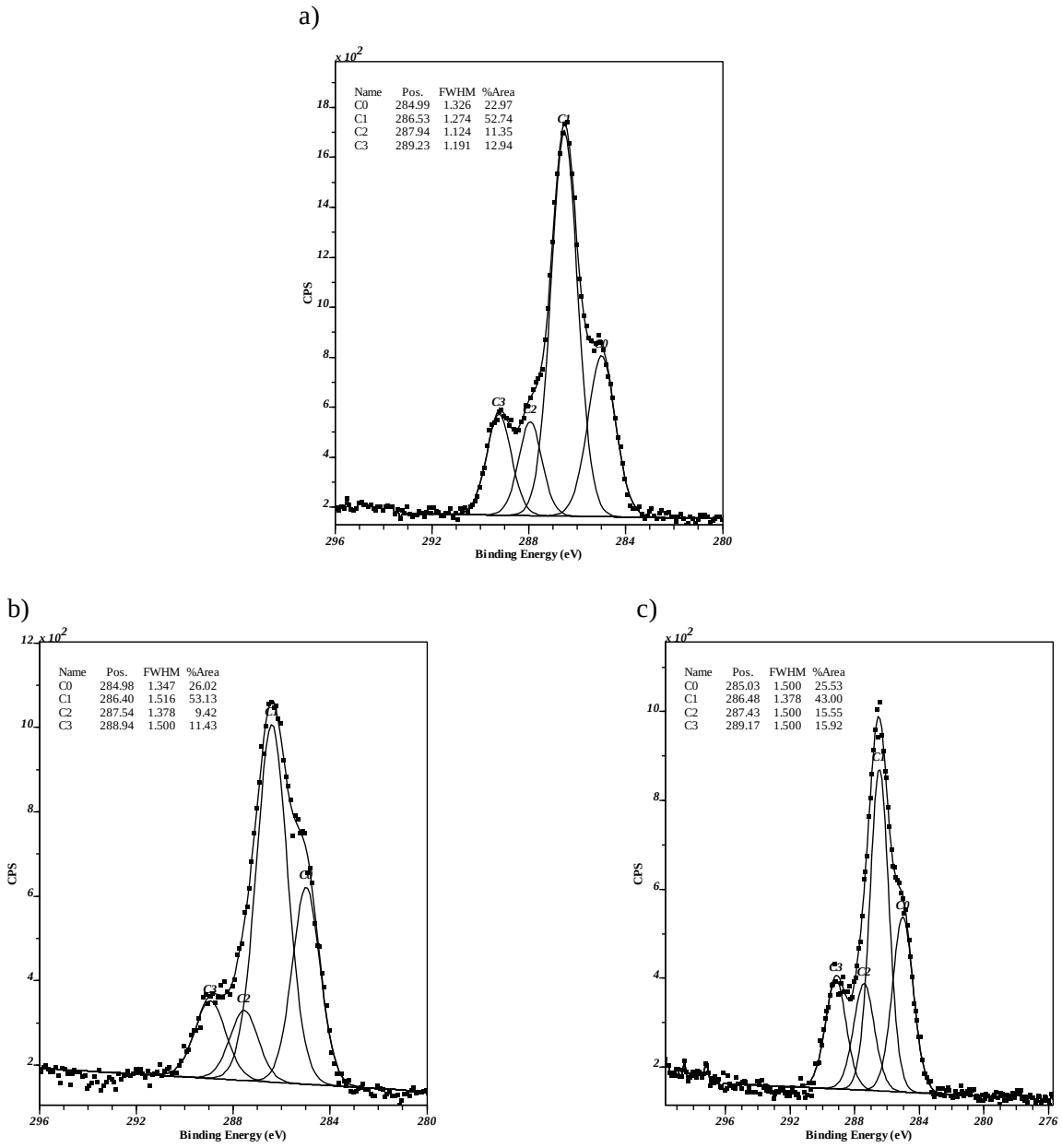

Figure 16. C1s core level spectra of a) nPSi-CD, b) nPSi-CD after CFX loading and c) nPSi-CD after PDN loading.

To summarize the whole process of hybrid synthesis and loading, an evolution of surface chemical composition of samples measured by XPS is shown in Fig. 17. Each synthesis step is represented: nPSi formation, chemical oxidation, CD polymerization and drugs loading.

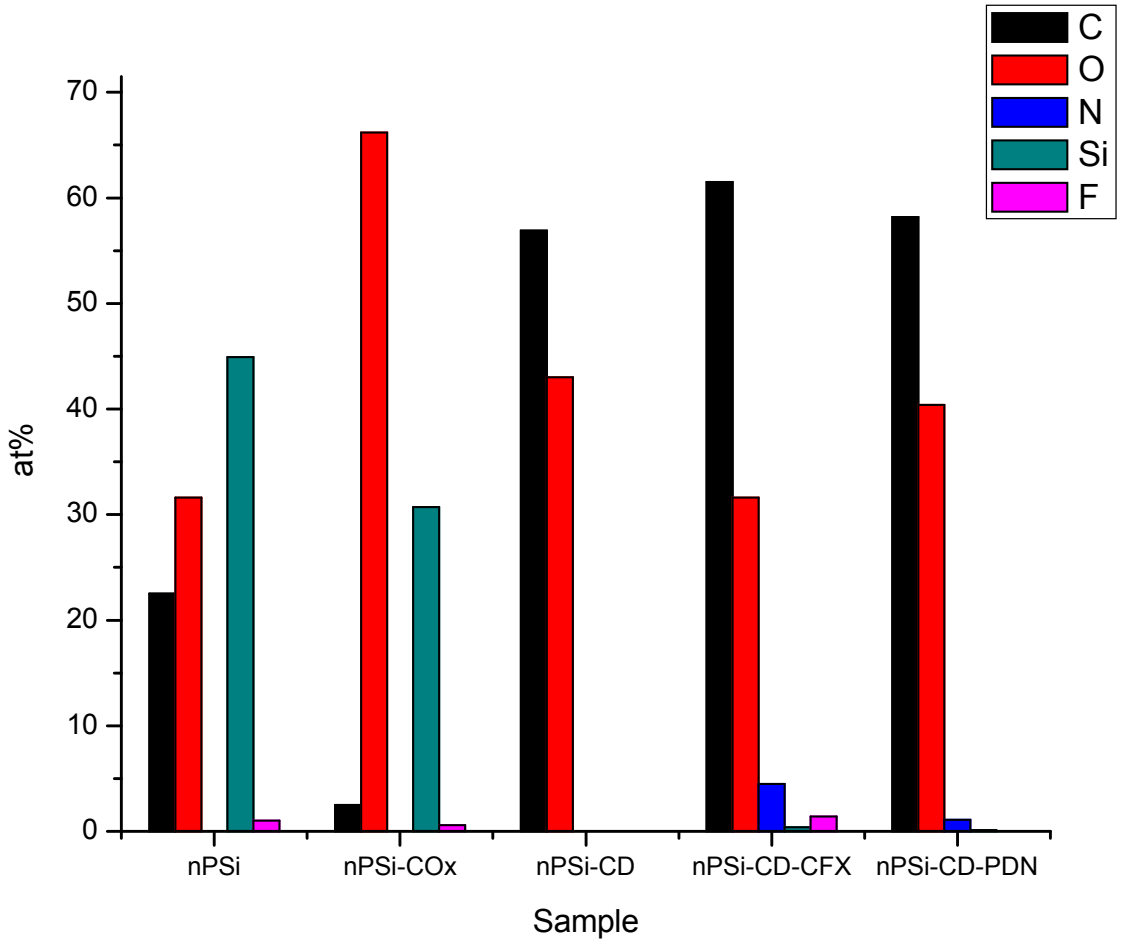

Figure 17. Evolution of surface chemical composition measured by XPS: a)PSi recently formed, nPSi; b) after chemical oxidation, nPSi-COx; c) after polymerization; nPSi-CD; d) after CFX loading, nPSi-CD-CFX; and e) after PDN loading, nPSi-CD-PDN.

In a last step for evaluating the drug delivery functionality of the composites, the samples were tested with CFX and PDN in water and PBS batches under stirring. CFX release profiles in distilled water are shown in Fig. 18. The profiles of Fig. 18-a correspond to the drug release as a function of sample area and the profiles of Fig. 18-b report the drug release as a function of sample mass. The equivalent profiles obtained in PBS are shown in Fig. 19-a and Fig. 19-b.

The four release profiles in Fig. 18 and Fig. 19 clearly show that CD-functionalized PSi samples worked much better than COx control samples. The COx samples retained a small amount of drug, which was released during the first minutes. In the case of functionalized samples, the maximum yield of loaded drug per sample area was 140% higher in mPSi-CD than in nPSi-CD. With regards to drug release as a function of sample mass, the increase was 19% higher in mPSi-CD than in nPSi-CD.

These results matched with those obtained by TBO titrations. Plots of molecule load per sample area indicate a significant advantage for mPSi-CD, but no significant differences are observed when plots refer to normalization to sample mass.

CFX release profiles expressed in percent of maximum drug release are shown in Fig. 20. In the CFX profiles in distilled water (Fig. 20-a) there is a clear contrasting behavior between the fast release of unfunctionalized samples with respect to the controlled release of functionalized samples. Nevertheless, in the case of CFX release profiles in PBS (Fig. 20-b) the release in terms of percent of maximum drug release is similar between unfunctionalized and functionalized samples. Comparing the profiles of functionalized samples in both media one can observe that CFX release was 45-fold faster in PBS medium (4 h) than in distilled water (180 h). This can be induced by three main effects [33]: a) The competitor role of ions in PBS towards drug-CD inclusion complex. This means that the ions displace the drug from the CD ring. b) The possible ionic interactions between the protonated amino functions of CFX and the carboxylate groups of polyCD are screened by the exceeding counterions brought by PBS. c) At neutral pH the carboxylic groups of CD's turn into carboxylate groups ionically repelling the CFX carboxylate group from the polymer network. A combination of these three aspects takes probably account for the accelerated release of CFX in PBS compared to pure water.

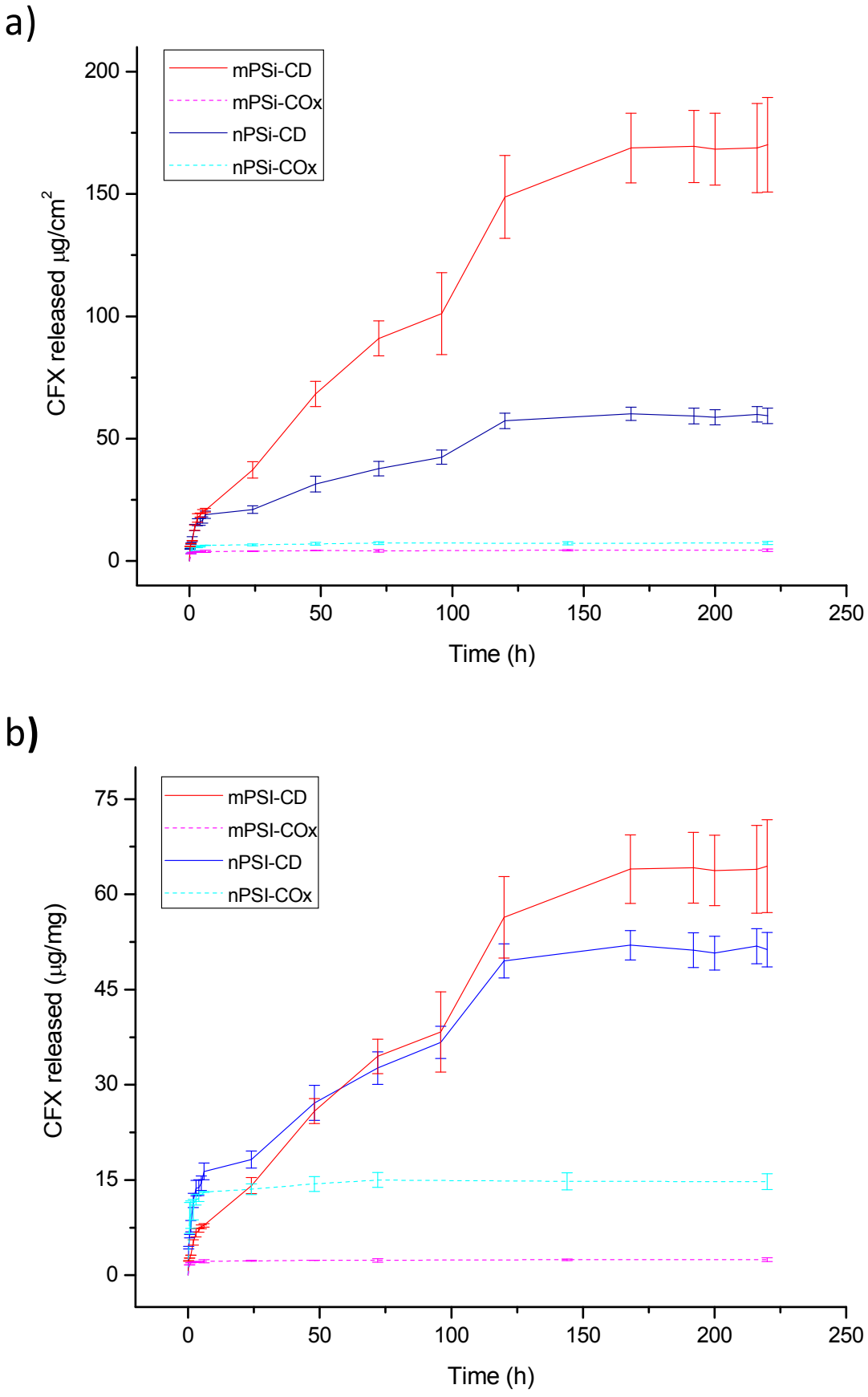

Figure 18. CFX release profiles in distilled water normalized to sample area (a) and to sample mass (b).

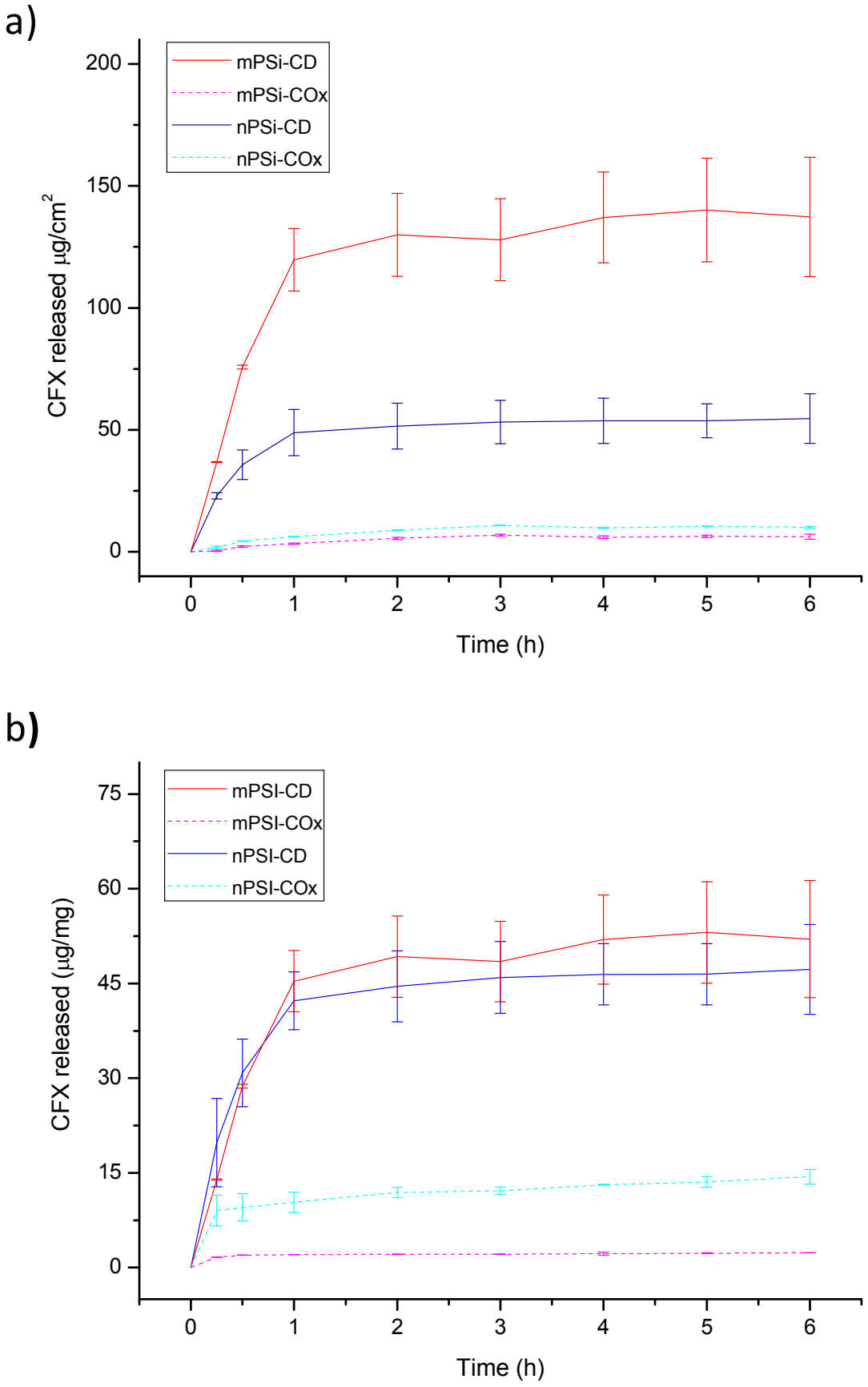

Figure 19. CFX release profiles in PBS normalized to sample area (a) and to sample mass (b).

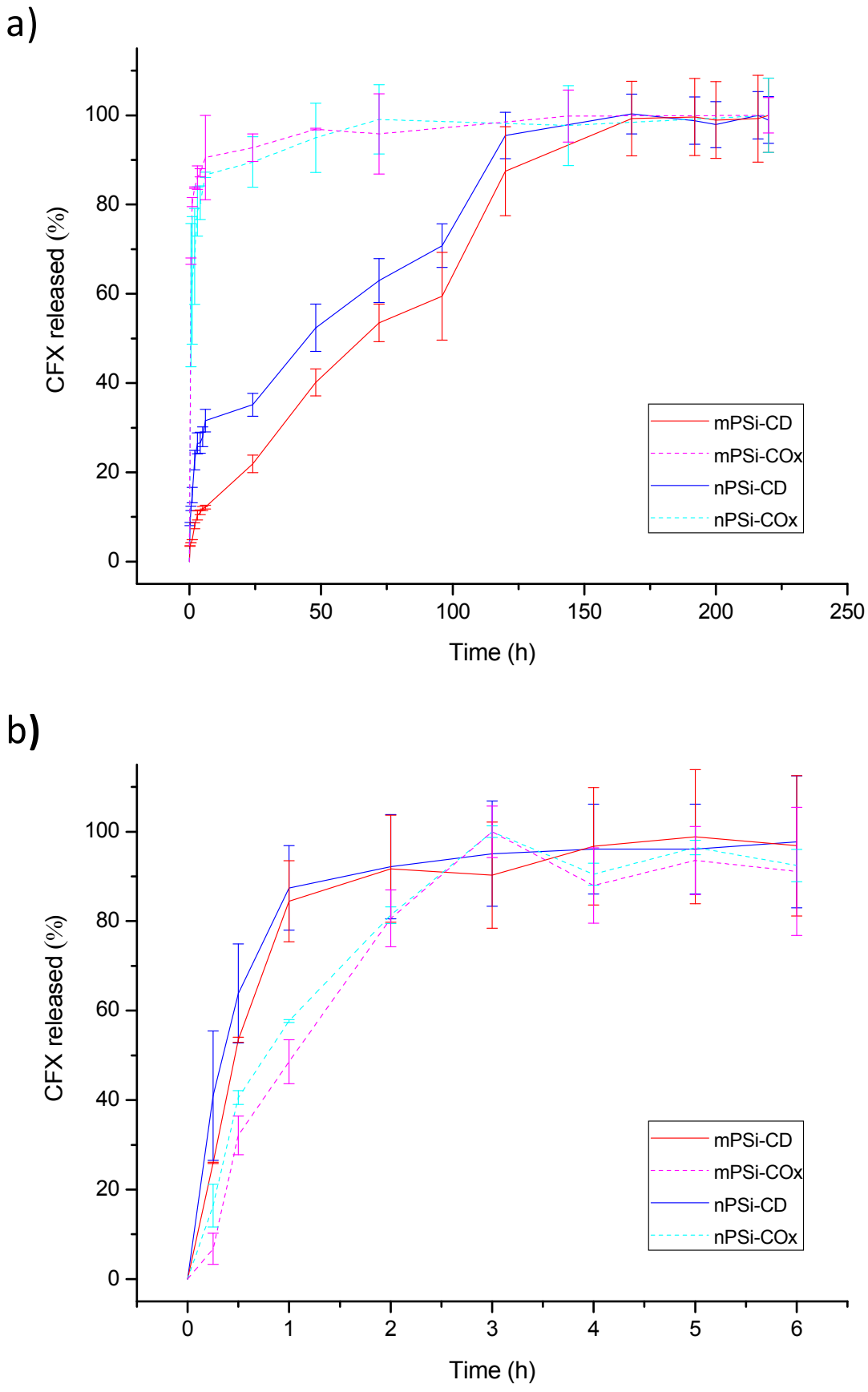

Figure 20. CFX release profiles as percent of maximum drug release in distilled water (a) and in PBS (b).

PDN release profiles in distilled water and in PBS are shown in Fig. 21 and Fig. 22, respectively. In the case of nPSi-CD samples, they retained significantly more drug than unfunctionalized ones; but in the case of mPSi-CD, they loaded similar amount drug as unfunctionalized samples. Nevertheless, the release of mPSi-CD samples is more controlled than in COx ones. The drug yield per sample area was 220% higher in mPSi-CD than in nPSi-CD, and per sample mass was 40% higher in mPSi-CD than in nPSi-CD. This tendency is also similar to what was observed for CFX and during TBO titration. The functionalization degree normalized to sample area magnifies delivery rates in favor of mPSi-CD, although data normalized to sample mass do not show such significant differences.

Release time of PDN was also affected by the medium of release. The PDN release of CD functionalized samples was around 32 fold faster in PBS medium (2.5 h) than in distilled water (80 h) (Fig. 23).

From all these release profiles, it is possible to indicate that CFX is more compatible with both hybrids (nPSi-CD and mPSi-CD) than PDN. CFX load was 10-fold that of PDN. On the other hand, the release time was also longer for CFX than for PDN in both hybrids: 2.25 times longer in distilled water and 1.6 times longer in PBS.

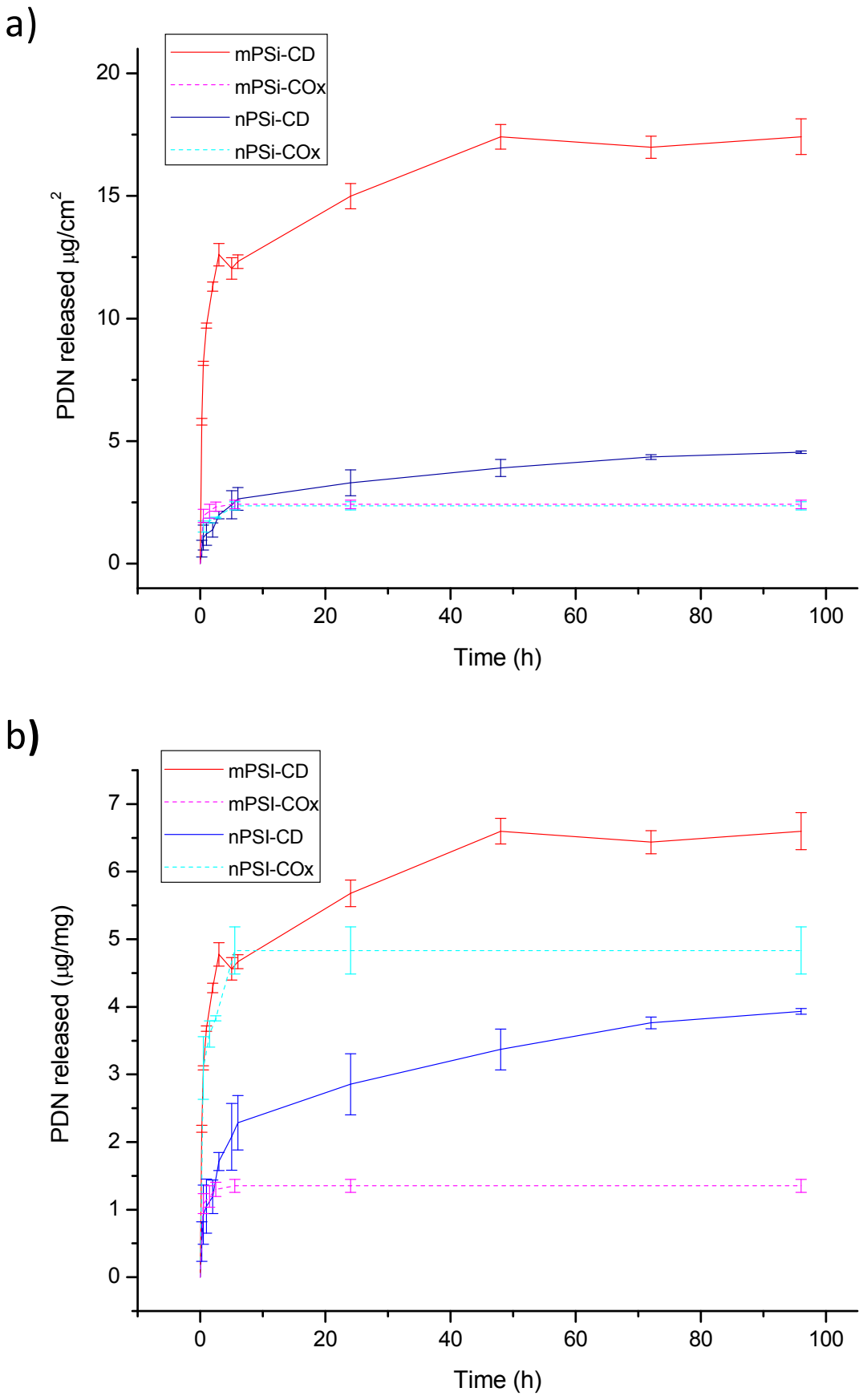

Figure 21. PDN release profiles in distilled water normalized to sample area (a) and to sample mass (b).

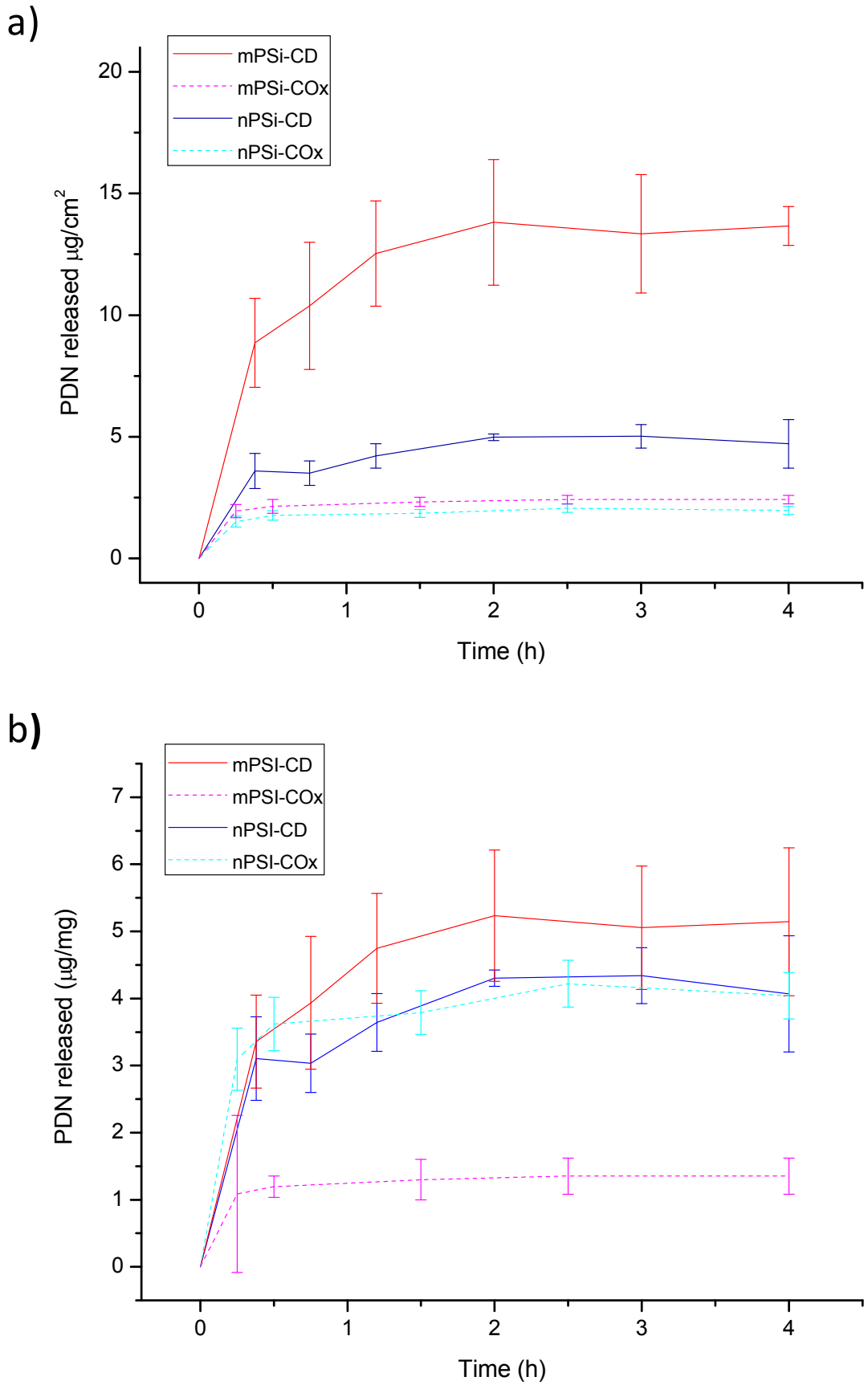

Figure 22. PDN release profiles in PBS normalized to sample area (a) and to sample mass (b).

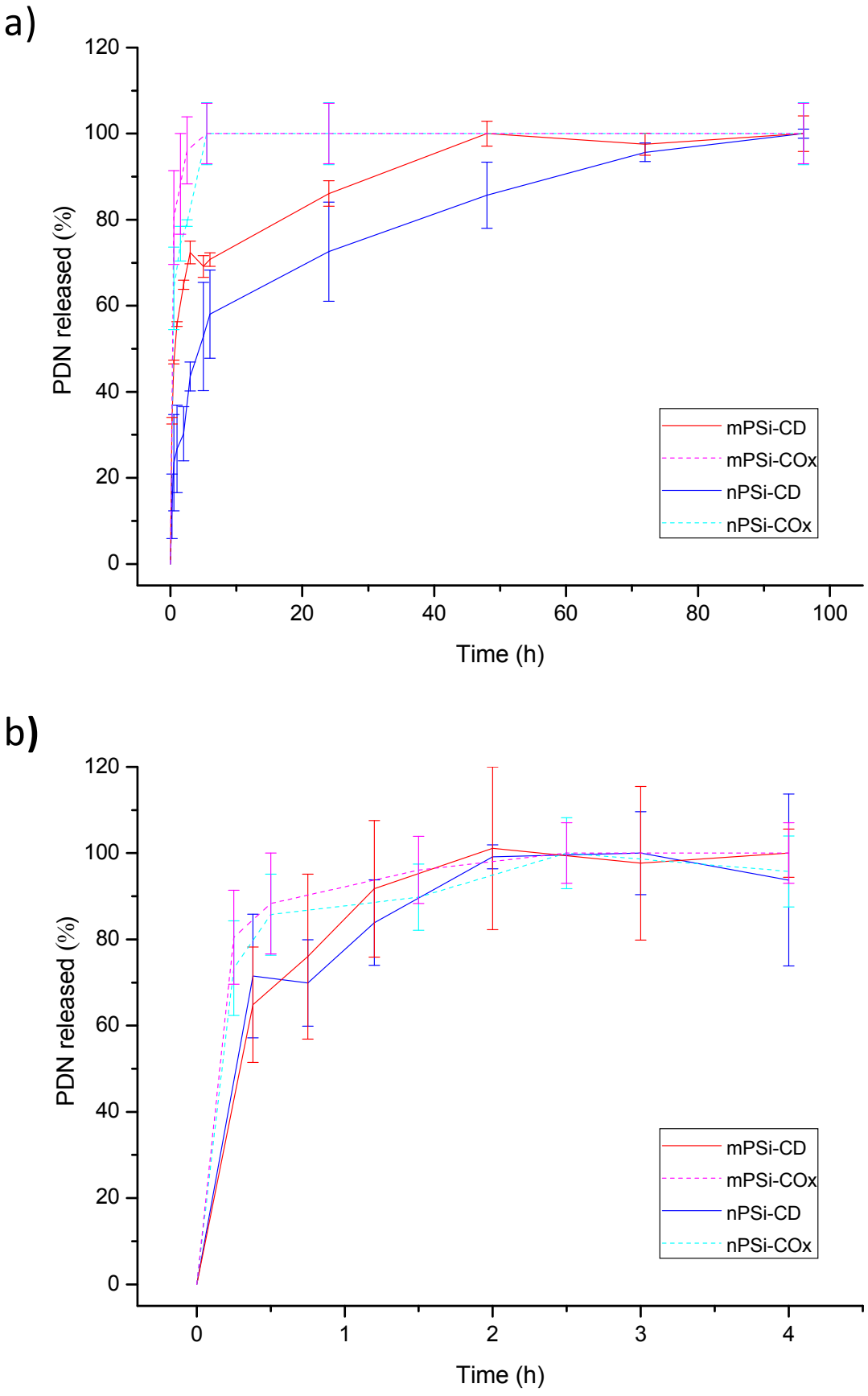

Figure 23. PDN release profiles as percent of maximum drug release in distilled water (a) and in PBS (b).

3.4 Conclusions

Results from FTIR, XPS and water contact angle indicated that nano and macro PSi layers were satisfactorily synthesized, properly stabilized by chemical oxidation and further functionalized by β-cyclodextrin *in-situ* polymerization using citric acid as crosslinking agent. The microscopic characterization showed clear topographic changes of surfaces after each step (AFM) and that the polymer is integrated in PSi pores and top surface (SEM). The amalgamation between the porous matrix and the polymer was favored by two main phenomena: the PSi hydrophilic compatibility with the external wall of CD after chemical oxidation, and the anchoring effect of the porous matrix. On the other hand, the deposition and *in vitro* proliferation of L132 cells on both reference samples and both composites proved their biocompatibility, despite their different cell growth behavior on each sample.

Drug release profiles showed that functionalized samples have a longer release time than COx ones. Higher drug loads are achieved and provide a better-controlled release. The profiles were reported in two ways, normalized to area and normalized to sample mass. The results significantly favor mPSi-CD over nPSi-CD when normalized to area, but when results are normalized to mass they are similar due to nPSi being lighter than mPSi.

The studies also indicated that CFX is more compatible with both composites (nPSi-CD and mPSi-CD) than PDN: CFX load was 10 times higher than PDN load in both composites. On the other hand, the release time for CFX was longer than for PDN in both composites: one week in distilled water and 4 h in PBS for CFX; more than three days in distilled water and 2.5 h in PBS for PDN. The faster release in PBS is due to the ionic strength of salts in solution.

Finally, it is important to mention that the quantity of drug released by both composites during the kinetic studies, confirms their potential for use in post-ophthalmic surgery. It is reported that the CFX minimum inhibitory concentration required to inhibit the growth of 90% of microorganisms (MIC90) goes from less than 0.25 to 2 μg/mL [34] (less than 0.25 μg/ml for *Bacillus* sp. and *Escherchia* coli, while 0.5 μg/mL for *Corynebacterium* sp. and *Staphylococcus* sp., and 2 μg/mL for *Streptococcus* sp.). As the mean volume of an adult human eye is 6.5 mL [35], the required CFX dose into the eye for a medical therapy is around 13 μg, a value not only reached but exceeded with just 1 mg of both PSi/CD hybrids synthesized.

In the case of the use of PDN as an ocular anti-inflammatory, a minimum concentration of 25 ng/mL is necessary to suppress inflammation and minimize side effects of ophthalmic steroids, such as bulbar perforation, choroidal injection, central retinal artery occlusion and others [36]. We can thus estimate that 0.16 μg of PDN are required for a medical therapy. This value is also reached using 1 mg of any of the PSi/CD hybrids, as derived from the kinetic studies.

In summary, by means of the characterization techniques and *in vitro* drug release studies it was proved that layered composites of PSi and polyCD are functional devices for drug delivery applications in post-ophthalmic surgery.

References

[1] Kumar DS, Banji D, Madhavi B, Bondanapu V, Dondapati S, SRI AP. Nanostructured porous silicon - A novel biomaterial for drug delivery. Int J Pharm Pharm Sci 2009;1(2):8-16.

[2] Thrimawithana TR, Young S, Bunt CR, Green C, Alany RG. Drug delivery to the posterior segment of the eye. Drug Discov Today 2011;16(5):270-277.

[3] Leprêtre S, Chai F, Hornez JC, Vermet G, Neut C, Descamps M, et al. Prolonged local antibiotics delivery from hydroxyapatite functionalised with cyclodextrin polymers. Biomaterials 2009;30(30):6086-6093.

[4] Trotta F, Zanetti M, Cavalli R. Cyclodextrin-based nanosponges as drug carriers. Beilstein J Org Chem 2012;8(1):2091-2099.

[5] Anglin EJ, Cheng L, Freeman WR, Sailor MJ. Porous silicon in drug delivery devices and materials. Adv Drug Deliv Rev 2008;60(11):1266-1277.

[6] Olson RJ. Reducing the risk of postoperative endophthalmitis. Surv Ophthalmol 2004;49(2):S55-S61.

[7] Nardi M, Lobo C, Bereczki A, Cano J, Zagato E, Potts S, et al. Analgesic and anti-inflammatory effectiveness of nepafenac 0.1% for cataract surgery. Clin Ophthalmol 2007;1(4):527.

[8] Sherwood D, Rich W, Jacob J, Hart R, Fairchild Y. Bacterial contamination of intraocular and extraocular fluids during extracapsular cataract extraction. Eye 1989;3(3):308-312.

[9] Thrimawithana TR, Young S, Bunt CR, Green C, Alany RG. Drug delivery to the posterior segment of the eye. Drug Discov Today 2011;16(5):270-277.

[10] Oliver KM, Strube YNJ, Mohan SK, Slomovic AR. Fourth-generation fluoroquinolones in the treatment of mycobacterial infectious keratitis after laser-assisted in situ keratomileusis surgery. Can J Ophthalmol 2005;40(6):750-753.

[11] Ravindran RD, Venkatesh R, Chang DF, Sengupta S, Gyatsho J, Talwar B. Incidence of post-cataract endophthalmitis at Aravind Eye Hospital. J Cataract Refract Surg 2009;35(4):629-636.

[12] Lane SS, Holland EJ. Loteprednol etabonate 0.5% versus prednisolone acetate 1.0% for the treatment of inflammation after cataract surgery. J Cataract Refract Surg 2012;39-2:168-173.

[13] Struck H, Bariszlovich A. Comparison of 0.1% dexamethasone phosphate eye gel (Dexagel) and 1% prednisolone acetate eye suspension in the treatment of post-operative inflammation after cataract surgery. Graefe's Arch Clin Exp Ophthalmol 2001;239(10):737-742.

[14] Mawhinney DB, Glass Jr JA, Yates Jr JT. FTIR study of the oxidation of porous silicon. J Phys Chem B 1997;101(7):1202-1206.

[15] Tolstoy VP, Chernyshova I, Skryshevsky VA. Handbook of infrared spectroscopy of ultrathin films. USA: Wiley-VCH; 2003.

[16] Naveas N, Costa VT, Gallach D, Hernandez-Montelongo J, Palma RJM, Garcia-Ruiz JP, et al. Chemical stabilization of porous silicon for enhanced biofunctionalization with immunoglobulin. Sci Technol Adv Mater 2012;13(4):045009.

[17] Martin A, Tabary N, Leclercq L, Junthip J, Degoutin S, Aubert-Viard F, et al. Multilayered textile coating based on a β-cyclodextrin polyelectrolyte for the controlled release of drugs. Carbohydr Polym 2013;93:718-730.

[18] Zhao D, Zhao L, Zhu C, Tian Z, Shen X. Synthesis and properties of water-insoluble β-cyclodextrin polymer crosslinked by citric acid with PEG-400 as modifier. Carbohydr Polym 2009;78(1):125-130.

[19] Gorbanyuk T, Evtukh A, Litovchenko V, Solnsev V, Pakhlov E. Porous silicon microstructure and composition characterization depending on the formation conditions. Thin Solid Films 2006;495(1):134-138.

[20] Ogata Y, Niki H, Sakka T, Iwasaki M. Oxidation of porous silicon under water vapor environment. J Electrochem Soc 1995;142(5):1595-1601.

[21] Föll H, Christophersen M, Carstensen J, Hasse G. Formation and application of porous silicon. Mat Sci Eng R 2002;39(4):93-141.

[22] Seah M, Spencer S, Bensebaa F, Vickridge I, Danzebrink H, Krumrey M, et al. Critical review of the current status of thickness measurements for ultrathin SiO2 on Si Part V: Results of a CCQM pilot study. Surf Interface Anal 2004;36(9):1269-1303.

[23] Ulgut B, Suzer S. XPS studies of SiO2/Si system under external bias. J Phys Chem B 2003;107(13):2939-2943.

[24] G. Bemason DB. The XPS of polymer database. UK: Surface spectra; 1992.

[25] Low SP, Williams KA, Canham LT, Voelcker NH. Evaluation of mammalian cell adhesion on surface-modified porous silicon. Biomaterials 2006;27(26):4538-4546.

[26] Noval AM, Vaquero VS, Quijorna EP, Costa VT, Pérez DG, Méndez LG, et al. Aging of porous silicon in physiological conditions: cell adhesion modes on scaled 1D micropatterns. J Biomed Mater Res A 2012;100(6):1615-1622.

[27] Davis ME, Brewster ME. Cyclodextrin-based pharmaceutics: past, present and future. Nat Rev Drug Discov 2004;3(12):1023-1035.

[28] Skiba M, Lahiani-Skiba M. Novel method for preparation of cyclodextrin polymers: physico-chemical characterization and cytotoxicity. J Incl Phenom Macrocycl Chem 2012:1-9.

[29] Blanchemain N, Chai F, Haulon S, Krump-Konvalinkova V, Traisnel M, Morcellet M, et al. Biological behaviour of an endothelial cell line (HPMEC) on vascular prostheses grafted with hydroxypropylgamma-cyclodextrine (HPγ-CD) and hydroxypropylbeta-cyclodextrine (HPβ-CD). J Mater Sci Mater Med 2008;19(6):2515-2523.

[30] Blanchemain N, Aguilar M, Chai F, Jimenez M, Jean-Baptiste E, El-Achari A, et al. Selective biological response of human pulmonary microvascular endothelial cells and human pulmonary artery smooth muscle cells on cold-plasma-modified polyester vascular prostheses. Biomed Mater 2011;6(6):065003.

[31] Khung Y, Barritt G, Voelcker N. Using continuous porous silicon gradients to study the influence of surface topography on the behaviour of neuroblastoma cells. Exp Cell Res 2008;314(4):789-800.

[32] Sun W, Puzas JE, Sheu T, Liu X, Fauchet PM. Nano-to Microscale Porous Silicon as a Cell Interface for Bone-Tissue Engineering. Adv Mater 2007;19(7):921-924.

[33] Blanchemain N, Karrout Y, Tabary N, Bria M, Neut C, Hildebrand H, et al. Comparative study of vascular prostheses coated with polycyclodextrins for controlled ciprofloxacin release. Carbohydr Polym 2012;90:1695-1703.

[34] Yu-Speight AW, Kern TJ, Erb HN. Ciprofloxacin and ofloxacin aqueous humor concentrations after topical administration in dogs undergoing cataract surgery. Vet Ophthalmol 2005;8(3):181-187.

[35] Festa F, Pagnoni M, Valerio R, Rodolfino D, Saccucci M, d'Attilio M, et al. Orbital Volume and Surface After Le Fort III Advancement in Syndromic Craniosynostosis. J Craniofac Surg 2012;23(3):789-792.

[36] McGhee C. Pharmacokinetics of ophthalmic corticosteroids. Br J Ophthalmol 1992;76(11):681-684.

Chapter 4:

PSi/Calcium Phosphate Bioceramic Cell Scaffolds

4.1 Introduction

Scaffold-based osseous tissue engineering aims at repairing/regenerating bone defects. Such a treatment involves seeding autologous cells throughout a biodegradable scaffold to create a scaffold–cell hybrid [1]. Human mesenchymal stem cells (hMSCs) derived from bone marrow are the most viable cells to contribute to the regeneration of osseous tissues due to their potential to either, divide to produce more stem cells or to *differentiate* into one or more tissues cells. That is to say, unspecialized hMSC cells become specialized cells, for regeneration of tissues such as bone, cartilage, muscle, ligament, tendon, adipose or stroma [2] (Fig. 1).

In this regard, porous silicon (PSi) provides an excellent platform for cell scaffolds due to its biocompatibility [3], biodegradability [4] and bioresorbability [5]. To promote its application as bone engineering scaffold supporting hMSCs, deposition of calcium phosphate (CaP) ceramics in its hydroxyapatite (HAP, $Ca_{10}(PO_4)_6(OH)_2$) phase has been suggested. This is because HAP is the main inorganic extracellular matrix component of skeleton cells [6,7], supporting mobility [6], calcium reserve [8] and its role in the regulation of metabolic energy [8-10]. HAP is a biocompatible and bioactive material, capable of guiding bone formation and providing direct chemical bonds with natural bone [8,11]. In Fig. 2, the phenomena that occur on the surface of HAP after implantation is schematized: 1) In a fist stage after implantation, solubilization and ionic exchange from the HAP surface start. 2) The solubilization of the HAP surface continues a certain period depending on the electrolytic properties of the implantation medium. 3) An equilibrium is reached between physiological ions and the modified surface of HAP. 4) Upon stabilization, the adsorption of proteins and organic material can proceed. 5-6) The proteinaceous biofilm formed triggers Cell adhesion and proliferation. 7) Cells can

initiate the production of new bone. 8) New bone is formed exhibiting natural bone metabolism. For this reason synthetic HAP and other CaP phases have been used as bone substitute materials in orthopaedics and dentistry applications [12-15].

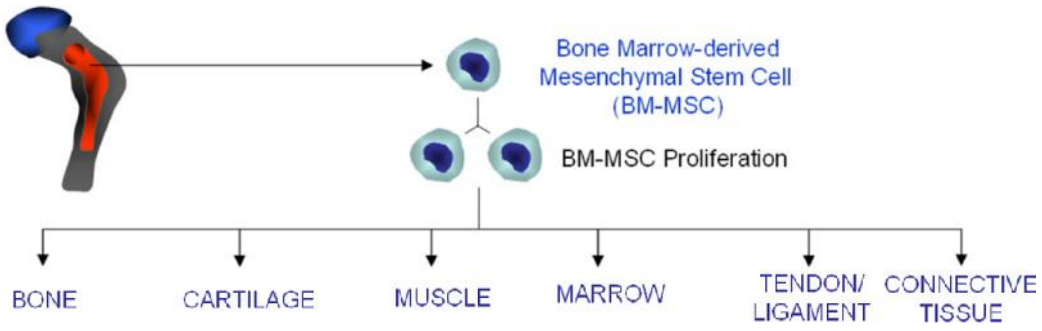

Figure 1. Scheme of hMSCs differentiation (from Seong et. al. [7]).

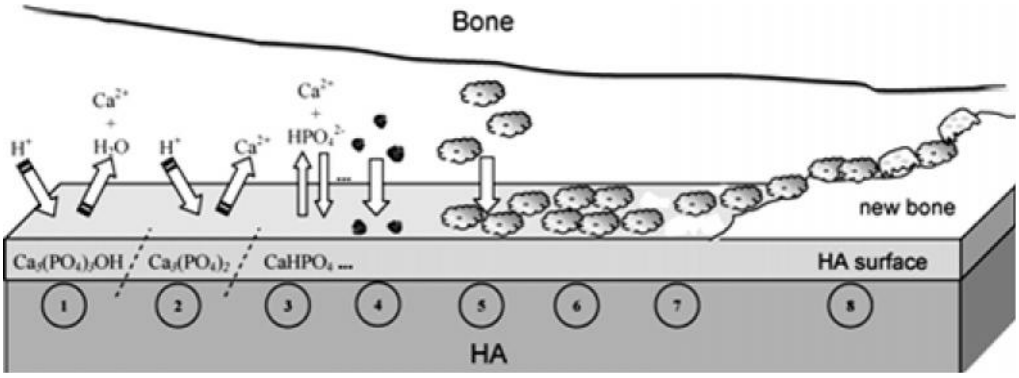

Figure 2. Schematic diagram of the HAP surface after implantation. 1) Solubilization and ionic exchange of the HAP surface. 2) Continuation of the HAP solubilization. 3) Equilibrium between physiological solutions and HAP surface. 4) Adsorption of proteins. 5-6) Cell adhesion and proliferation. 7) New bone production. 8) New bone formed (from Bertazzo et. al. [8]).

In that sense, this work focuses on the synthesis of PSi/CaP bioceramic cell scaffolds by means of two different techniques for CaP deposition on PSi: Cyclic Spin Coating (CSC) and Cyclic Electrochemical Activation (CEA) [16]. Since CaPs are ionic compounds, both methods consist on alternate calcium (Ca) and phosphate (P) deposition steps on nanostructered PSi. In this way, the individual variables of each step such as pH, current density and reaction time, can be controlled and studied independently.

Herein, PSi/CaP composites synthesized through both processes are structurally, morphologically and chemically studied in order to compare their ability to crystallize in the HAP phase. Additionally, in the case of CEA deposition, we aim at monitoring the CaP growth on PSi by the resistance increase of the electrodeposition process, in order to open an understanding of the CaP growth mechanism.

Moreover, HAP and other CaP phases present well defined Ca/P atomic ratios, which are related to their degree of bioresorbability: a higher Ca/P ratio leads to a lower bioresorbability rate [17-20]. This parameter is also linked to stability and bioactivity of CaPs. Therefore, the growth of PSi/CaP composites with tailored bioresorbable properties requires a precise control of the Ca/P ratio. Considering the stratified distribution of the CaP phases deposited, we aim at a determination of the Ca/P atomic ratio by RBS [21].

Furthermore, the PSi-CaP interface was chemically studied by HAXPES (Section 2.2.2 –xi of Chapter 2). In addition to the use of hMSCs in the regeneration of osseous tissues, they are also used to study the biocompatibility and bioactivity of materials designed to orthopaedic and dental applications [22]. Therefore, the biocompatibility of PSi/CaP bioceramics was tested by hMSCs culture.

4.2 Materials and Methods

4.2.1 Synthesis of PSi/calcium phosphate bioceramic scaffolds

In the previous chapter, two kinds of PSi were used: nPSi and mPSi, with an average pore diameter of 30 nm and 1 μm, respectively. But in this chapter, nPSi was the only substrate used for the synthesis of bioceramic cell scaffolds. Then, the label prefix 'n' was removed in this chapter leaving just PSi. PSi was synthesized using a current density of 60 mA/cm^2 for 90 s, rinsed in EtOH and dried with a nitrogen flow. Subsequent CaP depositions on PSi were carried out by CSC and CEA (Section 2.2.3 –iii and –v in Chapter 2, respectively). In CSC deposition, CaP was synthesized at different ratios of Ca/P solution volumes (V_{Ca}/V_P = 1, 1.67, 2) and under different pH of P solution (pH = 7.2, 9.7, 12.3), keeping constant the pH of Ca solution at 5.5. The standard condition was set at V_{Ca}/V_P = 1 and at pH = 7.2 of P solution.

In the case of CEA deposition, CaP was synthesized at different ratios of Ca/P current densities (I_{Ca}/I_P = 1, 1.67, 2) and Ca/P reaction times (t_{Ca}/t_P = 1, 1.67, 2). The standard condition was carried out at I_{Ca}/I_P = 1 and t_{Ca}/t_P = 1. All reactions were carried out with fresh Ca-P solutions at room temperature. A thermal post-treatment at 600 °C and 800 °C for an hour was applied in standard samples made by CSC and CEA, respectively. Additional PSi/CaP samples prepared by CEA were made for the analysis of the CaP growth using HAXPES. For the monitoring of the CaP growth: samples were prepared by reducing the standard reaction time of each cycle from 30 s to 7.5 s and other

series by increasing the reaction temperature from 20°C to 37°C and 54°C. In order to detect simultaneously Ca 1s, P 1s, and Si 1s core level signals by means of HAXPES, the t_{Ca}/t_P series were prepared by reducing the standard number of cycles from 20 to 2, with a posterior thermal treatment at 600 °C for one hour. As reference, two samples were used. One of PSi synthesized at 60 mA/cm^2 for 90 s for Si 1s core level and other of HAP for Ca 1s and P 1s core levels. HAP was synthesized on another PSi substrate at CEA standard conditions: $I_{Ca}/I_P = 1$ and $t_{Ca}/t_P = 1$, during 20 Ca/P cycles (30 s each). Both sample references were submitted to a posterior thermal treatment at 600 °C for one hour.

4.2.2 Characterization techniques

The morphology of PSi substrate and PSi/CaP composites prepared by both techniques was observed by FESEM/SEM and their chemical composition was analyzed by EDX, FTIR-SR and GA-XRD. In the case of CEA, the resistance increase of the global process during CaP electrodepostion was obtained recording the characteristic potential-time curve measured at constant current. Additionally, the quantification of the Ca/P atomic ratio of samples was performed by RBS analysis at oxygen resonant energies. In order to determine the chemical structure of PSi-CaP interface composites made by CEA were characterized by HAXPES. Finally, the biocompatibility of PSi/CaP composites obtained by both techniques was tested by hMSCs *in vitro* culture.

4.3 Results and Discussion

4.3.1 PSi/calcium-phosphate bioceramics synthesized by cyclic spin coating (CSC)

i) Physicochemical characterization

The synthesis of bioceramic composites was performed using a nanostructured PSi layer as a biocompatible structure to support the CaP deposits. PSi layers were 3.2 μm thick with an average pore diameter of 30 nm (Fig. 3-a and Fig. 3-b, respectively).

In order to study the morphology of CaP coatings obtained by CSC, a series of SEM images were acquired. Additionally, EDX analyses were carried out to identify the Ca and P containing structures. Fig. 4-a1 shows a top view of a CaP coating obtained at standard conditions, which consists of a series of solid flat-plates forming flower-like clusters with sizes between 10-20 μm. This morphology has been previously related to the brushite (BRU, $CaHPO_4 \cdot 2H_2O$) phase [23]. The corresponding EDX spectra of CaP

deposit on PSi showed a strong signal of Ca and P with some traces of Na (Fig. 4-a2). On the other hand, by means of a cross-sectional SEM image (Fig. 4-b1), a height of around 7 μm of CaP clusters is observable. The EDX spectra of the image in Fig. 1-b2 indicates that Ca and P were barely detected into the PSi structure, which suggests that PSi/CaP samples prepared by CSC are rather a bilayer structure than an integrated composite.

Higher and lower magnification top views of the CaP clusters are shown in Fig. 5-a and Fig. 5-b, respectively. The low magnification image illustrates how the clusters are distributed over the PSi surface, with typical separations of tens of microns. The high magnification image shows that solid flat-plates of CaP clusters have sizes of 3-20 μm.

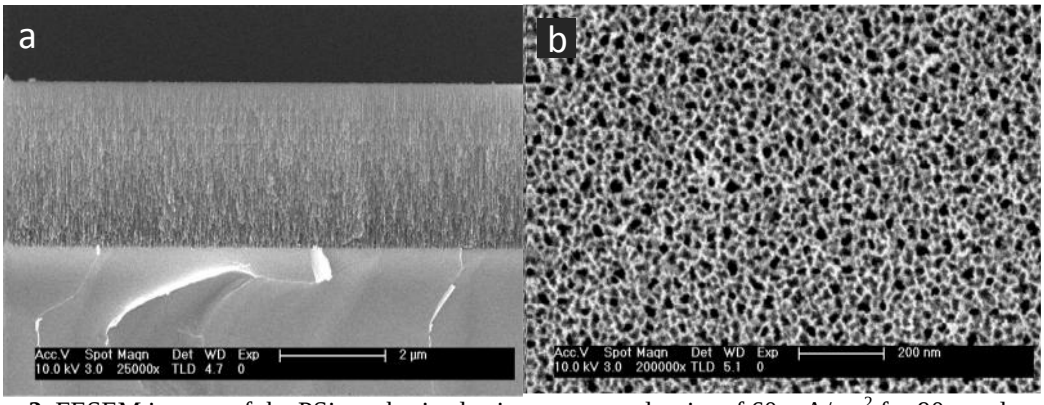

Figure 3. FESEM images of the PSi synthesized using a current density of 60 mA/cm^2 for 90 s and used in CSC: a) cross sectional and b) top view.

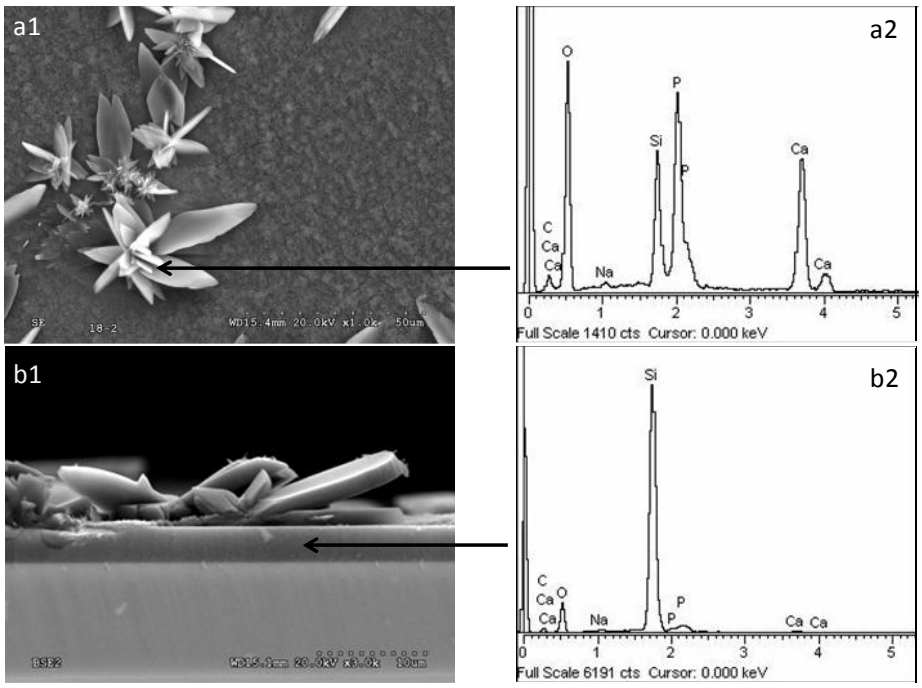

Figure 4. CaP deposit on PSi by CSC at standard conditions (V_{Ca}/V_P = 1 and pH = 7.2 of P solution): top view [SEM (a1) and EDX (a2)], and cross section view [SEM (b1) and EDX (b2)].

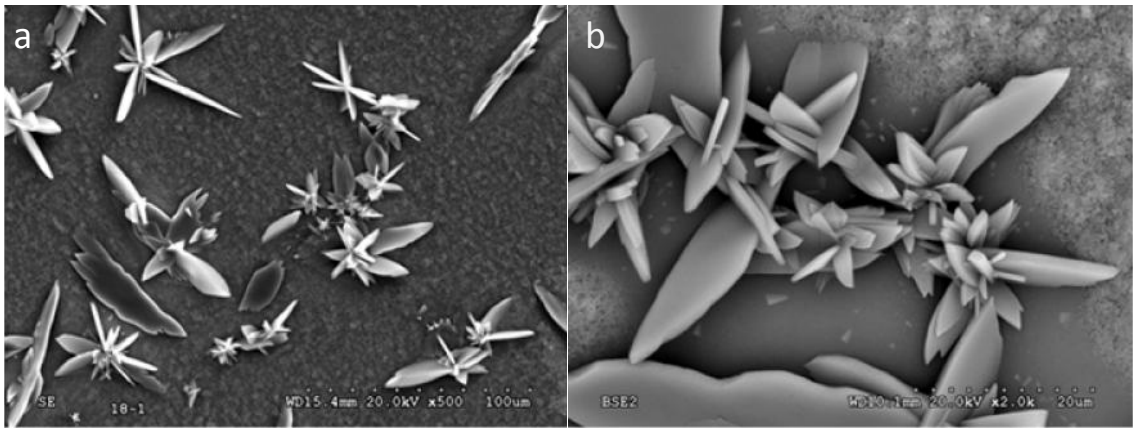

Figure 5. Zoom-out (a) and zoom-in (b) of SEM images from top view of CaP deposit on PSi by CSC at standard conditions (V_{Ca}/V_P = 1 and at pH = 7.2 of P solution).

The chemical composition of freshly synthesized PSi, and after CaP deposition was evaluated by SR-FTIR spectroscopy (Fig. 6). In Fig. 6-a, full spectra of both samples are shown. The PSi spectrum shows relatively strong interference fringes, which are typical of PSi layers of similar thickness [24,25]. In the case of the PSi/CaP spectrum, the fringes fade because of the infrared absorption and increased surface roughness associated to the CaP surface clusters. Fig. 6-b shows a zoom-in of both spectra to allow a better identification of functional groups of samples. Characteristic Si-H bonds of nanostructured PSi recently synthesized are identified at 2116, 906, 661 and 624 cm^{-1} [24,26]. In the case of PSi/CaP sample, absorptions in the range of 1190-976 cm^{-1} are identified, which are related to PO_4 ν_3 in CaP structures [27,28], as well as the signal at 633 cm^{-1} of PO_4 ν_4 [28]. Additionally, the absorption at 873 cm^{-1} corresponding to CO_3 ν_3 is identified [28]. This carbonate peak is probably originated from the reaction of hydroxyl ions with carbon dioxide ($CO_2 + 2OH^- \leftrightarrow CO_3^{-2} + H_2O$), which get integrated into the HAP structure [27]. An additional shoulder at around 1600 cm^{-1} is attributed to the bending mode of O-H group from water [23].

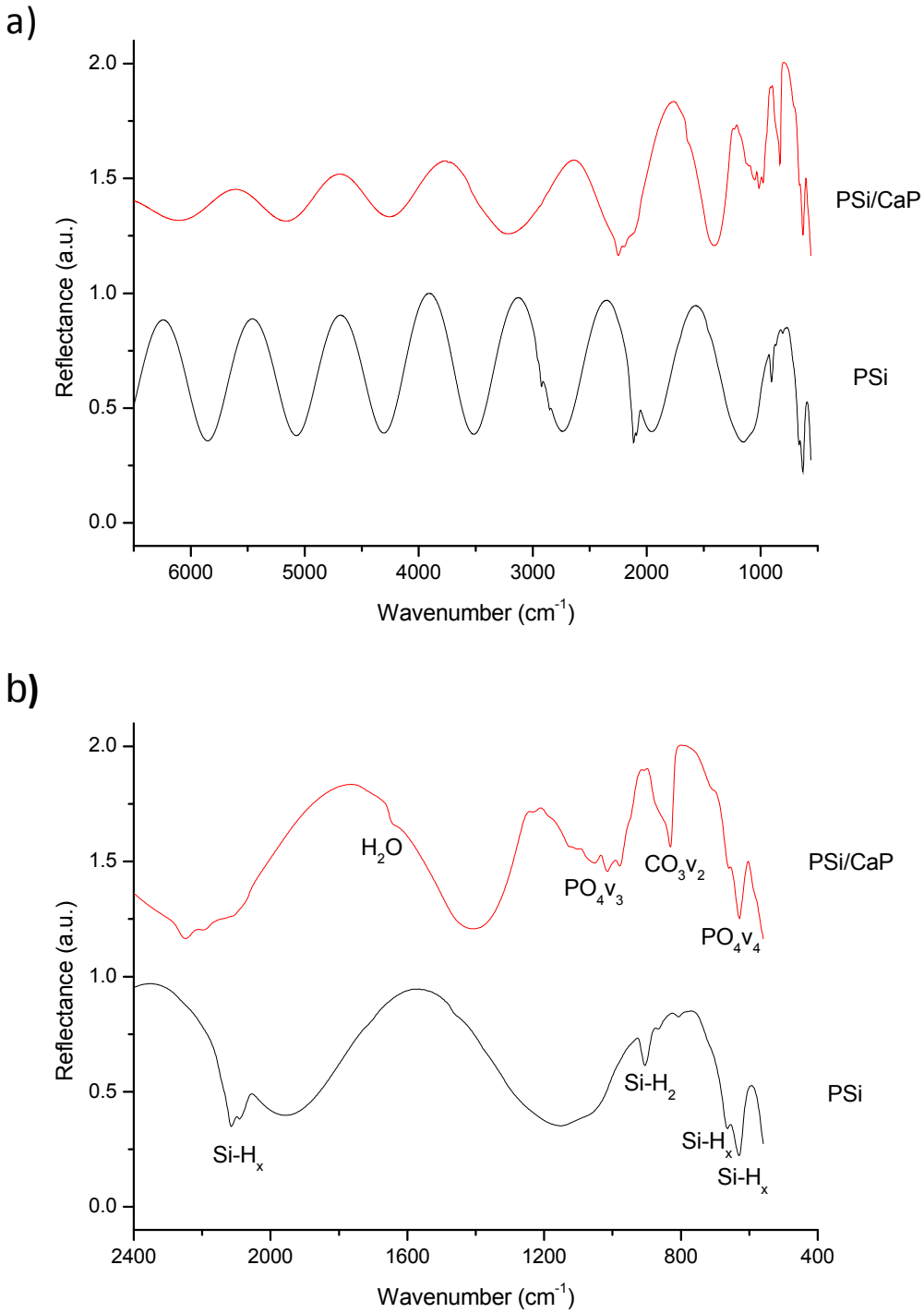

Figure 6. SR-FTIR spectra of PSi and PSi/CaP obtained by CSC at standard conditions (V_{Ca}/V_P = 1 and at pH = 7.2 of P solution): a) full range spectra and b) zoom-in of spectra.

X-Ray diffraction studies were performed in order to determine the crystalline structure of the CaP deposits. Fig. 7 shows a GA-XRD diagram of a PSi substrate. A strong intensity peak at 55.7° is detected, which corresponds to Si after partial amorphization due to transformation into PSi [29]. Fig. 8-a shows a GA-XRD diagrams of the samples obtained by the CSC technique at different ratios of Ca/P solution volume (V_{Ca}/V_P = 1, 1.67, 2). This series of experiments revealed an evident crystallization in

BRU phase [30], which is consistent with the previously observed morphologies (SEM) and identified chemical bonds (SR-FTIR). However, at the highest V_{Ca}/V_P ratio a slight trace of HAP appears. The chemical formation of this CaP coating is in agreement with the route for the chemical synthesis of BRU. Firstly, the PO_4^{-3} is oxidized to HPO_4^{-2} since the P solution has a neutral pH [31], and then reacts with Ca^{+2} based on the next equation [32]:

$$Ca^{+2} + HPO_4^{-2} + 2H_2O \rightarrow CaHPO_4 \cdot 2H_2O \qquad \text{(Eq. 1)}$$

Since the basic environment favors HAP formation [33], we proceeded with a series of CaP syntheses by CSC using the standard ratio ($V_{Ca}/V_P = 1$) at different pH of the P solution (pH = 7.2, 9.7, 12.3) (Fig. 3). In GA-XRD diagrams of Fig. 8-b it is possible to observe a gradual increase of the peak related to HAP for increasing pH, always in addition to the BRU structure. The competing reaction for HAP formation is shown in the next equation [32]:

$$10Ca^{+2} + 6PO_4^{-3} + 2OH^- \rightarrow Ca_{10}(PO_4)_6(OH)_2 \qquad \text{(Eq. 2)}$$

However, although there are peaks corresponding to HAP, they do not indicate the formation of a fully dominant HAP, as derived from some with relevant missing peaks (i.e. 2θ= 31.8, 32.2, 32.9, 34.1 [34]).

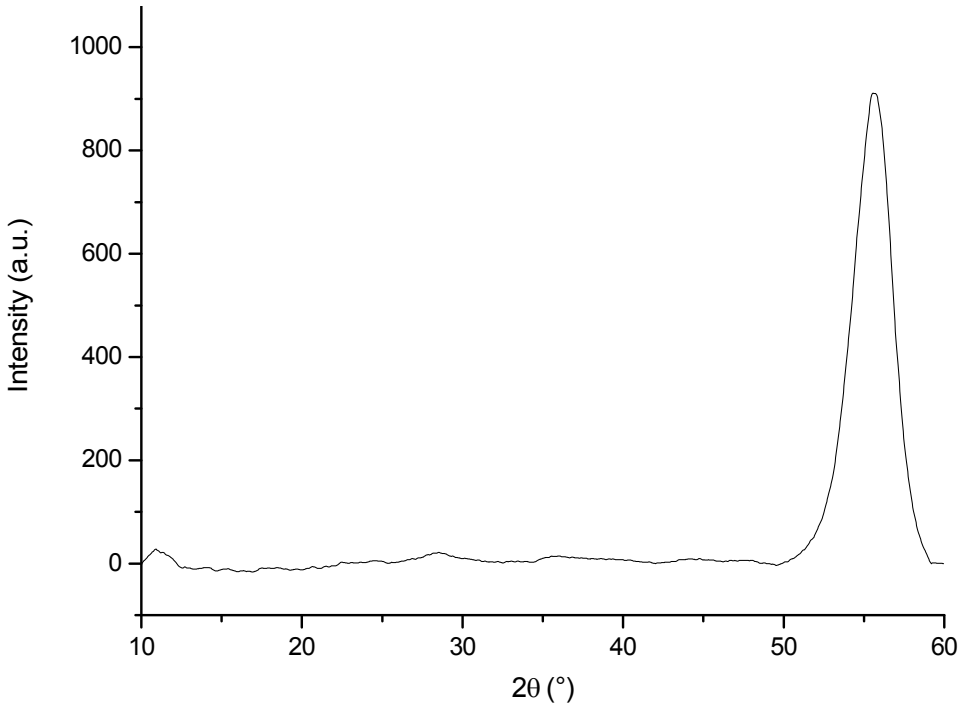

Figure 7. GA-XRD diagram of PSi substrate synthesized at 60 mA/cm^2 for 90 s.

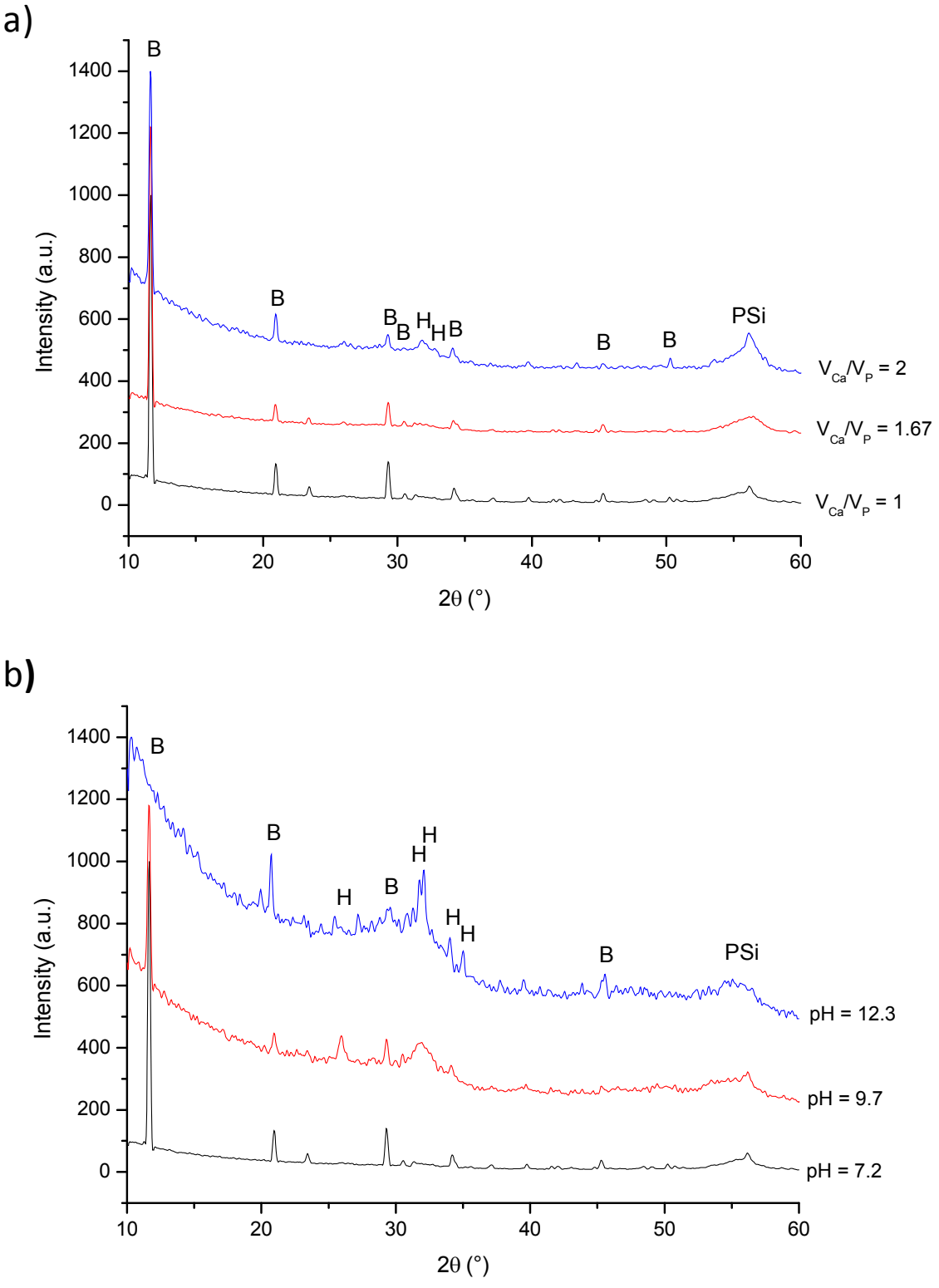

Figure 8. GA-XRD diagrams of PSi/CaP samples obtained by the CSC technique: a) at different ratios of Ca/P volume (V_{Ca}/V_P = 1, 1.67, 2) at neutral pH, and b) at different pH of P solution (pH = 7.2, 9.7, 12.3) at V_{Ca}/V_P = 1. B = Brushite, H = Hydroxyapatite.

Basic solutions are usually used to dissolve PSi [35] although the degradation rate of PSi remains slow. In the case of basic CSC solutions, from the kinetic point of view, the degradation is supposed to be negligible with respect to the fast CaP deposition rate. Furthermore, the CSC technique works mostly on the top surface of the PSi as was demonstrated by EDX analysis, which only detected Ca and P traces into the PSi layer, not affecting the structural configuration of PSi (SEM and EDX analysis of Fig. 4).

The thermal stability of standard PSi/CaP (V_{Ca}/V_P = 1 and at a neutral pH) was analyzed after a thermal treatment at 600 °C for one hour (XRD diagrams in Fig. 9). BRU was not stable at high temperatures. It suffered the typical thermally induced transformation of an orthophosphate into a pyrophosphate according to the following reactions [36]:

$$2CaHPO_4 \cdot 2H_2O \rightarrow CaHPO_4 + 4H_2O \quad \text{(Eq. 3)}$$

$$2CaHPO_4 \rightarrow Ca_2P_2O_7 + H_2O \quad \text{(Eq. 4)}$$

Eq. 3 represents the dehydration of BRU turning it into monotite (MON, $CaHPO_4$), and Eq. 4 the transformation of MON into calcium pyrophosphate (PYR, $Ca_2P_2O_7$), which occurs above 500 °C.

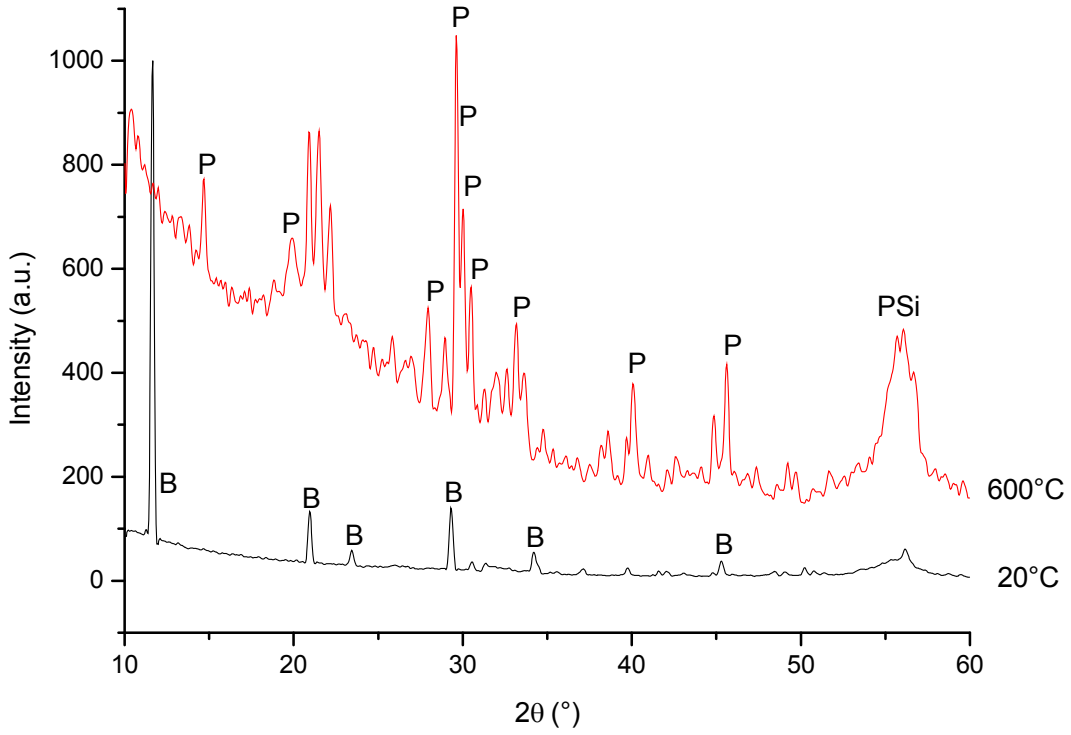

Figure 9. GA-XRD diagram of standard PSi/CaP sample obtained by the CSC at standard conditions (V_{Ca}/V_P = 1 and pH = 7.2 of P solution): at room temperature, and after post-thermal treatment at 600ºC.

ii) Biocompatibility characterization

In order to evaluate the biocompatibility of PSi/CaP samples, cells were seeded onto their surfaces. Fluorescence microscopy was used to characterize the attachment and morphology of hMSCs onto PSi and PSi/CaP composite prepared by CSC at standard conditions (Fig. 10). This composite was selected as reference to test the biocompatibility because it was the sample within a dominant BRU structure. As a control, cells were seeded on the PSi surface, where they were allowed to grow and attach for 24 h. The cells cultured on PSi showed a normal morphological appearance (Fig. 10-a1 and 10-a2) and an active mitosis (see arrows, Fig. 10-a1 and 10-a2). This behavior is in contrast with the semispherical form that L132 cells adopted on PSi after 24 h of culture (Section 3.3.4 of Chapter 3). In any case, it is convenient to remind that those PSi samples had been previously chemically oxidized and that a different cell line had been used. In fact, a drastic change in surface chemistry [37], and the culture of an alternative cell line [38] can justify variations in the expected cell adhesion response.

Returning to the biocompatibility study of bioceramics by hMSCs, in the case of the cells cultured on the PSi/CaP sample (Fig. 10-b1 and 10-b2), they showed a striated actin cytoskeleton with long filopodia acquiring a shape conditioned by the solid flat BRU clusters. This elongated cytoskeleton could be interpreted in terms of a migratory state of cells on clusters. This is probably due to a state of minimum energy in cells adhesion and/or to an influence of the extracellular ionic concentration gradient.

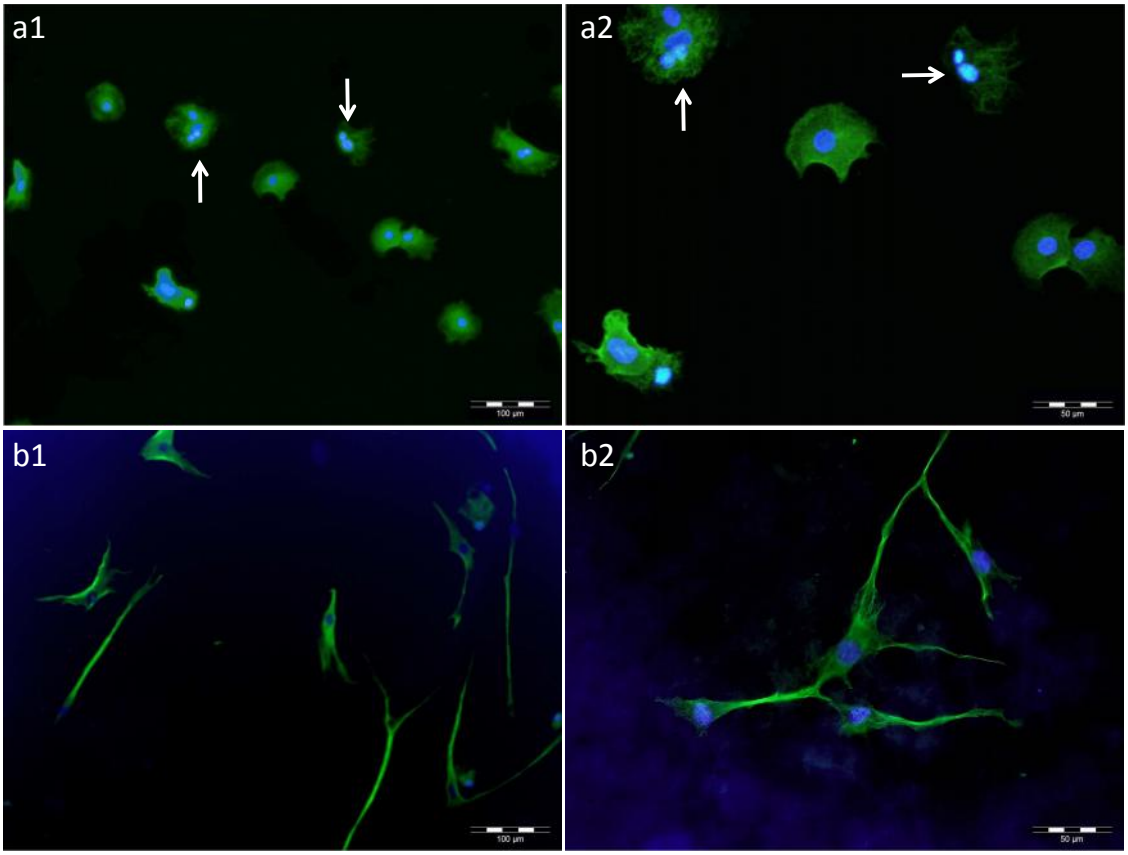

Figure 10. Fluorescence microscopy images of hMSCs cultured on PSi (a1 and a2) and on PSi/CaP composite prepared by CSC at standard conditions (V_{Ca}/V_P = 1 and pH = 7.2 of P solution) (b1-b2) showing actin cytoskeleton stained by phalloidin-Alexa488 and cell nuclei stained by DAPI.

Characterization results showed that CSC is a viable technique to synthesize PSi/CaP bioceramics. The CaP particles deposited on PSi consisted of a series of solid flat-plates with sizes of 10-20 μm. The BRU phase of CaP was strongly favored and mostly deposited on PSi surface, resulting in a composite of two well defined layers.

4.3.2 PSi/calcium-phosphate bioceramics synthesized by cyclic electrochemical activation (CEA)

i) Physicochemical characterization

CEA was the second cyclic technique used to deposit CaP on PSi. The same independent Ca and P stem-solutions used in CSC (neutral pH, room temperature) were utilized. As in the case of CSC, the morphology of the synthesized CaP coating was observed by SEM and the identification of Ca and P elements was performed by EDX

analysis. In the top view image of Fig. 11-a1, a CaP coating formed by CEA is shown. It consists of agglomerates of circa 20 μm size randomly and heterogeneously distributed on PSi. Besides, a strong signal of Ca and P atoms in its respective EDX spectra is indicated (Fig. 11-a2). In the cross-section image of Fig. 11-b1 CaP agglomerates formed by CEA are shown. A height of approximately 10 μm with respect to the PSi surface is observable. Unlike in PSi/CaP prepared by CSC, for the PSi/CaP synthesized by CEA, the Ca and P were intensely detected by EDX, even into the PSi layer, thus indicating a better integration of both compounds (Fig. 11-b2).

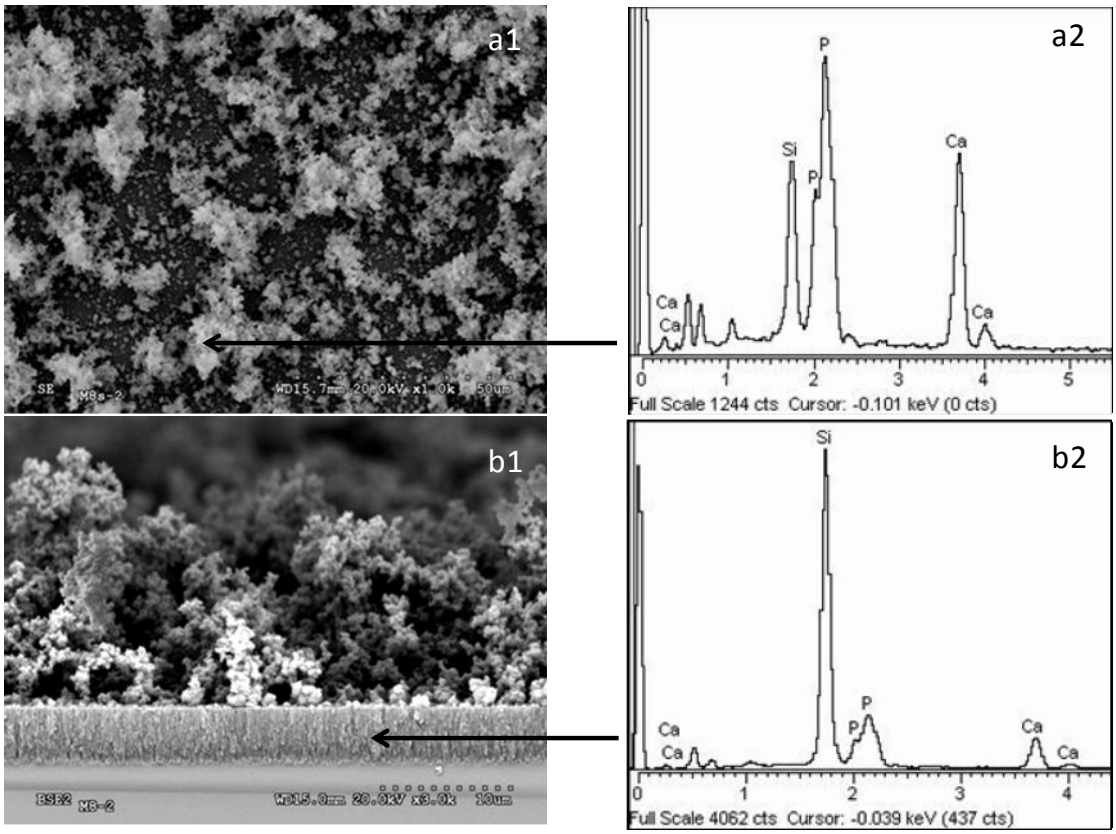

Figure 11. CaP deposit on PSi by CEA at standard conditions ($I_{Ca}/I_P = 1$ and $t_{Ca}/t_P = 1$): top view [SEM (a1) and EDX (a2)], and cross section view [SEM (b1) and EDX (b2)].

Higher magnification images of CaP clusters are shown in Fig. 12. Fig. 12-a shows that the CaP particles are spherical, around 300 nm in diameter and Fig. 12-b illustrates how the CaP particles are well-agglomerated in clusters. Morphologically, the CaP particles are similar to others synthesized previously [39], although this particular shape was obtained in an aqueous precipitation method at pH = 9 following a sintering step at 950 ºC.

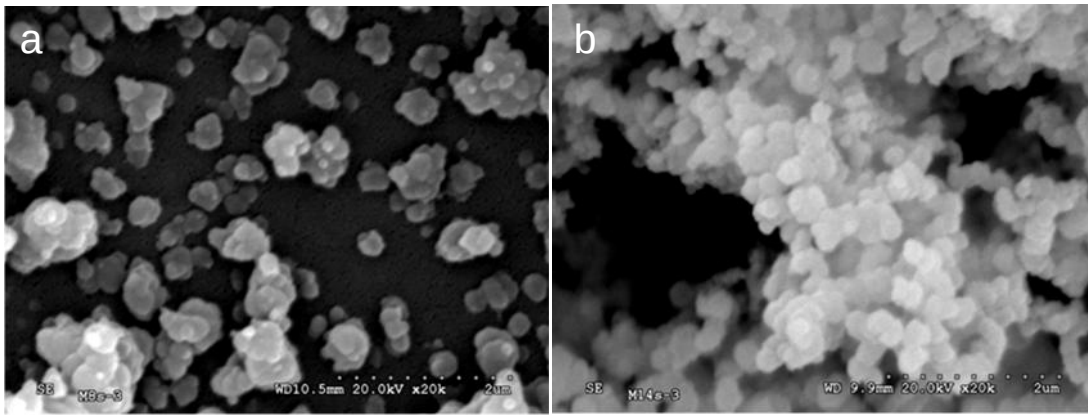

Figure 12. Zoom-in of CaP particles synthesized by CEA at standard conditions ($I_{Ca}/I_P = 1$ and $t_{Ca}/t_P = 1$): a) on PSi surface, and b) into agglomerates.

A characteristic of CEA is that CaP deposition on PSi can be monitored by recording the applied potential during the electrodeposition carried out at a constant current density. With increasing reaction time, or number of cycles in our case, cluster density and size increase as illustrated in the SEM images corresponding to the 5th and 20th cycles (Fig. 13-a1 and 13-a2, respectively). The required potential also increases with the number of cycles, as experimental *V* vs *t* curves of Ca and P deposition at the 5th and 20th cycle show (Fig. 13-b1 and 13-b2, respectively).

In order to provide a model for the CaP deposition we have evaluated the electrical parameters in the cell. The electrochemical system can be approximated to a model consisting of a resistance and a capacitor connected in series. For a resistor-capacitor circuit under direct current, the potential is given by [31]:

$$V = iR + \frac{i}{C}\int dt \qquad \text{(Eq. 5)}$$

where *V* is the applied potential; *i*, the current; *R*, the resistance; *C*, the capacitance and *t* is time. The asymptotic saturation of *V* to a constant value (Fig. 13-b1 and 13-b2) suggests that the 1/*C* term in (Eq. 5) is negligible, which can be attributed to the high capacitance associated with the large internal surface of PSi [24,40-42].

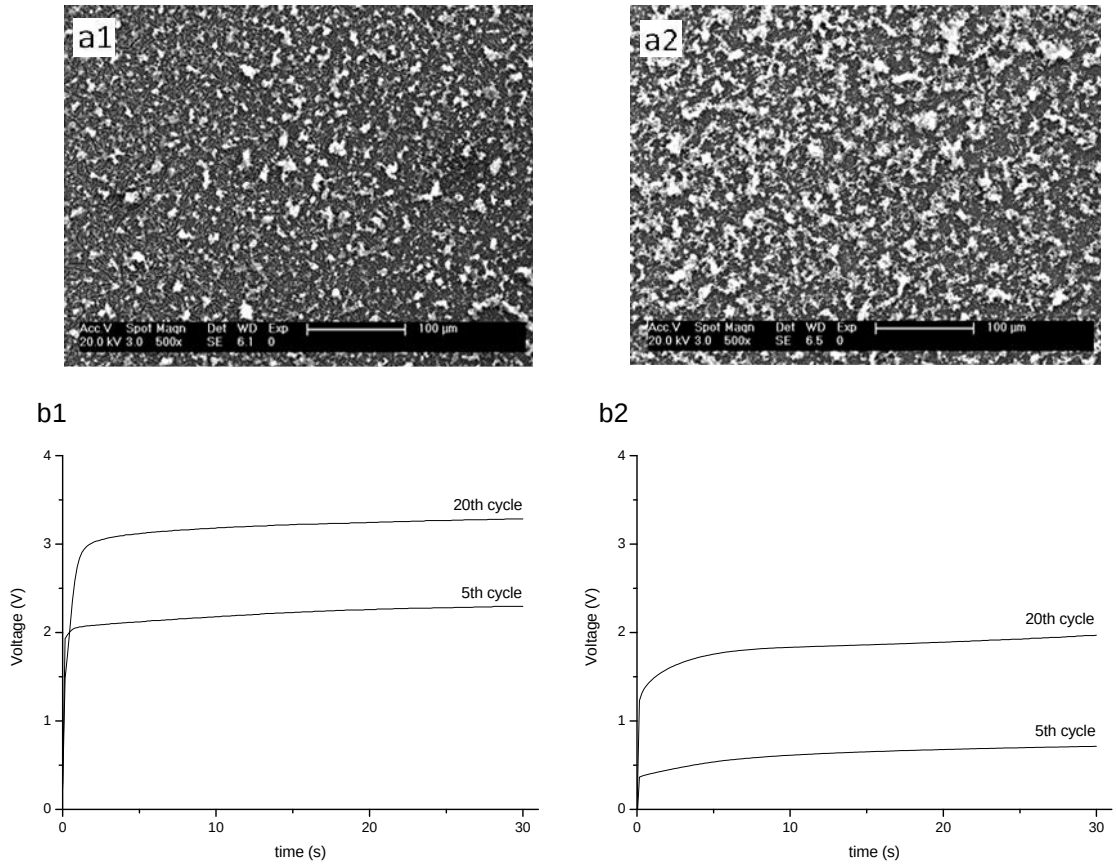

Figure 13. SEM images of CaP deposited on PSi prepared under standard conditions ($I_{Ca}/I_P = 1$ and $t_{Ca}/t_P = 1$): a1) at 5th cycle, a2) at 20th cycle; and *V* vs *t* curves for the 5th and 20th cycles: b1) corresponding to Ca solution (cathodic current), and b2) corresponding to P solution (anodic current).

The constant potential *V* for a fixed electrodeposition current (1 mA/cm^2, cathodic current for Ca solution and anodic current for P solution), allows the determination of an effective resistance value for each electrodeposition step by applying Ohm's law. The plot in Fig. 14 shows that this effective resistance increases linearly with the number of cycles, suggesting that CaP growth in PSi is also linear with the number of cycles. However, it is possible that the resistance increase has some contribution from oxide formation in the PSi matrix. As a consequence the voltage reached during the process is 3.3 V in Ca solution and 2 V in P solution [43]. Different resistance plots for different conditions of CaP deposition were obtained.

The SEM image of Fig. 15-a shows a lower density of CaP particles obtained with 20 cycles and 7.5 s per immersion cycle in comparison with the standard conditions of 30 s per cycle (Fig. 13-a2). The lower CaP deposition density is supported by the lower slope in its corresponding resistance curves of Ca and P deposition (Fig. 15-b). Fig. 16 shows

the resistance increment in each cycle of CaP electrodeposition at standard conditions but at higher reaction temperatures: 37°C and 54°C (Fig. 16-a and Fig. 16-b, respectively).

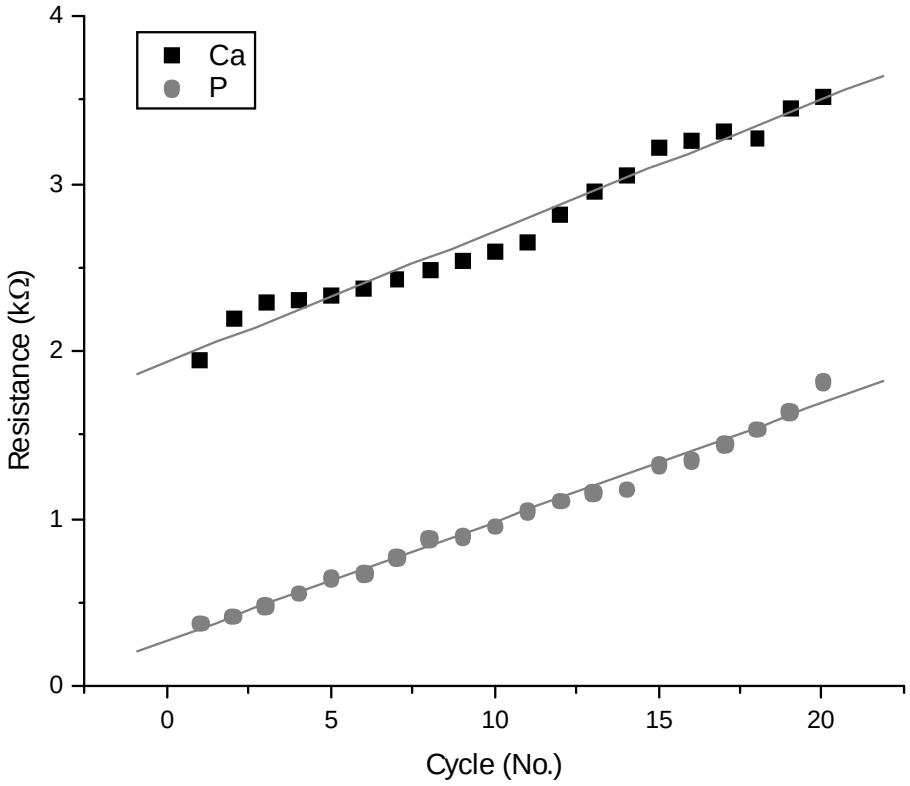

Figure 14. Resistance increment per cycle for the independent Ca and P solutions. CaP electrodeposition carried out at standard conditions ($I_{Ca}/I_P = 1$ and $t_{Ca}/t_P = 1$) and room temperature.

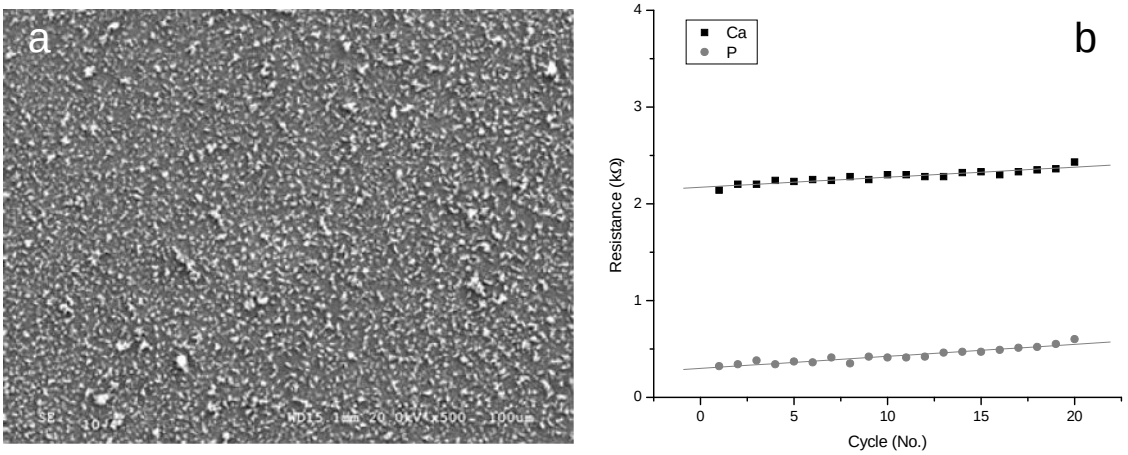

Figure 15. CaP deposited on PSi at standard conditions ($I_{Ca}/I_P = 1$ and $t_{Ca}/t_P = 1$) but reducing the time per cycle to 7.5 s: a) SEM image, and b) resistance increase.

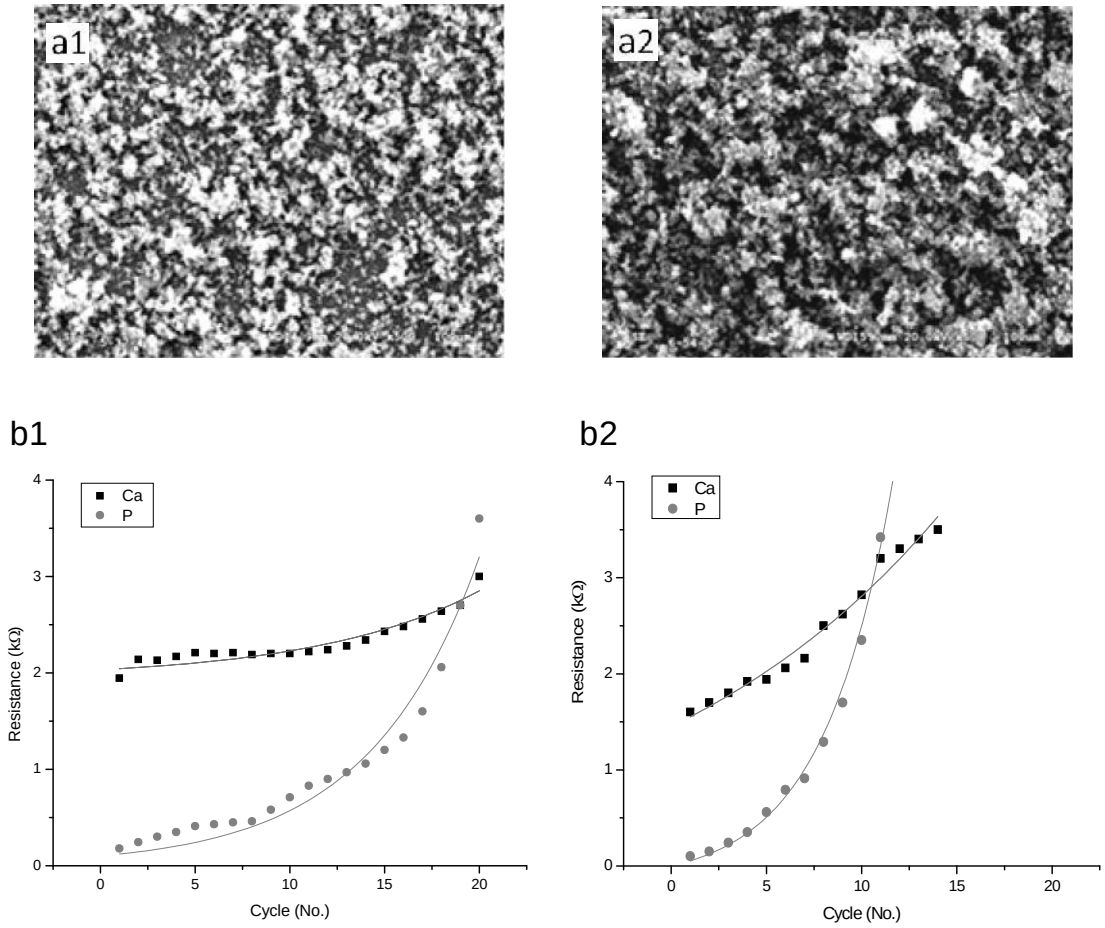

Figure 16. SEM images of CaP on PSi deposited at standard conditions (I_{Ca}/I_P = 1 and t_{Ca}/t_P = 1) increasing the reaction temperature to: a1) 37°C, a2) 54°C; and their respective resistance increment curves: b1) 37°C, b2) 54°C.

The equations of curves fitting the experimental data of the resistance increase as a function of CaP deposition conditions are reported in Table 1. These curves generated equations with coefficient of determination values (r^2) very close to 1. According to these experimental and fitting curves, the CaP deposition increases with the reaction temperature owing to enhanced ion supply by diffusional transport and decreased electrolyte viscosity [44]. Therefore, the resistance of the system is also increased. In fact, the CaP deposition at 54 °C (Fig. 16-b2) was such that PSi surface was saturated at the 14th cycle, boosting up the applied potential. Previous studies (Ban et al. [45]) have also reported that, in the electrochemical synthesis of CaP in this temperature range, the diffusion process is a rate-determining step, which is increased in proportion to temperature.

Table 1. equations of the curves fitting the resistance increment during CaP electrodeposition in different conditions.

Experiment	Ca deposition Equation	P deposition Equation
Standard	$y = 0.07838x + 1.93247;$	$y = 0.07069x + 0.27274;$
	$r^2 = 0.98629$	$r^2 = 0.99485$
7.5 s per cycle	$y = 0.01037x + 2.17163;$	$y = 0.01239x + 0.29989;$
	$r^2 = 0.93661$	$r^2 = 0.95224$
37 °C	$y = 0.01296e^{(x/4.80531)} + 2.10622;$	$y = 0.10296e^{(x/5.80584)};$
	$r^2 = 0.95135$	$r^2 = 0.9613$
54 °C	$y = 0.19407e^{(x/5.79477)} + 1.6;$	$y = 0.13347e^{(x/3.43569)};$
	$r^2 = 0.93737$	$r^2 = 0.99652$

x = Number of cycle (-)
y = Resistance (kΩ)

Moving on to the chemical study of the PSi/CaP composites, SR-FTIR analysis was carried out on the PSi before and after standard CaP deposition by CEA (Fig. 17). In Fig. 17-a, full spectra of PSi and PSi/CaP samples are shown. The PSi spectrum shows the typical interference fringes when PSi is formed as a thin layer [24,25]. As in the case of the spectrum of PSi/CaP obtained by CSC, the spectrum of PSi/CaP synthesized by CEA also shows faded fringes due to infrared absorption by CaP clusters, but in this case the fading is more pronounced. Fig. 17-b shows a zoom-in to both spectra. The PSi spectrum shows the characteristic Si-H bonds when PSi is recently synthesized: 2116, 906, 661 and 624 cm^{-1} [24,26]. In the case of PSi/CaP spectrum, PO_4 ν_3 peaks were identified at 1091, 1042, 962 cm^{-1}, which are related to CaP phases [27,28], besides the signal at 602 cm^{-1} corresponding to PO_4 ν_4 [28]. Moreover, an absorption around 1455 cm^{-1} corresponding to CO_3 ν_3 was also identified [28].

Diffraction studies were performed in order to extract information relative to the crystalline structure of the CaP samples deposited by CEA (Fig. 18). Fig. 18-a corresponds to a series of experiments at different current density ratios (I_{Ca}/I_P = 1, 1.67, 2) and Fig. 18-b to different reaction time ratios (t_{Ca}/t_P = 1, 1.67, 2). The parameters of current density and reaction time were selected with relation to the ion mobilities [31]. In this way, the I_{Ca}/I_P and t_{Ca}/t_P series in CEA are equivalent to Ca and P condition variations generated by V_{Ca}/V_P in CSC.

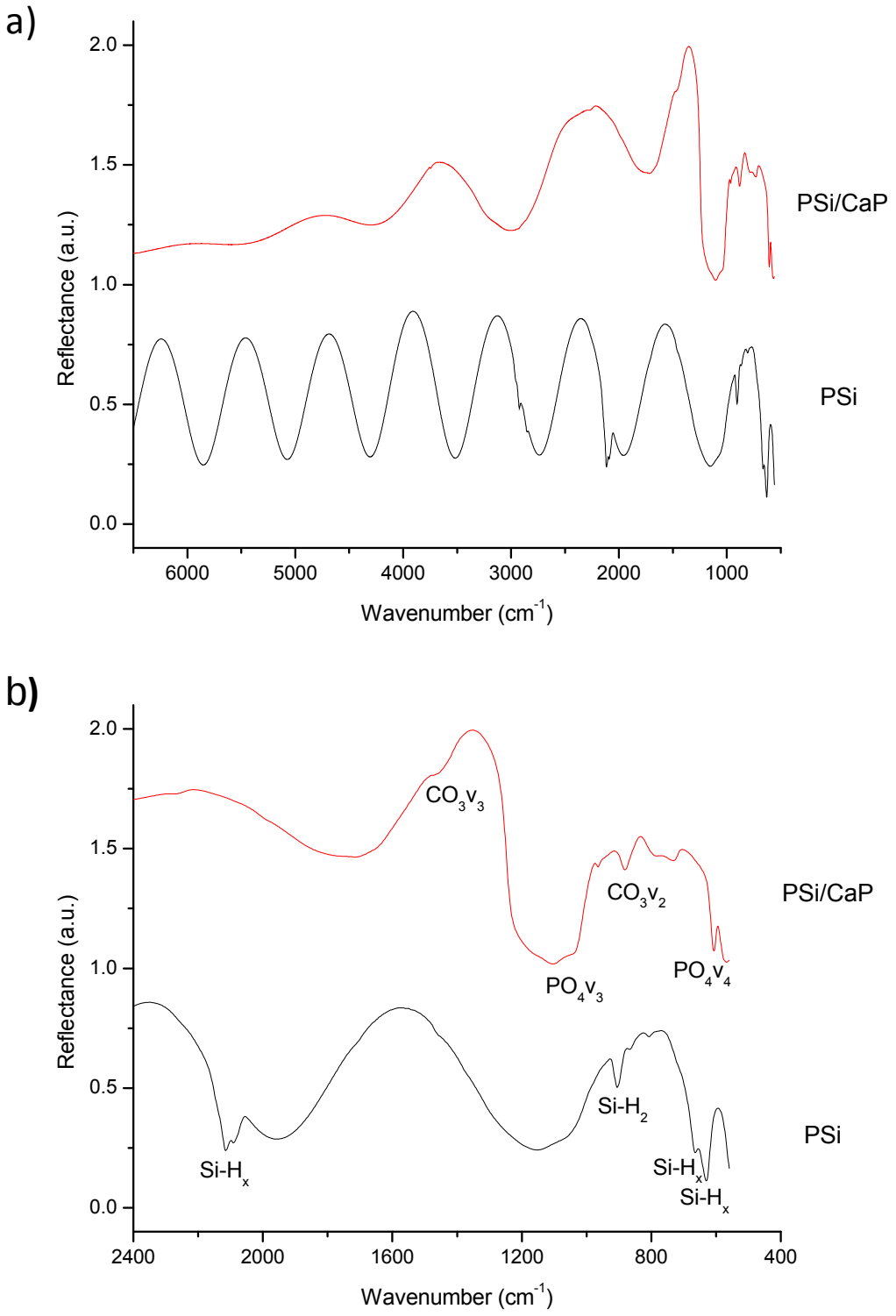

Figure 17. FTIR-SR spectra of PSi and PSi/CaP obtained by CEA at standard conditions ($I_{Ca}/I_P = 1$ and $t_{Ca}/t_P = 1$): a) full spectra and b) zoom-in of spectra.

According to GA-XRD diagrams in Fig. 18-a, in the experiment of $I_{Ca}/I_P = 1$, main 2θ values corresponding to HAP [33,34,46] are well identified with a trace of MON. On

the other hand, for the cases of I_{Ca}/I_P = 1.67 and 2, traces of MON and BRU are notorious within a dominant HAP structure too. In the case of GA-XRD diagrams in Fig. 18-b, the main phases identified in the difractograms are the same as those found in the CSC experiments. The more important difference is the lower crystallinity of HAP for t_{Ca}/t_P = 1.67 and 2. The diffractogram corresponding to sample prepared at t_{Ca}/t_P = 1.67 indicates a relatively strong presence of BRU in HAP and the corresponding to t_{Ca}/t_P = 2 shows a solid solution of MON-BRU traces in HAP. The relative increase of these phases creates a competitive environment for crystal growth that could not only affect to the quantity of HAP formed but also to the quality of the HAP crystals formed, as suggested by the increase of the width at half maximum of the peaks attributed to HAP.

From the evidences provided by the GA-XRD study it is possible to propose an electrochemical mechanism for the growth of CaP on/in PSi. The process of cyclic activation of Ca and P deposition onto PSi, taking into account the respective polarity of the independent Ca and P solutions, is explained as a series of reduction-oxidation reactions. The presence of MON and BRU traces in HAP suggests a sequence of electrochemical reactions. At pH = 7.2 the phosphate ion formed is the monohydrated HPO_4^{-2} [31] and since the reduction potential of Ca^{+2} ions to metallic *Ca* is not yet reached (-2.8 V) [31] until the 10th cycle, during the first 10 cycles there is only a chemical formation of MON and BRU given by [47,48]:

$$Ca^{+2} + HPO_4^{-2} \rightarrow CaHPO_4 \qquad \text{(Eq. 6)}$$

$$Ca^{+2} + HPO_4^{-2} + 2H_2O \rightarrow CaHPO_4 \cdot 2H_2O \qquad \text{(Eq. 7)}$$

That means that, at the beginning, each respective current density in each solution works only as a force that moves ions to PSi enhancing the chemical reaction on its surface. However, after the 10th cycle, in Ca solution there is a reduction from Ca^{+2} ion to metallic *Ca* as observed previously [31,49]:

$$Ca^{+2} + 2e^- \rightarrow Ca \qquad \text{(Eq. 8)}$$

Then, the metallic *Ca* is oxidized to MON and BRU in the P solution as already suggested [47,48], together with reactions of Eq. 6 and 7:

$$Ca + HPO_4^{-2} \rightarrow CaHPO_4 + 2e^- \qquad \text{(Eq. 9)}$$

$$Ca^{+2} + HPO_4^{-2} + 2H_2O \rightarrow CaHPO_4 \cdot 2H_2O + 2e^- \quad \text{(Eq. 10)}$$

OH^- ions are dominantly produced from reduction of water, although OH^- can also plausibly derive from ethanol dissolution and dissolved oxygen [50]:

$$2H_2O + 2e^- \rightarrow H_2 + 2OH^- \quad \text{(Eq. 11)}$$

$$O_2 + 2H_2O + 4e^- \rightarrow 4OH^- \quad \text{(Eq. 12)}$$

Thus, the MON, BRU and metallic Ca react with OH^- ions resulting in the formation of HAP [48,50-52]:

$$10CaHPO_4 + 12OH^- \rightarrow Ca_{10}(PO_4)_6(OH)_2 + 4PO_4^{-3} + 10H_2O \quad \text{(Eq. 13)}$$

$$10CaHPO_4 \cdot 2H_2O + 12OH^- \rightarrow Ca_{10}(PO_4)_6(OH)_2 + 4PO_4^{-3} + 20H_2O \quad \text{(Eq. 14)}$$

$$10Ca + 6PO_4^{-3} + 2OH^- \rightarrow Ca_{10}(PO_4)_6(OH)_2 + 20e^- \quad \text{(Eq. 15)}$$

Due to the pH of the P solution, the PO_4^{-3} reacts with water to produce HPO_4^{-2}[53] and the process restarts again in reactions of Eq. 6,7,9 and/or 10. The MON and BRU traces found when I_{Ca}/I_P and t_{Ca}/t_P ratios are increased may be attributed to the generation of an excess of Ca^{+2} and metallic Ca, and the neutral pH of P solution. The excess of Ca^{+2} and metallic Ca are transformed into MON and BRU due to the neutral pH. But at the same time due to this neutral pH, some MON and BRU formed cannot react to produce HAP because there are not enough PO_4^{-3} and OH^- ions to react. In fact, it has been reported that the growth kinetic coefficients of HAP are smaller than those of BRU by 18 orders of magnitude at pH 6.5 [30]. It is patent that basic conditions are more favorable for HAP formation [33,36,54]. That is why unlike in the CSC method, which affects mainly the top surface of PSi, basic pH could be not used. In fact, the CEA technique is not compatible with working at basic conditions because the technique implies ion permeability in the PSi layer. These layers risk thus getting dissolved when immersed into basic solutions. This phenomenon is amplified in view of the long time of PSi immersion in the basic solution since the overall growth process is relatively slow.

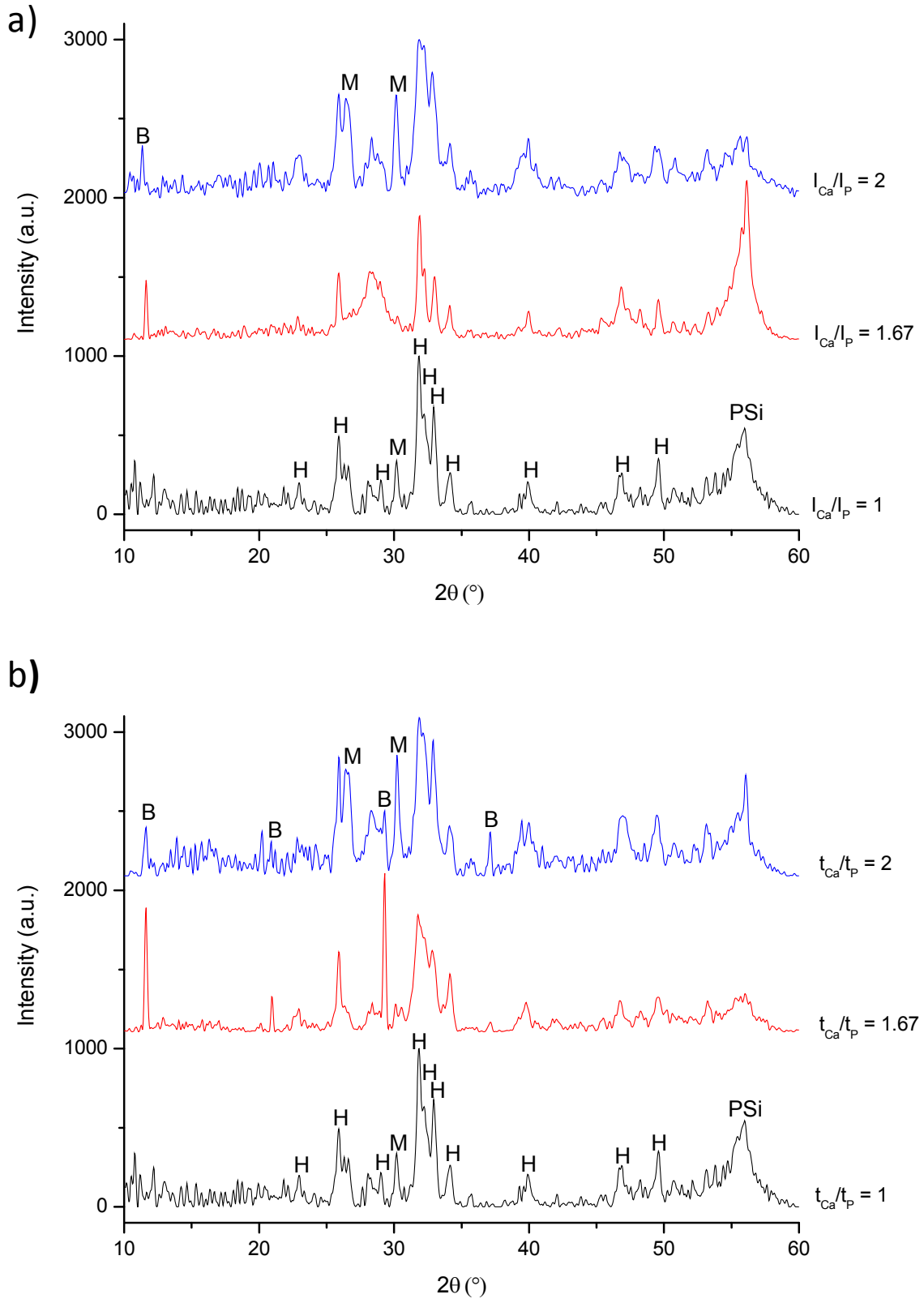

Figure 18. GA-XRD diagrams at different ratios of: a) CaP deposited with I_{Ca}/I_P = 1, 1.67, 2 for a t_{Ca}/t_P =1, and b) CaP deposited with t_{Ca}/t_P = 1, 1.67, 2 for a I_{Ca}/I_P = 1. H = Hydroxyapatite, M = Monotite, B = Brushite.

The stability of the synthesized HAP at room temperature was confirmed by the thermal post-treatment at 800 °C made for an hour (Fig. 19). The GA-XRD diffractogram of the annealed sample presents the same phases identified in the diffractogram obtained at room temperature. However, the annealing activates the crystalline structure as derived from the better definition of the diffractogram peaks. Besides, the 800°C diffractogram presents other two main differences, the monotite peak at 30.2 is considerably reduced and the HAP peak at 32.2 shows an enhanced definition.

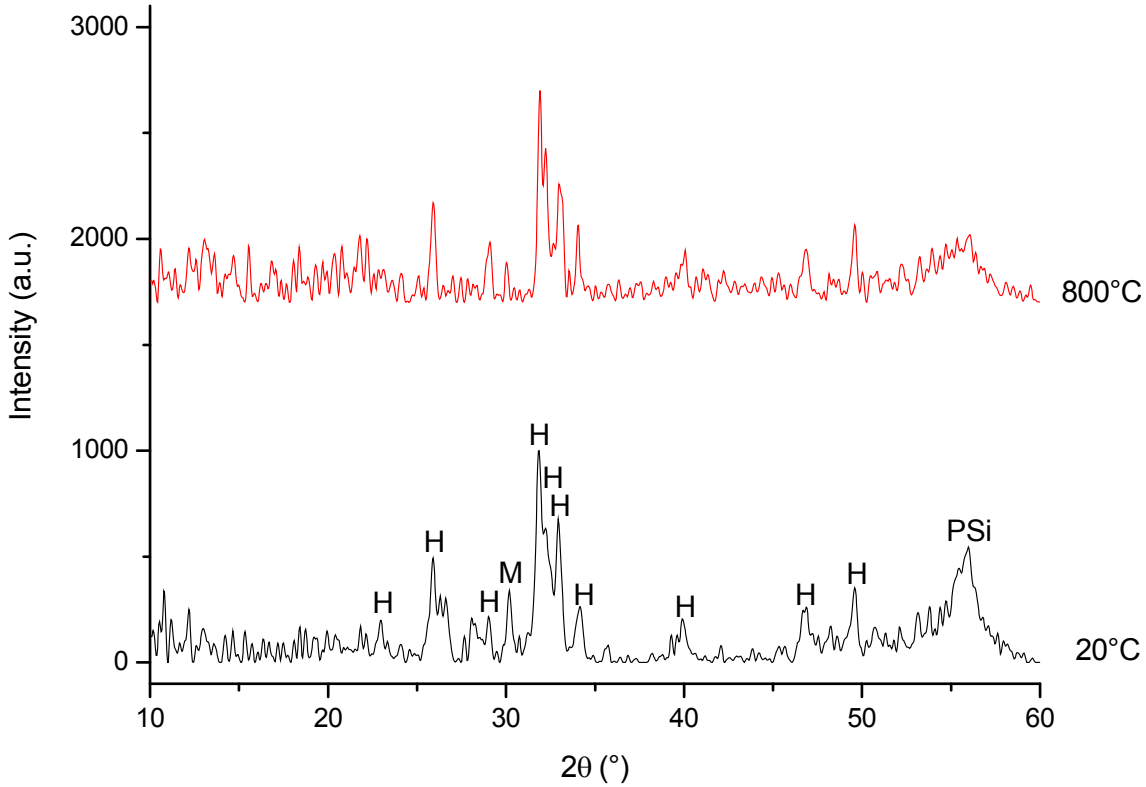

Figure 19. GA-XRD diagrams of CaP deposits obtained at room temperature and after a thermal post-treatment at 800 °C. Sample prepared at standard conditions ($I_{Ca}/I_P = 1$ and $t_{Ca}/t_P = 1$). H = Hydroxyapatite, M = Monotite.

As the evaluation of the Ca/P atomic ratio in CaP has become a clue indicator of the stability, bioresorbability and bioactivity of HAP films, analysis by RBS has been made on PSi/CaP composites synthesized by CEA where HAP was previously identified by XRD diagrams. Fig. 20-a shows a representative Rutherford backscattering spectrum obtained from a sample prepared at standard conditions ($I_{Ca}/I_P = 1$ and $t_{Ca}/t_P = 1$) and its respective simulation using the RBS simulation code SIMNRA [55].

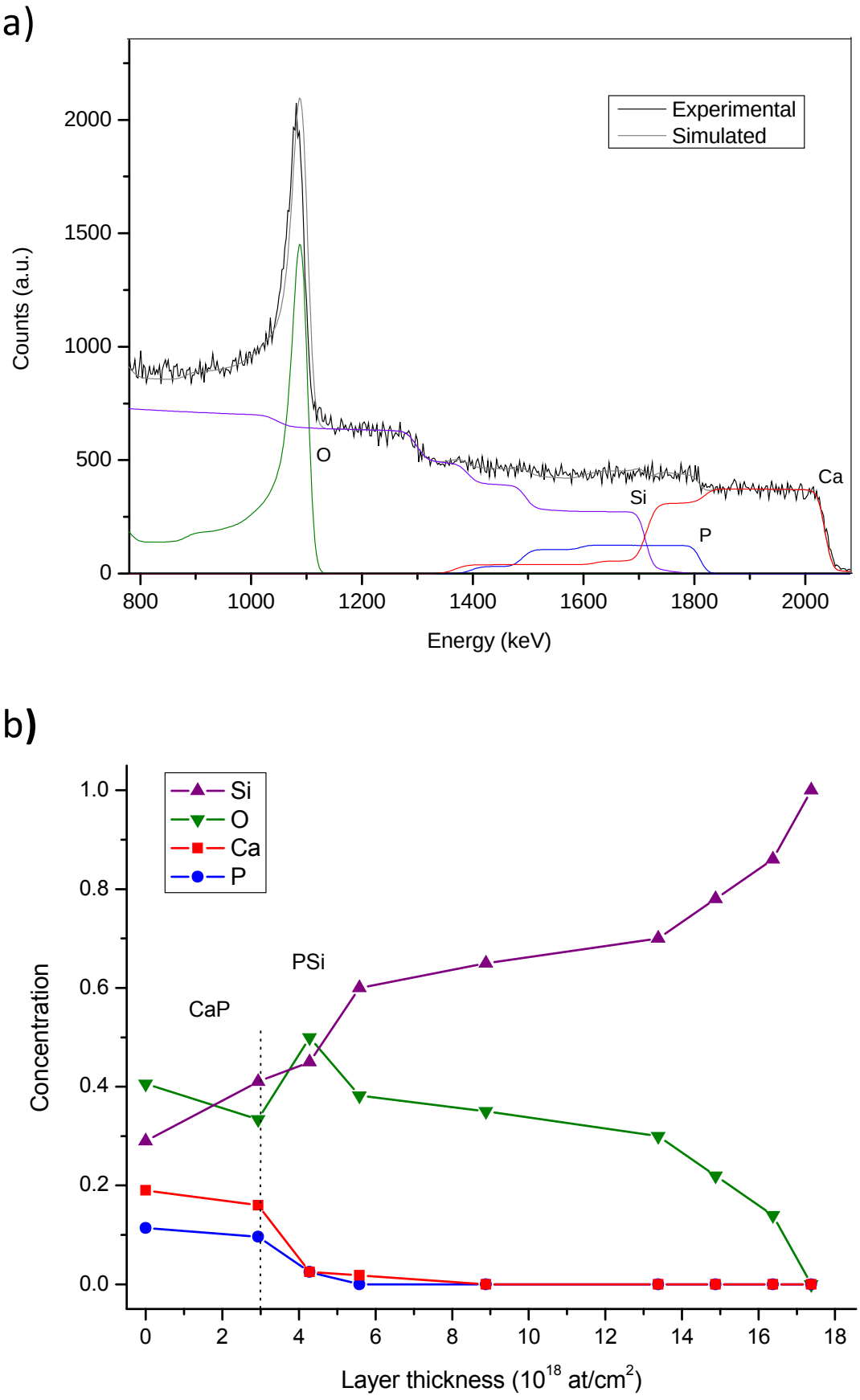

Figure 20. a) RBS spectrum of PSi/CaP composite prepared at standard conditions ($I_{Ca}/I_P = 1$ and $t_{Ca}/t_P = 1$) by CEA and its respective simulation, and b) concentration profile of PSi/CaP composite prepared at standard conditions by CEA.

Since the P and Si signal partially overlap in the spectrum, the individual contribution of each element (Si, O, Ca and P) to the overall spectrum simulated is also plotted. The in depth concentration profile (Fig. 20-b) was determined from the spectrum simulations. This profile indicates atomic concentrations (normalized to 1) of 0.19 for Ca and 0.114 for P at the top CaP surface. Si atoms are also detected in this layer because the spectrum includes both the top of CaP clusters and the exposed areas of the PSi surface since the film is not uniform (see Fig. 11-a1 and 11-b1). It is possible to identify the beginning of the PSi layer at a depth of aproximately $3x10^{18}$ at/cm^2, because there is a sudden increase of oxygen related to silicon oxide (SiO_2) in PSi [56]. On the other hand, Ca and P were also detected at concentrations of 0.025 each one at depths over $4x10^{18}$ at/cm^2, confirming the penetration of both elements into PSi structure, as initially suggested by EDX (see Fig. 11-b2). Applying the same data analysis (simulation to obtain profile concentrations) for both series of experiments made by CEA (I_{Ca}/I_P = 1, 1.67, 2 and t_{Ca}/t_P = 1, 1.67, 2), the profiles of Ca/P atomic ratios could be calculated (Fig. 21), as well as their respective error, by means of Poisson statistics [55]. The ideal Ca/P value related to HAP was only obtained for I_{Ca}/I_P = 1 and t_{Ca}/t_P = 1, while for the other two ratios (1.67 and 2), the Ca/P value was lower. This reduced value of the Ca/P ratio indicates the formation of other CaP phases in addition to HAP. Besides, although the calculated errors in the quantification of the Ca/P atomic ratios by RBS are considerable, they denote a clear tendency. The CaP crystals of MON and BRU detected in GA-XRD analysis (Fig. 18) match very well because their respective Ca/P atomic ratio is 1 [57] reducing the ideal value of 1.67 corresponding to HAP. Additionally, although the Ca/P atomic ratio is reduced when I_{Ca}/I_P and t_{Ca}/t_P are increased, the total amount of CaP synthesized is not decreased. That is to say, the total amount of CaP deposited by CEA increased when I_{Ca}/I_P and t_{Ca}/t_P were increased, but due to the multiplicity of the CaP phases and the activation of the ion species at the interface, the Ca/P atomic ratio was reduced.

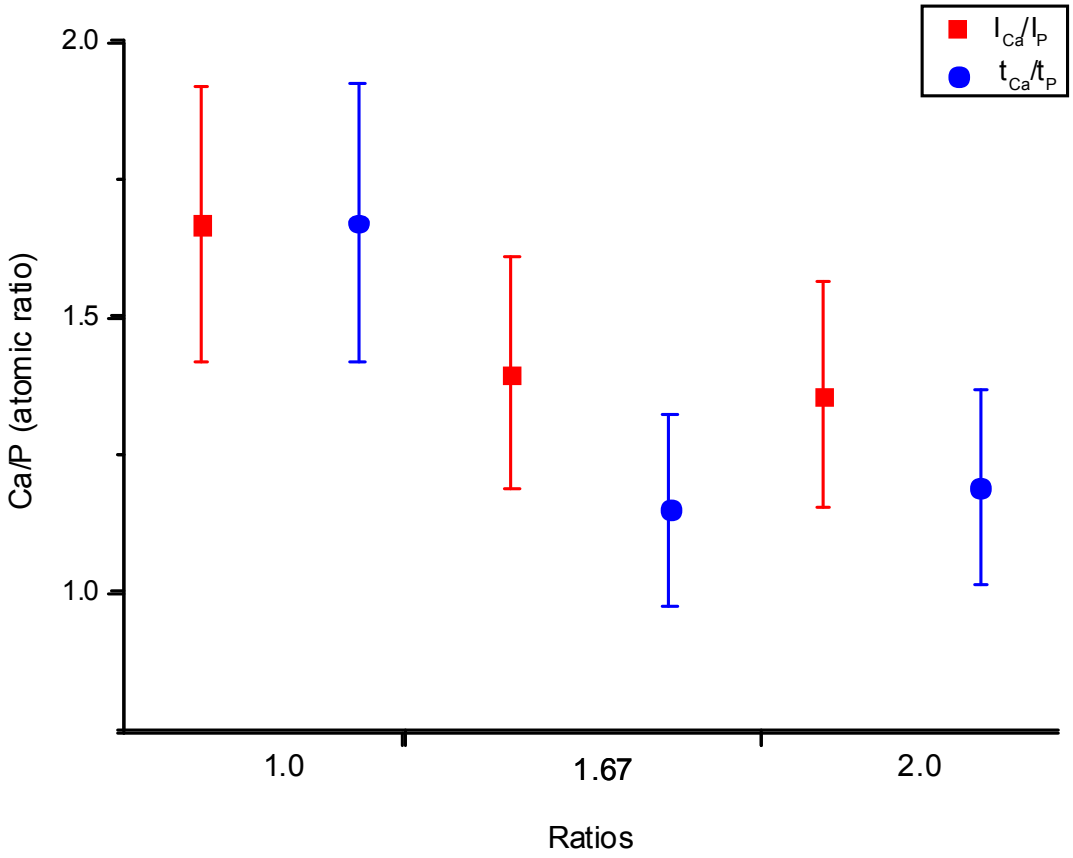

Figure 21. Quantification of the Ca/P atomic ratio by RBS of PSi/CaP composites prepared by CEA at different I_{Ca}/I_P (1, 1.67 and 2) and t_{Ca}/t_P (1, 1.67 and 2).

ii) PSi-CaP interface characterization by HAXPES

CSC and CEA techniques were used to synthesize the PSi/CaP biocomposites, but CaP integrated into PSi matrix was only obtained by means of CEA, irrespective of the time or current conditions, as indicated by Ca and P detection within PSi by EDX and RBS. In the case of PSi/CaP composites obtained by CSC, they were more like a bilayer material. Therefore, in order to study the chemical composition of the PSi-CaP interface, HAXPES analysis was carried out using a modified t_{Ca}/t_P series of CEA (see Section 4.2.1). Si 1s, P 1s and Ca 1s core levels spectra were measured using different photon excitation energies: 8.5, 12 and 15.5 keV. Fig. 22 shows spectra of PSi and HAP references. Their backgrounds were subtracted using the Shirley model and all spectra were smoothed, deconvoluted and normalized to their areas [58]. The data were processed using the OriginPro 8 and XPS PEAK 4.1 software.

Si 1s core level analysis of PSi sample reference is shown in spectra of Fig. 22-a. Results display two contributions at 1838.9 and 1843.6 eV, which are attributed to Si^0 and

SiO_2 species, respectively. Split between both peaks is 4.7 eV, which is close to previous reported value for Si 1s: 4.4 eV [59].

P 1s core level spectra of HAP reference prepared by CEA are shown in Fig. 22-b. The peak detected at 2149.0 eV is very close to that assigned to P-O or P=O compounds (2148.5 eV) [60], which are related to CaPs [61]. The peak of P^0 at 2145.5 eV [62] was also well identified. Ca 1s spectra of HAP reference are shown in Fig. 22-c. The Ca^0 contribution was detected at 4038.5 eV [62] and an additional peak was identified at 4042 eV, which can be assigned to HAP phase. The HAP coating in reference sample synthesized by CEA was previously confirmed by GA-XRD. However, at this moment, no previous work regarding at Ca 1s oxidation states has been reported and a more detailed study should be performed to provide a certain attribution of energy of Ca species in different chemical states.

The full-width at half-maximum (FWHM) of all spectra increased when the photon energy was increased, in such a way that resolution was lower for photon energies above 12 keV [58]. Table 2, derived from Fig. 22 shows the Si^0/SiO_2, P^0/(P-O + P=O) and Ca^0/HAP intensity ratios as a function of photon energy. With the exception Ca^0/HAP at 12 keV, the rest of neutral states/oxidized states intensity ratios tend to increase when photon energy is increased. This strongly suggests the presence of an in-depth composition gradient, with oxidized states exposing to the surface. The application of a detailed theoretical model to explain these results is a complex task in view of the heterogeneity of the samples and is considered out of the scope of this thesis.

Table 2. Si^0/SiO_2, P^0/(P-O + P=O) and Ca^0/HAP intensity ratios of references as a function of photon excitation energy.

Ratio	Photon excitation energy (keV)	Intensity ratio
Si^0/SiO_2	8.5	0.4645
	12.0	0.7033
	15.5	0.8369
P^0/(P-O + P=O)	8.5	0.1630
	12.0	0.2407
	15.5	0.5902
Ca^0/HAP	8.5	0.2075
	12.0	0.8109
	15.5	0.3138

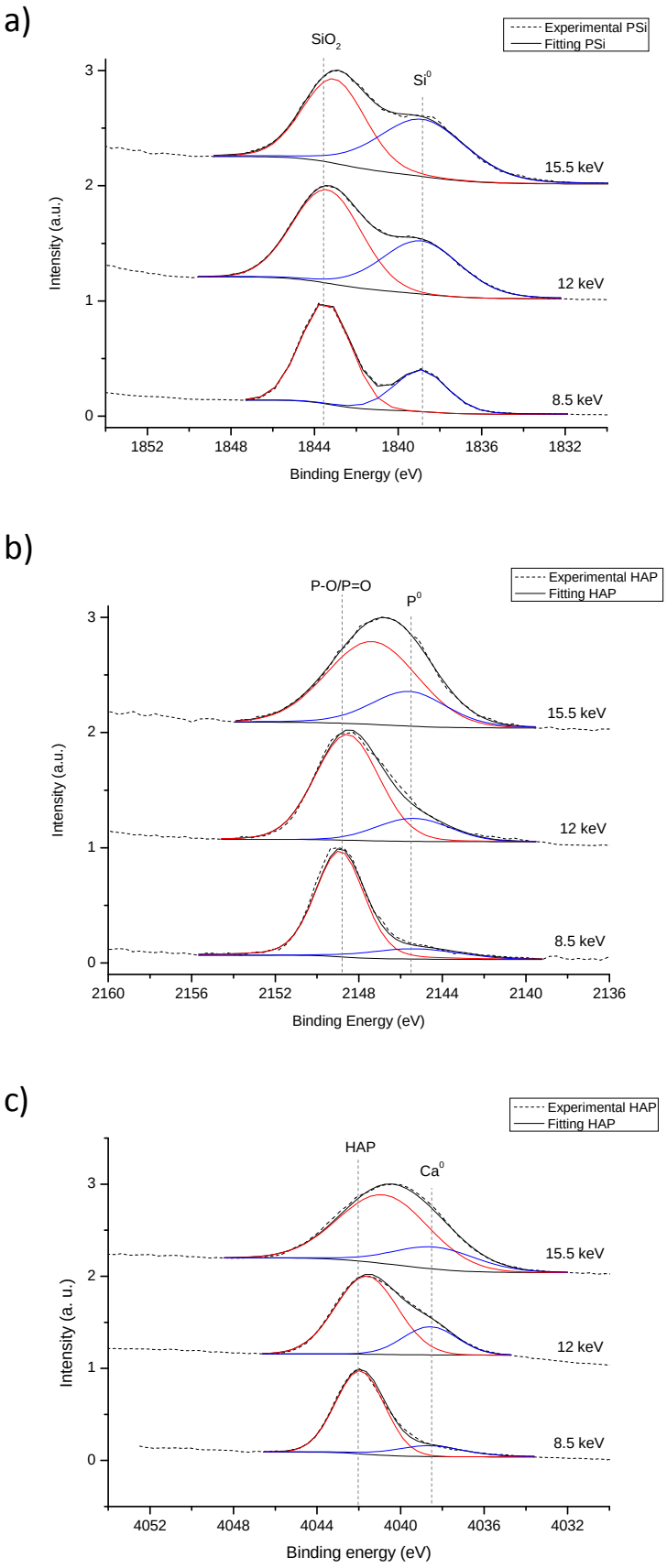

Figure 22. Si 1s core level spectra of PSi reference obtained at 60 mA/cm^2 for 90 s (a). P 1s (b) and Ca 1s (c) core level spectra of HAP reference prepared by CEA at standard conditions: $I_{Ca}/I_P = 1$ and $t_{Ca}/t_P = 1$, during 20 Ca/P cycles (30 s each). Measurements were carried out at 8.5, 12 and 15.5 keV. Spectra were smoothed and normalized to their areas and their backgrounds were subtracted using a Shirley model.

The Si 1s, P 1s and Ca 1s core levels spectra of t_{Ca}/t_P series are shown in Fig. 23, Fig. 24 and Fig. 25, respectively. As in the case of spectra references, their backgrounds were subtracted using a Shirley model. Spectra were also smoothed, normalized to their areas and deconvoluted into their respective contributions.

Si 1s core level analysis is shown in spectra of Fig. 23. Fig. 23-a corresponds to t_{Ca}/t_P = 1, Fig. 23-b to t_{Ca}/t_P = 1.67 and Fig. 23-c to t_{Ca}/t_P = 2. Results display the previously identified peaks at 1838.9 and 1843.6 eV, which are attributed to Si^0 and SiO_2 species, respectively. As in the case of PSi reference, Si^0/SiO_2 intensity ratio also tends to increase when photon energy is increased for three t_{Ca}/t_P cases (Table 3), which evidences the presence of an in-depth composition gradient, with oxidized species occupying the sample surface.

Table 3. Si^0/SiO_2 intensity ratio as a function of photon excitation energy.

Sample	**Photon excitation energy (keV)**	**Si^0/SiO_2**
t_{Ca}/t_P = 1	8.5	0.2159
	12.0	0.3339
	15.5	0.4404
t_{Ca}/t_P = 1.67	8.5	0.3011
	12.0	0.4070
	15.5	0.6895
t_{Ca}/t_P = 2	8.5	0.3084
	12.0	0.3619
	15.5	0.3370

P 1s core level spectra are shown in Fig. 24-a for t_{Ca}/t_P = 1, Fig. 24-b for t_{Ca}/t_P = 1.67 and Fig. 24-c for t_{Ca}/t_P = 2. As in the case of the HAP reference, in the three t_{Ca}/t_P cases, two main contributions related to P-O or P=O compounds (2149.0 eV) were identified. For P^0 peak (2145.5 eV), just some traces were detected in most cases, as illustrated by the reported P-O + P=O values in Table 4. The intensity of the P 1s spectrum obtained at 15.5 keV in t_{Ca}/t_P = 1 (Fig. 24-a) is notably decreased denoting a limited P integration. On the other hand, an unusual peak at 2152.0 eV in the spectra of t_{Ca}/t_P = 2 was observed (see P* in Fig. 24-c). This contribution could be assigned to PYR phase. Remind that for t_{Ca}/t_P = 2 additional phases to HAP, MON and BRU are induced. Since this sample was submitted to post-thermal treatment, the PYR is most surely present as suggested by the associated GA-XRD results.

Table 4. P^0/(P-O + P=O) intensity ratio as a function of photon excitation energy.

Sample	Photon excitation (keV)	P^0/(P-O+P=O)	P*/(P-O+P=O)
$t_{Ca}/t_P = 1$	8.5	0.0956	-
	12.0	0.2226	-
	15.5	0.1003	-
$t_{Ca}/t_P = 1.67$	8.5	0.0365	-
	12.0	0.0319	-
	15.5	0.1384	-
$t_{Ca}/t_P = 2$	8.5	0.0768[a]	0.0776
	12.0	0.0898[a]	0.1374
	15.5	1.2391[a]	1.5876

[a]New P* component was not considered.

Lastly, Ca 1s core level spectra of t_{Ca}/t_P series are shown in Fig. 25-a for $t_{Ca}/t_P = 1$, Fig. 25-b for $t_{Ca}/t_P = 1.67$ and Fig. 25-c for $t_{Ca}/t_P = 2$. Peaks related to Ca^0 (4038.5 eV) and HAP (4042 eV) were detected in all t_{Ca}/t_P cases. Additionally for $t_{Ca}/t_P = 2$ (Fig. 25-c), an extra contribution at 4045.5 keV was identified (Ca*). This peak could be assigned to PYR phase, which would match with the extra contribution detected in P spectra of $t_{Ca}/t_P = 2$. Besides, the peak intensity of this species also increased in depth as their crystalline phase related spectra in the P 1s analysis (Fig. 4-c). As in the case of the P spectra at 15.5 keV for $t_{Ca}/t_P = 1$ (Fig. 24-a), the intensity of the Ca spectrum obtained by this photon energy was the lowest (Fig. 25-a). This denotes that there was also a limited Ca integration into PSi for $t_{Ca}/t_P = 1$. Thus, spectra of $t_{Ca}/t_P = 1.67$ (Fig. 25-b) and $t_{Ca}/t_P = 2$ (Fig. 25-c) showed a higher integration of Ca species into PSi structure than $t_{Ca}/t_P = 1$ (Fig. 25-a). On the other hand, for $t_{Ca}/t_P = 1$ and $t_{Ca}/t_P = 1.67$, the Ca^0/HAP intensity ratio tends to increase when photon energy is increased, in contrast with $t_{Ca}/t_P = 2$ (Table 5).

Table 5. Ca^0/HAP intensity ratio as a function of photon excitation energy.

Sample	Photon excitation (keV)	Ca^0/HAP	Ca^*/HAP
$t_{Ca}/t_P = 1$	8.5	0.0353	-
	12.0	0.2145	-
	15.5	0.1264	-
$t_{Ca}/t_P = 1.67$	8.5	0.0304	-
	12.0	0.0552	-
	15.5	0.4291	-
$t_{Ca}/t_P = 2$	8.5	5.9524[a]	2.6829
	12.0	2.2945[a]	2.3582
	15.5	0.7859[a]	2.8974

[a]New Ca* component was not considered.

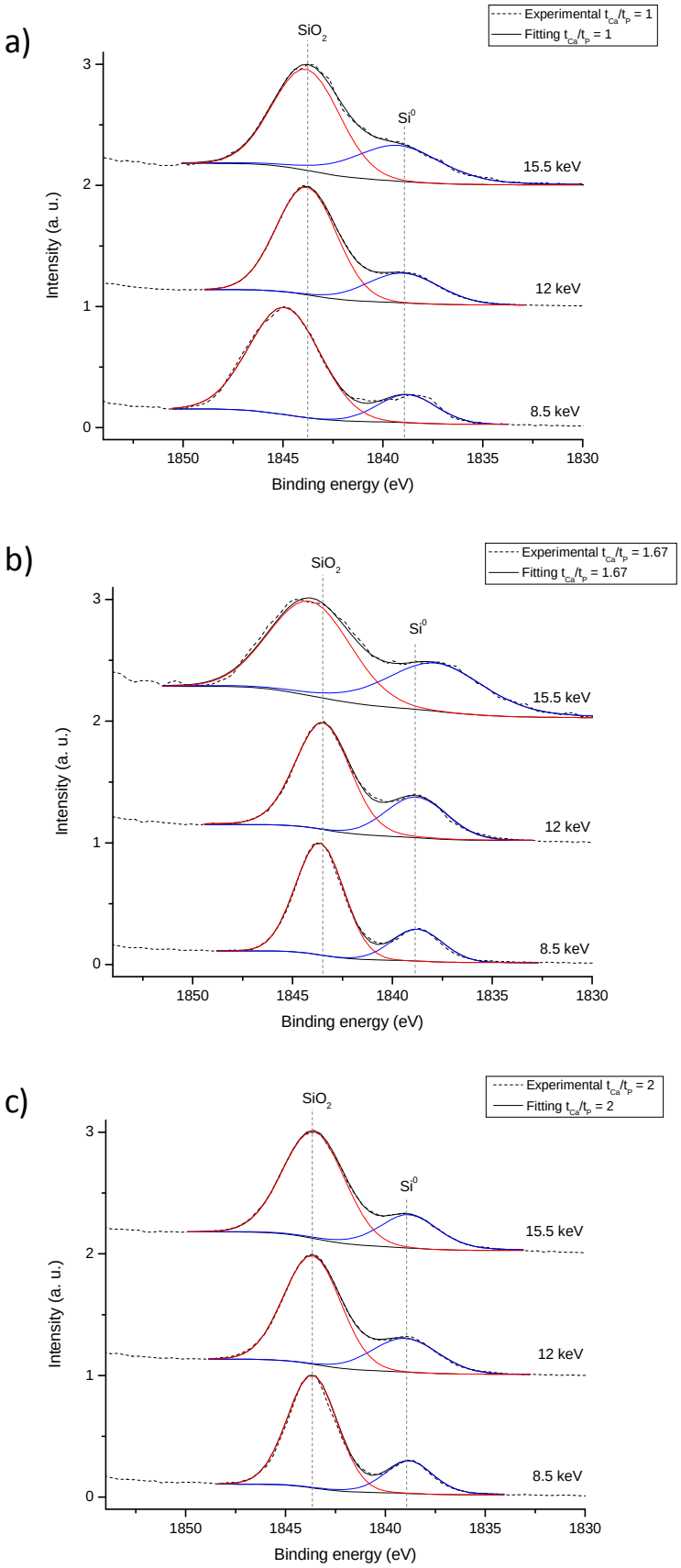

Figure 23. Si 1s core level spectra of PSi/CaP samples prepared by CEA measured at 8.5, 12 and 15.5 keV: a) $t_{Ca}/t_P = 1$, b) $t_{Ca}/t_P = 1.67$, and c) $t_{Ca}/t_P = 2$. Spectra were smoothed and normalized to their areas and their backgrounds were subtracted using a Shirley model.

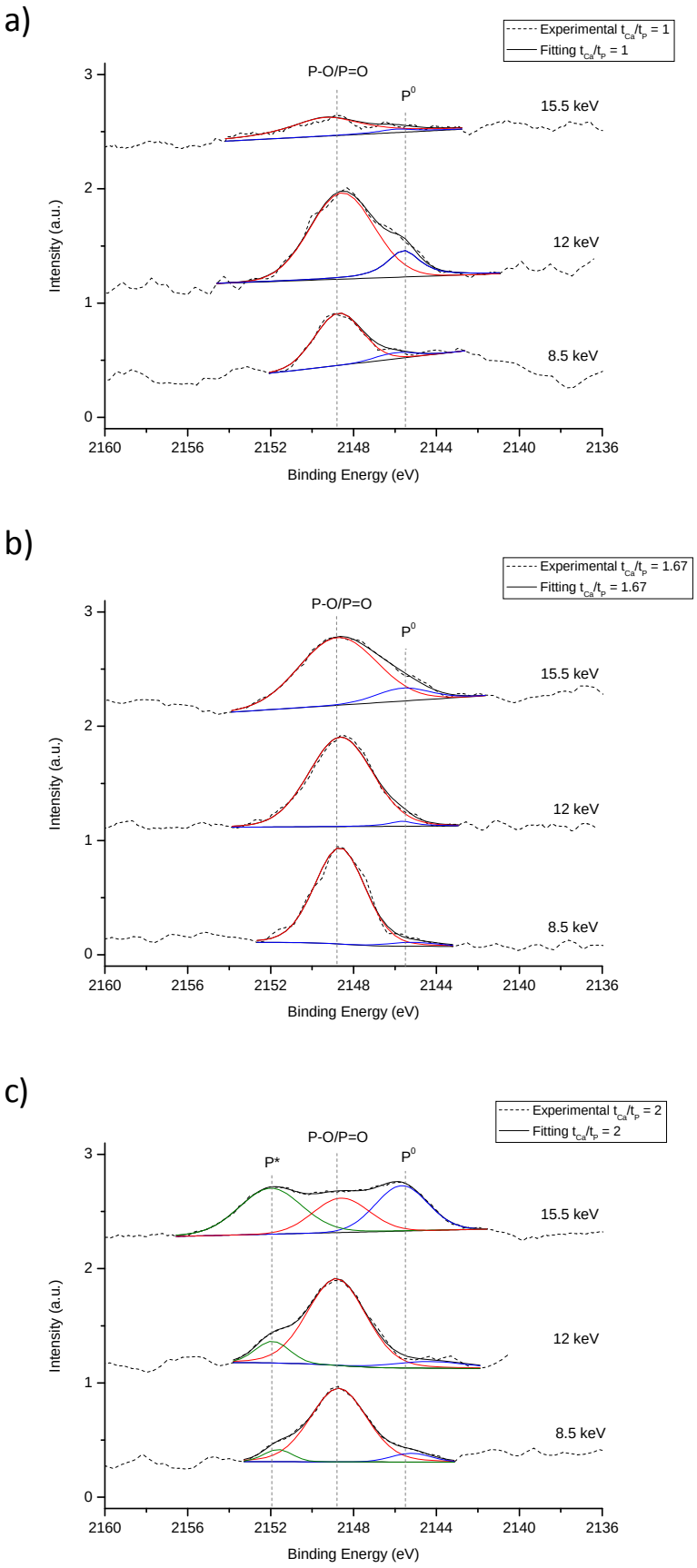

Figure 24. P 1s core level spectra of PSi/CaP samples prepared by CEA, which were measured at 8.5, 12 and 15.5 keV: a) $t_{Ca}/t_P = 1$, b) $t_{Ca}/t_P = 1.67$, and c) $t_{Ca}/t_P = 2$. Spectra were smoothed and normalized to their areas and their backgrounds were subtracted using a Shirley model.

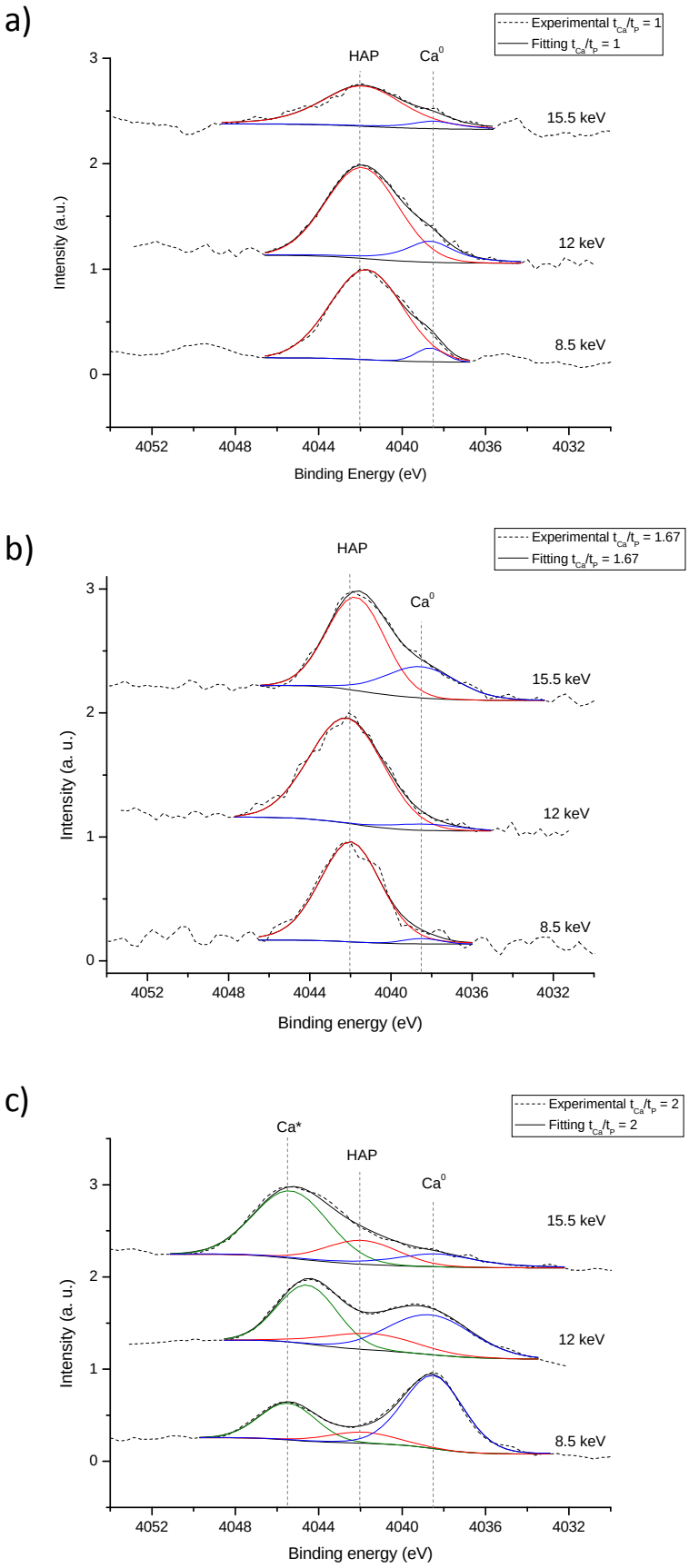

Figure 25. Ca 1s core level spectra of PSi/CaP samples prepared by CEA, which were measured at 8.5, 12 and 15.5 keV: a) $t_{Ca}/t_P = 1$, b) $t_{Ca}/t_P = 1.67$, and c) $t_{Ca}/t_P = 2$. Spectra were smoothed and normalized to their areas and their backgrounds were subtracted using a Shirley model.

According to the previous Ca 1s and P 1s core levels spectra, a scheme of CaP particles nucleated on PSi could be developed (Fig. 26). Electrodeposition in $t_{Ca}/t_P = 1$ generated the lowest penetration of Ca, thus also P, because P reacts with Ca nucleated on PSi. In the case of $t_{Ca}/t_P = 1.67$ and $t_{Ca}/t_P = 2$, they promoted an increasing incorporation of Ca species, thus also P. Besides, the tendency observed in the samples prepared in bulk of $t_{Ca}/t_P = 2$ to form multiple CaP phases (MON and BRU in addition to HAP), was also repeated in the PSi-CaP interface due to PYR identification. However, in order to strengthen this analysis, a more detailed study on Ca 1s oxidation states species is required.

The scheme of Fig. 26 summarizes the influence of t_{Ca}/t_P on the formation of CaP in the two studied regions: bulk CaP (Section 4.3.2) and PSi-CaP interface (current Section).

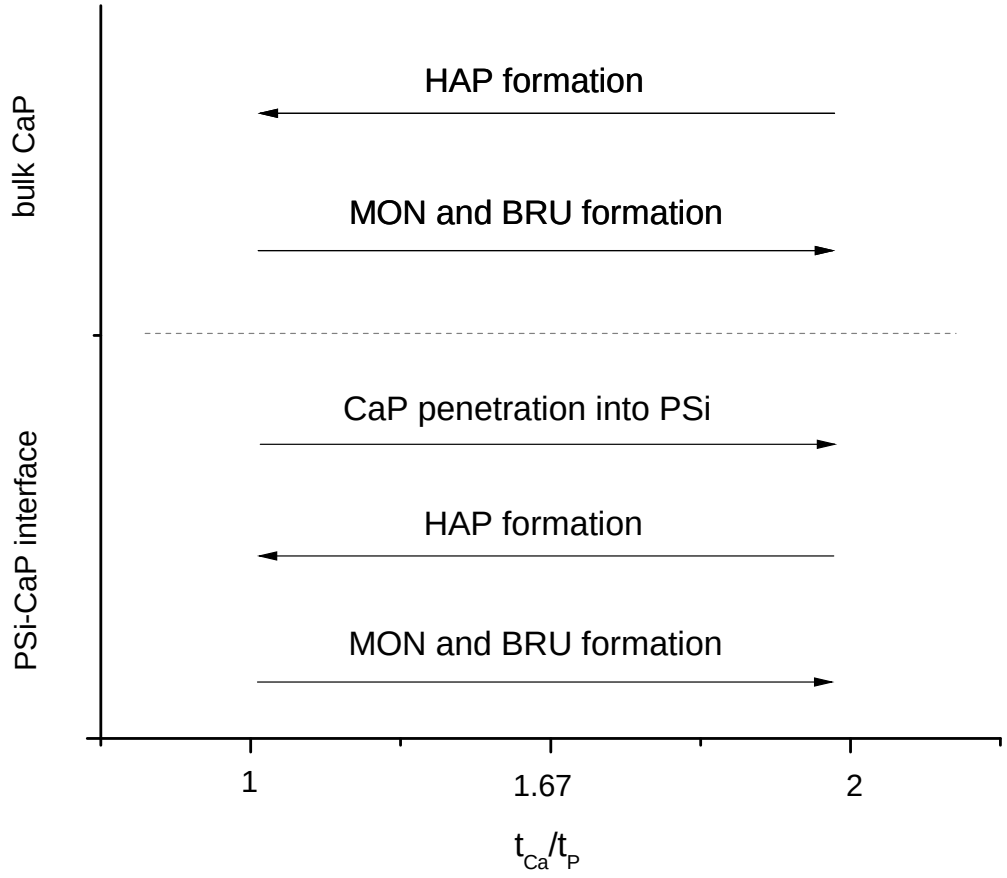

Figure 26. Influence of t_{Ca}/t_P on the formation of CaP in different regions: PSi-CaP interface and bulk CaP.

iii) Biocompatibility characterization

As in the case of composites prepared by CSC, the biocompatibility of PSi/CaP composite prepared by CEA at standard conditions (I_{Ca}/I_P = 1 and t_{Ca}/t_P = 1) was also studied by means of hMSCs culture. This PSi/CaP sample was selected to test the biocompatibility of bioceramics because it was the sample containing a dominant HAP phase. Fluorescence microscopy was used to characterize the attachment and morphology of the hMSCs onto PSi and PSi/CaP sample (Fig. 26). The cells cultured on the composite processed by CEA, presented a round expanded actin cytoskeleton, which indicates that their ability for attaching to the surface is not challenged (Fig. 26-b1 and Fig. 26-b2). Besides, cells are in active mitosis as on the PSi control (see arrows, 26-a1 and Fig. 26-a2), which was not observed in the case of CSC samples. These results indicate a short time scale biocompatibility due to the ability of the PSi/CaP composite prepared by CEA to support hMSC adhesion and proliferation along with maintaining the normal morphological appearance of cells.

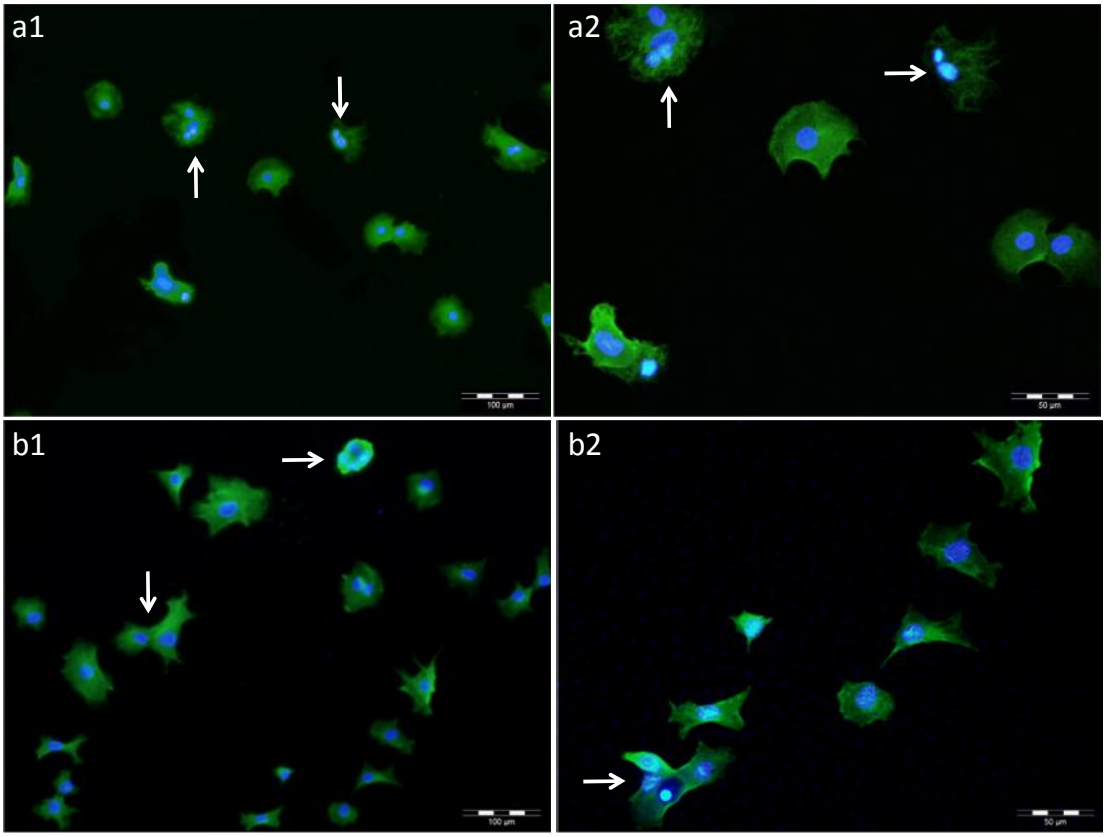

Figure 26. Fluorescence microscopy images of hMSCs cultured on PSi (a1 and a2) and PSi/CaP composites prepared by CEA at standard conditions (I_{Ca}/I_P = 1 and t_{Ca}/t_P = 1) (b1 and b2) showing actin cytoskeleton stained by phalloidin-Alexa488 and cell nuclei stained by DAPI.

4.4 Conclusions

This work demonstrated that the proposed methods based on cyclic CaP deposition are suitable for the construction of PSi/CaP composites for bone engineering scaffolds. Both techniques CSC and CEA consisted on alternate Ca and P deposition steps on PSi. The morphology of CaP deposited on PSi was observed by SEM and their chemical composition was analyzed by EDX, FTIR-SR and DRX. Both composite synthesis techniques were studied in terms of the mineral phase grown and the optimization for mineralizing CaP in its HAP phase was addressed. On one side, this study reveals that the CSC and CEA techniques are suitable for producing specific morphologies and CaP phases using the same independent Ca and P stem-solutions at neutral pH and at room temperature. Besides, depending on the used technique it is possible to form a bilayer material (PSi/CaP prepared by CSC) or an integrated composite (PSi/CaP prepared by CEA). The BRU phase is favoured with the CSC technique and the HAP phase is better synthesized using the CEA technique. In the case of CEA, an approximation to the mechanism of CaP electrodeposition was studied by a simple system resistance calculation. Results have shown that CaP deposition on PSi increases linearly with the cycles when carried at room temperature, but the increase is exponential when temperature reaction is increased.

On the other hand, the synthesis of HAP in PSi/CaP composite by CEA was additionaly validated by Ca/P atomic ratio quantification by means of RBS. These results indicated that controlling the synthesis parameters of CEA, it is possible to generate CaP on PSi with a Ca/P atomic ratio of 1.67, the ideal value related to HAP. By means of HAXPES it was possible to study the CaP-PSi interface. This study was performed using a modified series of standard t_{Ca}/t_P with cycle time of 30 s and a total of 2 cycles, which were contrasted with the references, one of PSi and another of HAP prepared by CEA at standard conditions. At this moment, there are no previous works regarding the Ca 1s oxidation states, thus, two peaks of binding energy for the oxidized species of Ca 1s were proposed: HAP at 4042 eV and PYR at 4045.5 eV. According to this, $t_{Ca}/t_P = 1$ generates the lowest penetration of CaP particles. In the case of $t_{Ca}/t_P = 1.67$ and $t_{Ca}/t_P = 2$, both promote the incorporation of CaP particles into the PSi. Besides, $t_{Ca}/t_P = 2$ tends to form multiple CaP phases: HAP, MON and BRU. Then, according to this analysis, it is recommendable to synthesize CaP on PSi starting with cycles of higher t_{Ca}/t_P or I_{Ca}/I_P because these conditions enhance CaP penetration on PSi. On a second stage, if an HAP phase is desired, it is recommended to reduce the t_{Ca}/t_P ratio at 1. However, in order to

validate this model, further studies regarding oxidation states from Ca 1s spectra are indispensable.

Finally, the biocompatibility was demonstrated by the ability of the PSi/CaP composite prepared by CEA to support bone-derived progenitor cells adhesion and suggesting proliferation. In this regards, although cells cultured onto PSi/CaP provided by CSC showed adhesion onto the surface, there was no evidence of proliferation. Moreover, the culture on PSi/CaP composite obtained by CSC modified the normal morphological appearance of cells acquiring the shape of the solid flat-plates of BRU clusters. In addition, as the biocompatibility of composites was demonstrated using hMSCs, it opens further work to create scaffold–cell hybrids for *in vivo* applications.

References

[1] Hutmacher DW, Schantz JT, Lam CXF, Tan KC, Lim TC. State of the art and future directions of scaffold-based bone engineering from a biomaterials perspective. J Tissue Eng Regen Med 2007;1(4):245-260.

[2] Evans ND, Gentleman E, Polak JM. Scaffolds for stem cells. Materials Today 2006;9(12):26-33.

[3] Naveas N, Costa VT, Gallach D, Hernandez-Montelongo J, Palma RJM, Garcia-Ruiz JP, et al. Chemical stabilization of porous silicon for enhanced biofunctionalization with immunoglobulin. Sci Technol Adv Mater 2012;13(4):045009.

[4] Park JH, Gu L, von Maltzahn G, Ruoslahti E, Bhatia SN, Sailor MJ. Biodegradable luminescent porous silicon nanoparticles for in vivo applications. Nat Mater 2009;8(4):331.

[5] Kumar DS, Banji D, Madhavi B, Bodanapu V, Dondapati S, Sri AP. Nanostrctured porous silicon – A novel biomaterial for drug delivery. Int J Pharm Pharm Sci 2009;1(2):8-16.

[6] Dorozhkin SV, Epple M. Biological and medical significance of calcium phosphates. Angew Chem Int Ed 2002;41(17):3130-3146.

[7] Seong JM, Kim B, Park J, Kwon IK, Mantalaris A, Hwang Y. Stem cells in bone tissue engineering. Biomed Mater 2010;5(6):062001.

[8] Bertazzo S, Zambuzzi WF, Campos DDP, Ogeda TL, Ferreira CV, Bertran CA. Hydroxyapatite surface solubility and effect on cell adhesion. Colloids Surf , B 2010;78(2):177-184.

[9] Swetha M, Sahithi K, Moorthi A, Srinivasan N, Ramasamy K, Selvamurugan N. Biocomposites containing natural polymers and hydroxyapatite for bone tissue engineering. Int J Biol Macromol 2010;47(1):1-4.

[10] Wolf G. Energy regulation by the skeleton. Nutr Rev 2008;66(4):229-233.

[11] Zhu W, Zhang X, Wang D, Lu W, Ou Y, Han Y, et al. Experimental study on the conduction function of nano-hydroxyapatite artificial bone. Micro & Nano Letters, IET 2010;5(1):19-27.

[12] Mahabole M, Aiyer R, Ramakrishna C, Sreedhar B, Khairnar R. Synthesis, characterization and gas sensing property of hydroxyapatite ceramic. Bull Mater Sci 2005;28(6):535-545.

[13] Ergun C, Doremus R, Lanford W. Hydroxylapatite and titanium: Interfacial reactions. J Biomed Mater Res A 2003;65(3):336-343.

[14] Porter AE, Buckland T, Hing K, Best SM, Bonfield W. The structure of the bond between bone and porous silicon-substituted hydroxyapatite bioceramic implants. J Biomed Mater Res A 2006;78(1):25-33.

[15] Toworfe G, Composto R, Shapiro I, Ducheyne P. Nucleation and growth of calcium phosphate on amine-, carboxyl-and hydroxyl-silane self-assembled monolayers. Biomaterials 2006;27(4):631-642.

[16] Hernández-Montelongo J, Muñoz-Noval A, Torres-Costa V, Martín-Palma R, Manso-Silvan M. Cyclic Calcium Phosphate Electrodeposition on Porous Silicon. Int J Electrochem Sci 2012;7:1840-1851.

[17] Jelinek M, Olan V, Jastrabik L, Studnika V, Hnatowicz V, Kvítek J, et al. Effect of processing parameters on the properties of hydroxylapatite films grown by pulsed laser deposition. Thin Solid Films 1995;257(1):125-129.

[18] Van Dijk K, Schaeken H, Wolke J, Jansen J, Habraken F, Verhoeven J, et al. Influence of Ar pressure on rf magnetron-sputtered Ca5 (PO4) 3OH layers. Surf Coat Tech 1995;76:206-210.

[19] Feddes B, Wolke J, Vredenberg A, Jansen J. Initial deposition of calcium phosphate ceramic on polyethylene and polydimethylsiloxane by rf magnetron sputtering deposition: the interface chemistry. Biomaterials 2004;25(4):633-639.

[20] Ektessabi A, Hamdi M. Characterization of calcium phosphate bioceramic films using ion beam analysis techniques. Surf Coat Tech 2002;153(1):10-15.

[21] Manso M, Martínez-Duart J, Langlet M, Jiménez C, Herrero P, Millon E. Aerosol-gel-derived microcrystalline hydroxyapatite coatings. J Mater Res 2002;17(6):1482-1489.

[22] Chen F, Lam W, Lin C, Qiu G, Wu Z, Luk K, et al. Biocompatibility of electrophoretical deposition of nanostructured hydroxyapatite coating on roughen titanium surface: In vitro evaluation using mesenchymal stem cells. J Biomed Mater Res B 2007;82(1):183-191.

[23] Lim HN, Kassim A, Huang NM, Khiewc PS, Chiu WS. Three-dimensional flower-like brushite crystals prepared from high internal phase emulsion for drug delivery application. Colloids Surf Physicochem Eng Aspects 2009;345(1):211-218.

[24] Bisi O, Ossicini S, Pavesi L. Porous silicon: a quantum sponge structure for silicon based optoelectronics. Surf Sci Rep 2000;38(1-3):1-126.

[25] Parkhutik V, Martínez MSJ, Senent EG. Processing of Infrared Spectroscopy Data on Thin Porous Films Using Software “Prospect”. J Porous Mat 2000;7(1):239-242.

[26] Martin-Palma RJ, Manso-Silvan M, Torres-Costa V. Biomedical applications of nanostructured porous silicon: a review. J Nanophotonics 2010;4(042502):1-20.

[27] Rößler S, Sewing A, Stölzel M, Born R, Scharnweber D, Dard M, et al. Electrochemically assisted deposition of thin calcium phosphate coatings at near-physiological pH and temperature. J Biomed Mater Res-A 2003;64(4):655-663.

[28] Rehman I, Bonfield W. Characterization of hydroxyapatite and carbonated apatite by photo acoustic FTIR spectroscopy. J Mater Sci Mater Med 1997;8(1):1-4.

[29] Muñoz-Noval Á, Sánchez-Vaquero V, Torres-Costa V, Gallach D, Manso-Silván M, García-Ruiz JP, et al. Silicon-based hybrid luminescent/magnetic porous nanoparticles for biomedical applications. J Nanophotonics 2011;5(1):051505-051505-10.

[30] Arifuzzaman S, Rohani S. Experimental study of brushite precipitation. J Cryst Growth 2004;267(3-4):624-634.

[31] Bard AJ, Faulkner LR. Electrochemical methods fundamentals and applications. 2nd ed. New York: John Wiley & Sons; 2001.

[32] Kumta PN, Sfeir C, Lee DH, Olton D, Choi D. Nanostructured calcium phosphates for biomedical applications: novel synthesis and characterization. Acta Biomaterialia 2005;1(1):65-83.

[33] Manso M, Jimenez C, Morant C, Herrero P, Martinez-Duart JM. Electrodeposition of hydroxyapatite coatings in basic conditions. Biomaterials 2000;21(17):1755-1761.

[34] Rodríguez K, Renneckar S, Gatenholm P. Biomimetic Calcium Phosphate Crystal Mineralization on Electrospun Cellulose-Based Scaffolds. ACS Appl Mater Interfaces 2011;3(3):681-689.

[35] Anderson SHC, Elliott H, Wallis DJ, Canham LT, Powell JJ. Dissolution of different forms of partially porous silicon wafers under simulated physiological conditions. Phys Stat Sol (a) 2003;197(2):331-335.

[36] Cuneyt Tas A, Korkusuz F, Timucin M, Akkas N. An investigation of the chemical synthesis and high-temperature sintering behaviour of calcium hydroxyapatite (HA) and tricalcium phosphate (TCP) bioceramics. J Mater Sci Mater Med 1997;8(2):91-96.

[37] Khung Y, Barritt G, Voelcker N. Using continuous porous silicon gradients to study the influence of surface topography on the behaviour of neuroblastoma cells. Exp Cell Res 2008;314(4):789-800.

[38] Low SP, Williams KA, Canham LT, Voelcker NH. Evaluation of mammalian cell adhesion on surface-modified porous silicon. Biomaterials 2006;27(26):4538-4546.

[39] LeGeros R, Lin S, Rohanizadeh R, Mijares D, LeGeros J. Biphasic calcium phosphate bioceramics: preparation, properties and applications. J Mater Sci Mater Med 2003;14(3):201-209.

[40] Föll H, Christophersen M, Carstensen J, Hasse G. Formation and application of porous silicon. Mat Sci Eng R 2002;39(4):93-141.

[41] Lehmann V. Electrochemistry of silicon. : Wiley Online Library; 2002.

[42] Lehmann V, Hönlein W, Reisinger H, Spitzer A, Wendt H, Willer J. A novel capacitor technology based on porous silicon. Thin Solid Films 1996;276(1-2):138-142.

[43] Ronkel F, Schultze JW. Electrochemical aspects of porous silicon formation. J Porous Mat 2000;7(1):11-16.

[44] Bicelli LP, Bozzini B, Mele C, D'Urzo L. A review of nanostructural aspects of metal electrodeposition. Int J Electrochem Sci 2008;3(4):356-408.

[45] Ban S, Maruno S. Effect of temperature on electrochemical deposition of calcium phosphate coatings in a simulated body fluid. Biomaterials 1995;16(13):977-981.

[46] Arellano-Jiménez MJ, García-García R, Reyes-Gasga J. Synthesis and hydrolysis of octacalcium phosphate and its characterization by electron microscopy and X-ray diffraction. J Phys Chem Solids 2009;70(2):390-395.

[47] Kar A, Raja KS, Misra M. Electrodeposition of hydroxyapatite onto nanotubular TiO2 for implant applications. Surf Coat Tech 2006;201(6):3723-3731.

[48] Huang LY, Xu KW, Lu J. A study of the process and kinetics of electrochemical deposition and the hydrothermal synthesis of hydroxyapatite coatings. J Mater Sci Mater Med 2000;11(11):667-673.

[49] Jeske M, Schultze JW, Thönissen M, Münder H. Electrodeposition of metals into porous silicon. Thin Solid Films 1995;255(1-2):63-66.

[50] Lu X, Zhao Z, Leng Y. Calcium phosphate crystal growth under controlled atmosphere in electrochemical deposition. J Cryst Growth 2005;284(3-4):506-516.

[51] Montero-Ocampo C, Villegas D, Veleva L. Controlled potential electrodeposition of calcium phosphate on Ti6Al4V. J Electrochem Soc 2005;152(10):C692.

[52] Redepenning J, Schlessinger T, Burnham S, Lippiello L, Miyano J. Characterization of electrolytically prepared brushite and hydroxyapatite coatings on orthopedic alloys. J Biomed Mater Res 1996;30(3):287-294.

[53] Harris DC. Quantitative chemical analysis. 6th ed. New York: W.H. Freeman; 2003.

[54] Lai C, Tang SQ, Wang YJ, Wei K. Formation of calcium phosphate nanoparticles in reverse microemulsions. Mater Lett 2005;59(2-3):210-214.

[55] Mayer M. *SIMNRA user's guide* . Max-Planck-Inst für Plasmaphysik 1997.

[56] Torres-Costa V, Pászti F, Climent-Font A, Martín-Palma R, Martínez-Duart J. Optical and in-depth RBS characterization of porous silicon interference filters. J Electrochem Soc 2005;152:G846.

[57] Driessens F, Boltong M, De Maeyer E, Wenz R, Nies B, Planell J. The Ca/P range of nanoapatitic calcium phosphate cements. Biomaterials 2002;23(19):4011-4017.

[58] Benito N, Galindo RE, Rubio-Zuazo J, Castro GR, Palacio C. High-and low-energy x-ray photoelectron techniques for compositional depth profiles: destructive versus non-destructive methods. J Phys D 2013;46(6):065310.

[59] Boujamaa R, Baudot S, Rochat N, Pantel R, Martinez E, Renault O, et al. Impact of high temperature annealing on La diffusion and flatband voltage (Vfb) modulation in TiN/LaOx/HfSiON/SiON/Si gate stacks. J Appl Phys 2012;111:054110.

[60] Malmgren S, Ciosek K, Hahlin M, Gustafsson T, Gorgoi M, Rensmo H, et al. Comparing Anode and Cathode Electrode/Electrolyte Interface Composition and Morphology using Soft and Hard X-ray Photoelectron Spectroscopy. Electrochim Acta 2013;97:23-32.

[61] Hofmann MP, Young AM, Gbureck U, Nazhat SN, Barralet JE. FTIR-monitoring of a fast setting brushite bone cement: effect of intermediate phases. J Mater Chem 2006;16(31):3199-3206.

[62] Bearden J, Burr A. Reevaluation of X-ray atomic energy levels. Rev Mod Phys 1967;39(1):125.

Chapter 5:

Conclusions and Perspectives

5.1 Conclusions

In this thesis new modifications to porous silicon (PSi) were presented, which allowed obtaining new advanced biomaterial structures. Specifically, the development of new synthesis processes, the physicochemical characterization and the biocompatibility testing of new PSi-based biomaterials has been described aiming at applications in drug delivery and cell scaffolds. For the former application, this thesis has focused on the development of PSi/Cyclodextrin Hybrids, while PSi/Calcium Phosphate Bioceramics were prepared as cell scaffolds for skeletal tissues. The following specific conclusions can be derived from the results presented in this thesis:

5.1.1 PSi/cyclodextrin drug delivery hybrids

i) Two kinds of PSi (nanoporous and macroporous) were used as substrates to synthesize PSi/CD drug delivery hybrids. Both PSi matrices were properly stabilized by a simple chemical route using hydrogen peroxide. As a consequence of stabilization, PSi exhibited a transition towards a hydrophilic character as illustrated by water contact angle technique. Such transition could be explained by the presence of Si-OH (identified by FTIR-ATR and XPS). That hydrophilization was an essential requirement to functionalize correctly both PSi substrates by β-cyclodextrin *in-situ* polymerization using citric acid as crosslinking agent.

ii) Good adherence was achieved between the porous matrix of both types of PSi substrates and β-cyclodextrin-citric acid polymer (polyCD). Such bonding strength was induced by two main phenomena: the PSi hydrophilic compatibility with the external wall of β-cyclodextrin after chemical oxidation, and the anchoring effect of the porous matrix.

iii) The biocompatibility of synthesized PSi/CD hybrids and their respective substrates was evaluated by means of the deposition and *in vitro* proliferation of L132 cells. Although different cell adhesion behaviors were observed on each sample, they showed a viable cytocompatibility after 24 h of culture.

iv) In order to test PSi/cyclodextrin hybrids as potential intraocular drug delivery systems, they were loaded with two drugs used in post-ophthalmic surgery: ciprofloxacin (CFX, an antibiotic) and prednisolone (PDN, an anti-inflammatory). The kinetic studies were carried out by means of drug release profiles in two different media: distilled water and phosphate buffer saline (PBS). Drug release profiles showed that PSi/CD hybrids have a longer release time, higher drug load and better-controlled release than their respective PSi substrates. These studies also indicated that CFX is more compatible with both hybrids than PDN in both media. The PBS medium generated a faster release than distilled water due to the higher ionic strength in the buffer.

v) The functional dose of the hybrids to work as drug release systems for CFX and PDN required in ocular medical therapy was estimated from the experimental drug release data for each drug, and the volume of an adult human eye. Additionally, the minimum inhibitory concentration required to inhibit the growth of 90% of microorganisms (MIC90) was considered for CFX and the minimum concentration of necessary PDN to suppress inflammation was taken into account for PDN. Quantities as low as 1 mg of the PSi/cyclodextrin hybrids were considered functional.

5.1.2 PSi/calcium phosphate bioceramic cell scaffolds

i) Two alternative techniques to synthesize PSi/CaP biocomposites were proposed: Cyclic Spin Coating (CSC) and Cyclic Electrochemical Activation (CEA). Since CaPs are ionic compounds, both methods consisted on alternate Ca and P deposition steps on nanostructered PSi. In this way, the individual variables of each step such as pH, current density and reaction time, could be controlled and studied independently.

ii) CSC and CEA produced specific morphologies and CaP phases using the same independent Ca and P stem-solutions at neutral pH and at room temperature. The brushite (BRU) phase was favored with the CSC technique and the hydroxyapatite (HAP) phase was better synthesized using the CEA technique.

iii) The mechanism of CaP electrodeposition on PSi by CEA was studied by a simple system resistance calculation. Results show that CaP deposition on PSi increases linearly with cycles when performed at room temperature, but increases exponentially when temperature reaction is increased.

iv) The synthesis of HAP in CaP/PSi composite by CEA was validated by Ca/P atomic ratio quantification by means of RBS. These results indicated that, by controlling the synthesis parameters of CEA, it is possible to generate CaP on PSi with a Ca/P atomic ratio of 1.67, the ideal value related to HAP.

v) HAXPES was used in order to study the chemical structure of PSi-CaP interfaces obtained by CEA. As previous studies regarding Ca 1s oxidation states have not been reported, two contributions of binding energy for the oxidized species were proposed: HAP at 4042 eV and PYR at 4045.5 eV. According to this, plus the obtained spectra for Si 1s and P 1s, CaP integration into PSi structure is favored when t_{Ca}/t_P ratio is increased. Additionally, as in the case of the bulk region (studied by GA-XRD and RBS), the HAP phase can be promoted in the PSi-CaP interface by means of controlling the t_{Ca}/t_P ratio.

vi) The biocompatibility of PSi/CaP composites obtained by both CaP deposition techniques was tested by hMSCs *in vitro* culture. In the case of the composite synthesized by CSC, cells showed adhesion onto the surface but without evidence of proliferation. Besides, this composite modified the normal morphological appearance of cells, which acquired the shape of the solid flat-plates of BRU clusters. In the case of composite prepared by CEA, cells showed good adhesion, preliminary signs of proliferation and a normal morphology.

As a final and general conclusion, results show the suitability of PSi as a biomaterial for drug delivery and cell scaffold applications.

5.2 Perspectives

Materials, composites and devices based on PSi for biomedical applications are spanning to the commercial dimension. Different companies market PSi for bioapplications: pSiMedica Ltd. (UK), Silicon Kinetics (USA), pSivida (USA), and

others. In that sense, further research on the biocomposites synthesized in this thesis should be performed to promote the transfer to real applied devices.

In the case of PSi/CD hybrids, new drug release profiles in vitreous humour medium could be carried out. As pig eyes are very similar to human eyes, they are an option to be used for *in vivo* kinetic studies for drug release. Vitreous humour consists on a gelatinous mass, which is 98-99% water and salts, sugars and proteins. Thus, drug release in vitreous humour could present profiles between those obtained in distilled water and those in PBS (vitreous humour is more viscous than distilled water and PBS, which would increase the release time but salts inside would facilitate the drug release). In addition, experiments could be carried out with additional antibiotics and anti-inflammatories. Finally, for a complete understanding of the reactions occurring at the oxidized PSi-polyCD interface an accurate investigation of the surface bonds, for example through Raman spectroscopy, would be required.

In the case of PSi/CaP biocomposites, an adsorption of proteins and organic material on CaP could be carried out for the elaboration of the scaffold–cell hybrids for *in vivo* applications. The hMSCs compatibility was already proved, but biochemical factors might help stem cells to differentiate into particular cell types (for bone, cartilage, muscle, ligaments, tendons, adipose and stroma). On the other hand, due to the flexibility of both CaP cyclic deposition techniques (CSC and CEA), an alternative way is opened for ionic compound synthesis on PSi substrates such as carbonates, which would allow forming new biocomposites. In addition, for other fields of application, CSC and CEA could be used to synthesize different layers or mixed compounds on PSi, for example Fe-Au-Fe. This material is used for magneto-resistive random-access memory applications. Finally, in order to strengthen the results of chemical study on PSi-CaP interface of composites obtained by CEA, a more detailed study should be performed to provide a certain attribution of Ca 1s binding energy of different CaP phases.

Abstract

Porous silicon (PSi) is an excellent biomaterial given its biocompatibility, biodegradability and bioresorbability. Nevertheless, it is necessary to adapt its properties depending on the specific application. In that sense, two new PSi-based biomaterials were developed to work in the field of drug delivery and cell scaffolds.

PSi-biopolymer hybrids are attractive as drug delivery devices because they improve control over drug release kinetics and stability. According to this, two kinds of PSi, nano- and macro-, were modified by β-cyclodextrin–citric-acid in-situ polymerization. Both hybrids were characterized by microscopy and physicochemical techniques. Its biocompatibility was proved by means of L132 cells *in vitro* culture. Finally, both hybrids were tested as drug delivery systems with ciprofloxacin-base (antibiotic) and prednisolone (anti-inflammatory), in two mediums, distilled water and PBS. Results showed that both kinds of PSi/cyclodextrin hybrids, are functional for drug delivery applications.

For the use PSi as cell scaffold in bone tissue engineering, deposition of calcium phosphate (CaP) in its hydroxyapatite (HAP) phase provides an added value. Within this context, the synthesis of CaP/PSi composites by means of two different techniques was developed: Cyclic Spin Coating (CSC) and Cyclic Electrochemical Activation (CEA). CSC and CEA consisted on alternate Ca and P deposition steps on PSi. Each technique produced specific morphologies and CaP phases using the same independent Ca and P stem-solutions at neutral pH. The brushite (BRU) phase was favored with CSC and the HAP phase was better synthesized using CEA. Analyses by RBS on CaP/PSi synthesized by CEA supported that, by controlling the CEA parameters, an HAP coating can be promoted. Besides, its PSi-CaP interface was studied by HAXPES. Biocompatibility was evaluated by bone-derived progenitor cells. Depending on the composite used to culture cells, a characteristic response of adhered cells was obtained. These results can be used for the design and optimization of CaP/PSi composites with enhanced biocompatibility for bone-tissue engineering.